Characterization of Mass Transport in the Upper Human Airways

Der Fakultät für Maschinenbau, Verfahrens- und Energietechnik
der Technischen Universität Bergakademie Freiberg

genehmigte

DISSERTATION

zur Erlangung des akademischen Grades eines Doktor-Ingenieurs

(Dr.-Ing.)

vorgelegt

von Diplom-Ingenieur Katrin Bauer

geboren am 01. Juli 1979 in Werdau

Gutachter: Prof. Dr.-Ing. Christoph Brücker, TU Bergakademie Freiberg
Prof. Dr.-Ing. Ulrich Groß, TU Bergakademie Freiberg

Tag der Verleihung: 06. Dezember 2011

Excerpts of this work have been published in international peer reviewed journals:

Adler K., Brücker Ch., 2007. Dynamic flow in a realistic model of the upper human lung airways. *Exp Fluids*, 43 (2-3), pp. 411-423.

Bauer K., Brücker Ch., 2009. The role of ventilation frequency in airway reopening. *J. Biomech.* 42, pp. 1108-1113.

Bauer K., Chaves H., Brücker Ch., 2010. Visualizing Flow Partitioning in a Model of the Upper Human Lung Airways. *J. Biomech. Eng.*, 132, 031005-1-9.

Bauer K., Chaves H., Brücker Ch., 2011. Transport at Air-Liquid Bridges under High-Frequency Ventilation. *Notes on Num. Fluid Mech.*, 116, 2011, DOI: 10.1007/978-3-642-20326-8

Acknowledgment

First of all, I thank my supervisor, Prof. Christoph Brücker, for his advice and guidance throughout my work. I also thank Dr. Humberto Chaves for his great ideas which contributed to the success of this work. The numerical flow simulations presented here were performed by Dr. Alexander Rudert, thank for your work.

Many thanks go to the entire research group of Fluid Mechanics for the great team work and support, especially my room mates, Michael Triep and Armin Keißner, I would like to thank for the fruitful science discussions.

I am very grateful to Sebastian Kunze, Michael Budnitzki and Dr. Johannes Boltze for their instructive comments on my thesis.

I would also like to acknowledge the support of my work by the Deutsche Forschungsgemeinschaft and all members of the research group "Protective Artificial Respiration" for brisk scientific exchange.

Special thanks go to my husband, Daniel Bauer, for his persistent confidence in me and also for various helpful scientific discussions.

Last but not least I would like to thank my parents for all their support I received throughout my life.

Contents

List of Figures

List of Tables

Nomenclature

Latin Symbols

A	Area, Amplitude
A_0	Amplitude of instability
A_{max}	Maximum displacement
C	Compliance
Ca	Capillary number
d,d_0	Wall thickness
D	Diameter
Dn	Dean number
d_p	Particle Diameter
Eu	Euler number
f	Frequency
F	Force
f_w	Drag coefficient
g	Constant of gravitational acceleration
G	Shear modulus
h	Liquid depth
H	Height, Helicity
$I(x, y)$	Intensity of Light
J_m	Bessel-function of m-th order
k	Wave number
l	length
$m(x, y)$	Modulation of light
$M(x, y)$	Modulation function
n	Refractive index
p	Pressure
r	Radial variable
R, r_0	Radius
R	Resistance
Re	Reynolds number
St	Stokes number

t	Time
T	Cycle time
TV	Tidal Volume
V	Volume
$\dot{V}$	Volume flow
u	Velocity variable
U	Flow velocity
We	Weber number
x, y, z	Axial coordinates

Abbreviations

ALI	Acute Lung Injury
ARDS	Acute Respiratory Distress Syndrome
CMV	Conventional Mechanical Ventilation
CT	Computed Tomography
DNS	Direct Numerical Simulation
FVM	Finite Volume Method
GAMG	Geometric Agglomerated algebraic MultiGrid solver
HFV	High Frequency Ventilation
HFJV	High Frequency Jet Ventilation
HFOV	High Frequency Oscillatory Ventilation
LED	Light Emitting Diode
LES	Large Eddy Simulation
LIP	Lower Inflection Point
PEEP	Positive End-Expiratory Pressure
PFC	Perfluorocarbon
PISO	Pressure Implicit with Splitting of Operators
PIV	Particle Image Velocimetry
PLV	Partial Liquid Ventilation
VILI	Ventilator Induced Lung Injury
UIP	Upper Inflection Point

Greek Symbols

α	Womersley number
β	Material constant
δ	Damping constant
η	Dynamic viscosity
λ	Wavelength
ν	Kinematic viscosity
ρ	Density
σ	Surface tension
τ	Time constant
$\phi(x,y)$	Probability function
ω	Angular frequency, vorticity
$\hat{\omega}$	Natural frequency

1 Introduction

Mechanical Ventilation is required in the case of respiratory failure as patients loose their ability to breathe spontaneously. In the early stages of mechanical ventilation, patients were placed in a steel chamber, called iron lung, where a negative pressure was applied to the lung in order to mimic spontaneous breathing. In this form the iron lung provides non-invasive ventilation. Due to several disadvantages and side effects such as restricted motion of patients and hindered accessibility by medical personal, the iron lung was almost totally replaced by positive pressure ventilation. Since its introduction in the 1950s in the course of the poliomyelitis-epidemic, positive pressure ventilation has been proven to provide a live-saving therapy in intensive care medicine [111]. Mortality rates were reduced dramatically.

Nevertheless, mechanical ventilation, when applied over longer period of time may also be a potential risk for life. Positive pressure induces large shear stresses in the lung tissue which can lead to Ventilator Induced Lung Injury (VILI) such as Volu-[1] and Barotrauma[2] [61, 109]. Reasons for these lung injuries are strongly alternating pressure levels and the lung structure itself which is highly inhomogeneous and anisotropic. Consequently, also lung injury is not uniform as indicated by X-ray Computed Tomography (CT) images [37, 73, 95]. These references have shown that some regions are severely affected by acute inflammation and atelectasis[3] whereas others appear to be completely spared. Affected areas are characterized by a lower compliance especially, with atelectasis. Time constants of different regions, i.e. filling and emptying times, vary largely. Pulmonary characteristics differ regionally, leading to a further inhomogeneous distribution of air during mechanical ventilation [19, 114]. Consequently, ventilation leads to overdistension of the healthy parts whereas atelectatic regions might remain collapsed. Additionally, frequent recruitment (opening) and derecruitment (collapse) of lung parts further damages lung tissue.

Neonates, i.e. premature infants whose lung might not be fully developed, have higher risks for potential lung damages. The reasons are that the cartilaginous rings, which are stiff in adult lungs, are soft in the early days of life. Surfactant, a substance which decreases surface tension, can be missing. This leads to decreased lung compliance and high risk of atelectasis. The lungs of newborns are per se characterized by very low compliance, whereas the resistance due to pressure loss is higher than in adult lungs [29]. Therefore, children also have a higher risk of barotrauma during mechanical ventilation.

The aim of this work is to contribute to a more protective ventilation by fundamental

---

[1] Lung damage by overdistension during mechanical ventilation

[2] Lung damage by too high pressure during mechanical ventilation

[3] collapse of alveoli

physical understanding of the lung ventilation funded by the “Deutsche Forschungsgemeinschaft” DFG with the project BR 1494/7-1. Therefore, the understanding of mass transport in the human lung under normal breathing conditions as well as in diseased lungs needs to be improved, which is the purpose of this work. This project is part of the interdisciplinary research group “Protective Artificial Respiration” where medical scientists and engineers work closely together. Our medical research partners are Prof. Georg Simbruner (Division of Neonatology, Clinical Department of Pediatrics, Innsbruck Medical University, Austria) and Prof. Mario Rüdiger (Department for Neonatology and Pediatric Intensive Care Medicine, Carl Gustav Carus University Hospital, Dresden, Germany).

For the engineering part, which is subject of this work, a lung model was generated, at which the flow could be investigated experimentally by means of Particle Image Velocimetry (PIV)-measurements and numerically by Computational Fluid Dynamics (CFD). Different breathing and ventilation conditions, respectively, were simulated. For these cases, the model is characterized by a rigid airway structure. In an extended model, the case of an collapsed lung was simulated and recruitment (reopening) behavior was investigated. A flexible boundary was integrated, which mimics the nonlinear pressure-volume behavior of the human lung. The last study deals with liquid airway blockages, as they might occur by increased mucus production or collapsed airways. Steady streaming at a liquid-air interface and break up of liqid bridges was investigated by means of optical flow visualizations. Therefore, a simplified model, consisting of a liquid filled tube, was utilized.

2 State of the art

2.1 Lung anatomy

The human lung consists of two main lobes (left and right). Each of which is further subdivided; the right main lobe into upper, middle and lower lobes (see Fig. 2.1). The left lung consists of only two lobes (upper and lower) and is also smaller than the right lobe since the heart is located slightly on the left side of the thorax.

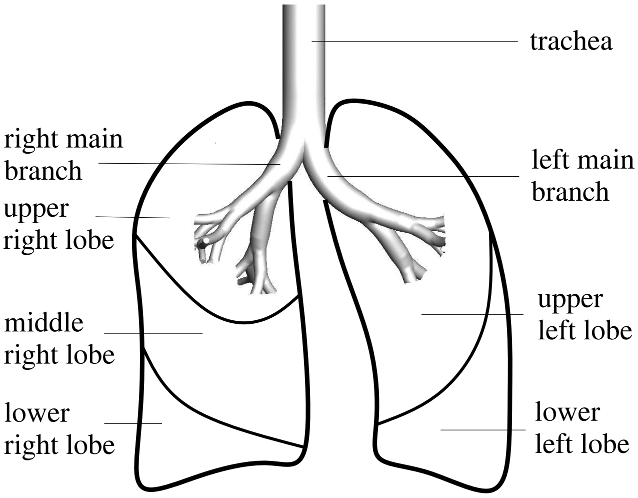

Figure 2.1: Schematic of the human lung lobes.

During spontaneous breathing, the diaphragm, a thin muscle which separates the thoracic from the abdominal cavity, contracts, which causes a negative pressure (relative to the ambient pressure) within the lung and thus, the inhalation. During relaxation of the diaphragm the expiration takes places. That means, the pressure in the lung rises up to the ambient pressure outside of the body.

Within the respiratory system (Fig.2.2) the air passes the mouth or nose first followed by the pharynx and larynx (the connection between pharynx and trachea, not shown in Fig. 2.2), the trachea, the bronchial tree and finally, at the end of the bronchial tree, the alveoli, at which the gas exchange takes place. The typical diameter of the alveoli is about $250\,\mu$m [115] and they are coated by a thin film (about $1\,\mu$m [115]) called surfactant - surface active agent - which reduces the surface tension and increases lung compliance. Thereby, surfactant prevents the alveoli from collapse and reduces the potential to damage the airways.

Within the bronchial tree, the air passes 23 dichotomic generations until it reaches the distal ends, i.e. the alveoli. The top of the bronchial tree is the trachea. It is a flexible

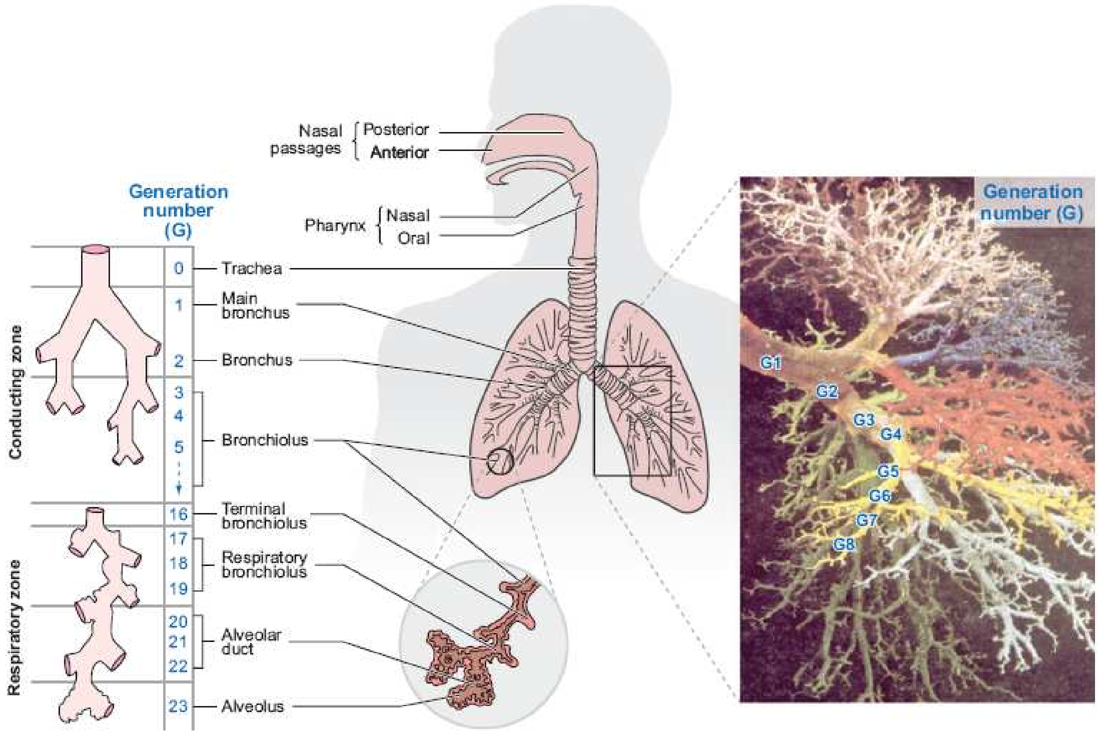

Figure 2.2: Schematic drawing of the respiratory system, according to Kleinstreuer et al. [58].

tube which can extend up to 60 % in cross sectional area when inflated to 6 kPa [70]. The average trachea length is between 10 − 13 cm [8] and it consists of 16-20 C-shaped cartilage rings [4] which are open to the dorsal (back) side of the lung. The rings prevent the trachea from collapse during breathing. The tips of the C-shaped rings are connected by an elastic muscular membrane [102]. In neonates, the cartilage rings are still very soft. In diseased lungs, where the lower regions have a low compliance, a large amount of air is trapped in the trachea as mechanical ventilation is applied. The behavior of the trachea can be compared to the Windkessel effect, well known for the aorta in the arterial circulation system. Hence, the alveoli are only insufficiently supplied with fresh air. This effect has been observed by our medical partner. The inside of the trachea is coated by mucus and epithelial cells which are responsible for mucus transport [4].

The trachea bifurcates into the left and right main bronchus (see Fig. 2.1 and 2.2) which further bifurcate down to the 23rd generation. The first 16 generations form the conducting zone (Fig. 2.2), which is dominated by inertia and convective mass transport. The lower generations 17-19 form a transition zone, followed by the respiratory zone (generation 20-23), where the gas exchange takes place [116]. In the lower branches, especially from the 17th generation on, mass flow is dominated by diffusive transport mechanisms due to very low velocities. The reason for the change in mass transport is the exponential increase of the total cross section area from the 17th generation on. At the 23rd generation the alveoli form a total cross section of more than $10000\,\mathrm{cm}^2$ [116]. In contrast, at the trachea the cross section is only $2.5\,\mathrm{cm}^2$ and even slightly decreases till the 3rd generation. The average dead space of the human bronchial tree is about 150 ml [4, 116].

The data from Weibel [116] are based on statistical analysis of a human lung cast and represent average values for each generation. Weibel presented a symmetric bronchial tree model with diameters and lengths for each generation and straight branches. These data were very frequently used for model generation by other researchers since they are simplified but still based on a real lung. However, a real bronchial tree is asymmetric and three-dimensional. CT-scans from human lungs demonstrate the different diameters and lengths of branches within one generation and strong curvature of the branches. Horsfield [47] presented data of one typical male lung incorporating different diameters, lengths and curvature of each branch. These data from Horsfield were also frequently found in literature since a realistic lung can be reconstructed.

Some studies have demonstrated the fractal nature of the bronchial tree (e.g. [80]). A fractal can be space filling and ensure minimal dissipation. Interestingly, a study by Mauroy et al. [75] has shown that an idealized bronchial tree concerning dissipation, is more sensitive to malfunction such as asthma. Here, slight changes in the airway geometry can cause a steep increase of airway resistance. Hence, the bronchial tree must have a safety factor for possible constrictions in the airway diameter.

2.2 Airway mechanics

The human airways are very flexible and expand during inspiration. The relation between pressure and volume in the human lung is non-linear as depicted in Fig.2.3 a). The pressure-volume (p-v)-curve during a whole breathing cycle for a healthy lung is shown (extracted from [92]). It can be seen, that the curves for inspiration and expiration are not identical but form a hysteresis loop. The slope represents the total compliance of the lung and thorax. The compliance is therefore defined by $C = \triangle V/\triangle p$. Here, $\triangle V$ denotes the increase of volume during the pressure increase $\triangle p$. The inverse of the compliance is the elastance. The work of breathing is represented by the enclosed area. The compliance together with the resistance and inertia contribute to a total impedance of the respiratory system. Whereat the resistance occurs due to viscous pressure loss and the inertia due to the inertia of the lung tissue and the acceleration of mass within the lung. Since the inertia of the lung tissue and the air are very small, it is often neglected [5]. The product from resistance R and compliance C represents the time constant $\tau = R{\cdot}C$ of a respiratory unit. Hence, locally different compliances lead to different time constants in the lung.

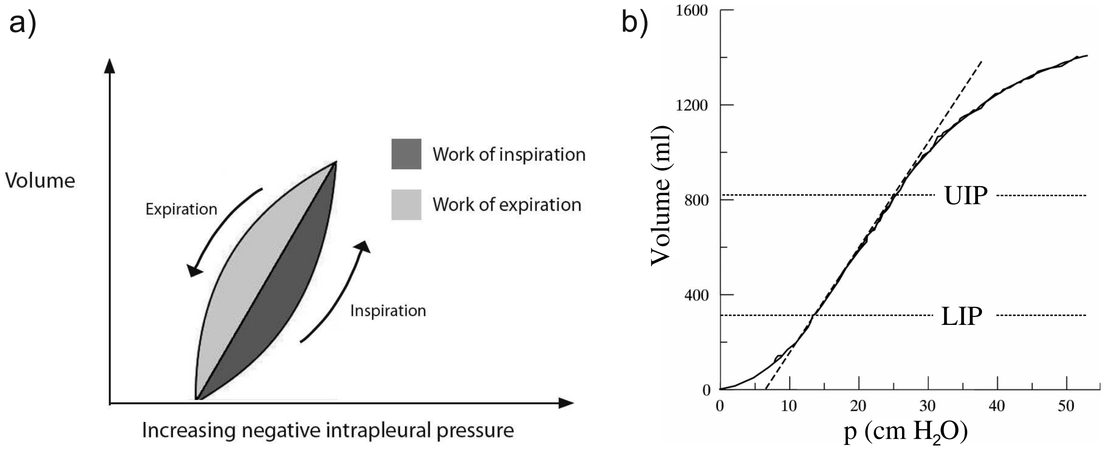

Figure 2.3: a) Pressure-volume relation during whole breathing cycle of the healthy lung, from Roberts [92] , b) pressure-volume relation during inflation of a lung affected with ARDS, modified from [53].

Fig. 2.3 b) shows the pressure-volume relation for the case of a lung disease called ARDS - Acute Respiratory Distress Syndrome, extracted from Jonson and Svantesson [53]. ARDS is a subcategory of an Acute Lung Injury (ALI) which can be associated with collapse of the alveoli, stiff lung tissue, pulmonary infiltrates [95], i.e. liquid occurs in the lung, inflammation and as consequence, a decreased partial pressure of oxygen in the blood [119]. The death rate is at about 38 % [95].

The low increase in volume at the beginning of the curve in Fig. 2.3 marks the ventilation of already open alveoli. Further increase of the pressure leads to recruitment of collapsed lung areas and to a higher slope of the curve. The change from low to high increase rate of volume is called "lower inflection point" (LIP). The compliance is increased. As all areas are recruited, a further increase of pressure causes overdistension of the alveoli and a decrease of compliance. This point is called "upper inflection point" (UIP) [46, 53].

Suki et al. [100] observed the inflation of a collapsed lung as a kind of avalanche phenomenon. As the intra-bronchial pressure exceeds a certain threshold level, the so called "opening pressure", one of the collapsed airway branches opens first and an avalanche is initiated which inflates all more distal airways whose opening pressure is below the threshold. Due to the corresponding volume increase the pressure in the recruited airways subsequently decreases. A further increase of the intra-bronchial pressure would release new avalanches. These ideas of Suki et al. were further developed in Alencar et al. [2]. They characterize the airway reopening during inflation of the lung as a form of an avalanche shock. These shocks are represented in the p-V diagram as phases with falling pressure during increasing volume which they attributed to a “negative elastance”.

2.3 Ventilation techniques

Conventional Mechanical Ventilation - CMV

During mechanical ventilation the patient is supplied with air at normal breathing conditions. The tidal volume, i.e. the volume that is breathed in and out, is about 500 ml or 10 ml/$\text{kg}_{\text{bodyweight}}$ [4] for neonates whose lungs are much smaller. The breathing frequency is about 15 breaths per minute, i.e 0.25 Hz for adults. The natural breathing frequency for neonates is higher at about 60 breaths per minute (1 Hz). Patients are either ventilated non-invasively by a face mask or invasively by an endotracheal tube. The tube is inserted into the lung via the nose or mouth, whereat the exit of the tube is placed in the trachea center ahead of the bifurcation. The typical outer tube diameter for an adult lung ventilation is about 13 mm and thus smaller than the trachea diameter which is typically between $18-20$ mm. To prevent the patient from aspiration[1] a cuff (small balloon), circumferentially attached to the outside of the tube, is inflated, which closes the gap between tube and trachea. In neonates the outer diameter of the tube is as large as the inner trachea diameter, hence a cuff is not necessary.

Mechanical ventilation is either pressure- or volume-controlled. During pressure controlled ventilation a pressure is set and the tidal volume varies depending on the compliance and resistance of the complete respiratory system which includes the ventilator machine with all tubes and the human lung [86]. At volume controlled ventilation the tidal volume and flow rate is set and the pressure adjusts again according to the compliance and resistance of the respiratory system [86]. Both methods are equally used.

Positive End-Expiratory Pressure - PEEP

---

[1] inhalation of any liquid or solid substance

In order to avoid airway collapse, a positive pressure level (PEEP) after the end of expiration was applied during ventilation. The PEEP - values vary between 5 and 15 $\mathrm{cmH_20}$ [37]. The use of the correct PEEP level is crucial. Overly levels can further increase already open lung areas and induce barotrauma, while too low levels can lead to derecruitment [37], [61]. Unfortunately, there is no consense on how to choose the optimal PEEP-level. It strongly depends on the recruitable lung area. Furthermore, the patient's mortality rate is even more influenced by the tidal volume. Low tidal volumes can decrease the mortality rate from 40% down to 31% after mechanical ventilation [9].

Noisy Ventilation

Another approach to successfully recruit atelectatic (collapsed) lung areas is biologically variable ventilation. Here, ventilation frequency and tidal volume is randomly varied from breath to breath during mechanical ventilation [78]. Suki et al. [98] have added some noise to the input signal. They reported about a kind of stochastic resonance whereat the Pa_{O_2} (partial pressure of oxygen) in the blood could be improved. In a further study [99] they have shown that noisy ventilation also leads to less Ventilator Induced Lung Injury (VILI) and even increases surfactant content.

High Frequency Ventilation - HFV

In the 1960s an alternative ventilation method with lower tidal volumes, below the anatomic dead space, but higher ventilation frequencies was first developed, called high frequency ventilation (HFV). Here, the tidal volume is between $2-5$ ml/kg bodyweight [60] and the applied ventilation frequency is between 8 and 15Hz for neonates and 3-7Hz for adults [17].

HFV seemed to be promising concerning lower rates of lung diseases [60]. Shear rates and stress of the lung tissue are reduced. However, recent studies are controversial about the advantages over conventional mechanical ventilation (CMV). According to Johnson et al. [52] and Reempts et al. [108], the rate of lung diseases and mortality of premature infants was similar for HFV and CMV. Stark [97] and Courtney et al. [16] reported some protection of HFV as it was applied very early and by experienced clinicians. However, the pulmonary outcome is more dependent on other neonatal risk factors such as e.g. initial resuscitation [97,108]. The long term effect of the ventilation mode is still not fully known and more studies are demanded. Nevertheless, HFV is routinely used in neonatal intensive care units, and there is a growing interest for its application in adults with ALI and ARDS [14,91].

HVF is subdivided into two categories:

- **High Frequency Oscillatory Ventilation - HFOV**, whereat an oscillation of the air is generated by a membrane, e.g. a loudspeaker membrane or a piston [49]
- **High Frequency Jet Ventilation - HFJV**, a jet of air is pushed into the lung at high frequency between $2.5 - 10\,\mathrm{Hz}$ [49].

Partial liquid ventilation - PLV

An alternative approach of ventilation was developed by Fuhrmann [36] in 1991, whereat patients with ALI or ARDS are ventilated by perfluorocarbon (PFC) instead of air. PFC is inert and chemically stable with a density of $1800\,\mathrm{kg/m^3}$ [88] and can dissolve very high amounts of gas (oxygen). Due to its high density compared to air it flows rapidly into lower airways where it helps to recruit atelectatic regions and thereby improves gas exchange and reduces inflammation. Furthermore, it prevents lung regions from end-expiratory collapse according to PEEP [88]. Despite these facts, studies have shown no significant difference in mortality rate compared to CMV [88]. Its clinical relevance is still low since past clinical studies are not sufficient concerning dosing, indication and duration of treatment or ventilation pattern.

2.4 Human bronchial tree models

Many studies have demonstrated the strong influence of the lung geometry on mass transport e.g. [74,85]. Therefore, a realistic generation of the lung model is crucial. Even though the upper airways have a symmetric geometry the use of a symmetric model causes asymmetric flow and transport behavior. For example, Zhang and Kleinstreuer [123] simulated the airflow in a planar, symmetric airway model. This symmetric model leads to asymmetric velocity distribution as depicted in Fig. 2.4 a). The inner branches of each generation are characterized by higher flow velocity. In contrast, Liu et al. [69] used an asymmetric geometry with larger diameters of the outer branches. The velocity profiles in this model are shown in Fig. 2.4 b) for a low Reynolds number of $Re = 200$. It can be seen that the maximum velocity in inner and outer branches is similar or even higher in the outer branches. They analyzed the flow partition relation between daughter branches G7 and G9' as function of the Reynolds number. For low Re, the outer branch with the larger diameter received almost threefold the mass of the inner branch. With increasing Reynolds

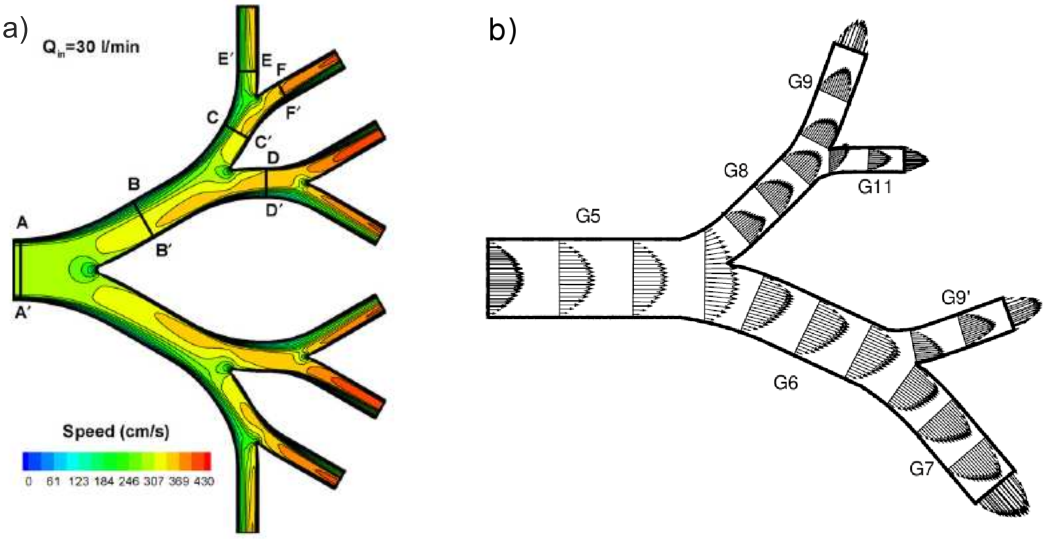

Figure 2.4: Comparison of different lung models, a) veloctiy contours during steady inspiration in a symmetric airway model from Zhang and Kleinstreuer [123], b) axial velocity vectors in an asymmetric lung model from Liu et al [69]

number up to $Re = 1600$, the relation between inner and outer branch becomes more homogeneous whereat the outer branch received less than twice the mass flow rate of the inner branch. For comparison, the Reynolds number during normal breathing is about $Re = 2000$. These studies have demonstrated the influence of the model on flow partitioning and flow patterns. If high Reynolds numbers were applied on symmetric airway models, flow partitioning becomes rather asymmetric. However, the asymmetric model suggested by Liu et al. [69] overestimates the differences of branch diameters within one generation, with diameters varying by 50-100%. According to Horsfield [47], the diameter varies only by 10-60% within one generation.

The models shown in Fig. 2.4 are both simplified. First, they are planar, whereas a real bronchial tree is three-dimensional. Second, they incorporate only three generations. This is very common in literature, since some flow characteristics occurring in a real lung can already be shown in those simplified models. Some researchers even prefer the use of two generations, only (e.g. [28, 45, 66, 94, 101]).

As mentioned before, a real lung consists of 23 generations which all contribute to a flow resistance. This is neglected by low generation models. Hence, the higher the generation number, the more realistic becomes the flow in the lung. However, up to date, a maximum number of 6 generations has been incorporated by most researchers to create lung models (e.g. [11, 68, 84]). For both cases, experimental and numerical research, 6 generations seem to mark a barrier. Since the branching diameter decreases with every generation, the technical effort is too high to manufacture a model with more than 6 generations for experimental research. With each new generation the branch number rises quadratically. An adequate grid resolution at a model with more than 6 generation would exceed the possible numerical effort.

The strong increase of computer power in the recent years has allowed few researchers to extent the human airway tree for numerical simulations. Wall et al. [112] used a lung model with 7 generations. However, it was discretized by 2 million cells only. Calay et al. [12] revealed that a number of $100,000 - 150,000$ cells per bifurcation is necessary for a mesh independent solution. A 7-generation model has $2^n - 1 = 2^7 - 1 = 127$ bifurcations. Hence, a mesh independent solution should be based on at least 12.7 million cells. Gemci et al. [40] used a 17 generation model with 1453 bronchi, i.e. single branches with $6,744,000$ cells. This number is first too small for sufficient flow resolution, and second, not characterized by bifurcations down to the $17th$ generation since constant bifurcating from the $1st$ to the $17th$ generation would yield $2^{n+1} - 1 = 2^{18} - 1 = 262,143$ single branches.

Very frequently, CT-data are used for model generation with a large number of generations [11, 68, 84, 112]. The advantage is that these geometries are very close to the reality. However, a disadvantage of CT-data is that they largely depend on the reconstruction procedure and on the threshold of the grey level for the images. Hence, the same lung scanned by two different devices can yield different results. Reproducing the CT-model by Rapid Prototyping induces additional deviations in an uncontrollable manner from the original model due to additional surface finishing procedures. To conclude, creating a CT-based model is hardly reproducible.

Low generation models are mainly based on statistical data (e.g. [82, 122, 123]) derived from Weibel [116] for a symmetric bronchial tree or from Horsfield [47] for an asymmetric model (e.g. [12, 65]).

Kitaoka et al. [57] presented a lung model based on statistical geometry data which even includes 23 generations. However, they only concentrated on the model generation and never performed flow investigations.

Some researchers (e.g. [59, 68, 123]) extended their bronchial tree model by the laryngeal geometry (oral airways from the mouth to the trachea). It is known that the integration of this upper airway geometry into the lung model leads to an altered inflow situation. The parabolic shape of the velocity profile is changed to a curved sheet-like shape and turbulent structures are enhanced [68,71]. Xi et al. [120] have shown in their studies that in the laryngeal tracheo-bronchial model, particle deposition is enhanced in the larynx and in the upper trachea regions compared to models without larynx.

For the analysis presented in this work, the laryngeal geometry is not included since the flow structure in the lung under ventilated conditions is in the main focus of interest. The mechanical ventilation which is investigated here, is usually carried out with an endotracheal tube. The use of such a tube again totally alters the inflow situation [1]. It is also highly stochastic and variable due to different techniques of intubation and the position of the tube exit in the carina. Therefore, it was abstained from the adjusted inflow situation caused by an endotracheal tube or the laryngeal jet since both lead to different effects of mass transport and velocity profiles. Here, the differences in flow partitioning caused by the geometry and pressure loss in the branching network were in the main focus of interest. The influence of the tube or laryngeal geometry would disturb the effects observed here. Additionally, Zhang and Kleinstreuer [123] have shown that the entrance effects due to the laryngeal geometry begin to weaken downstream from the 3rd generation on.

The aforementioned models do all neglect the influence of the non-linear pressure volume behavior of human lung tissue, i.e. they do not incorporate lung compliance. The distal endings of these models are open to the ambience without any further resistance. Most frequently, the same boundary condition is applied at each end. In numerical studies, different types of boundary conditions are used. First, the pressure outlet, whereat each outlet receives the same pressure value, (e.g. [40, 50, 72, 123]) is implemented. For the case of the human lung flow simulation, zero pressure is chosen. Lin et al. [68] assumed uniform ventilation and therefore specified uniform velocity. Another boundary condition is to specify a constant outflow rate at each outlet [82, 107] as fraction of the inlet flow. Van Ertbruggen et al. [107] specified different outflow rates for each outlet according to values given by Horsfield [48]. Despite different flow rates for the outlets, they did not incorporate different compliances.

However, as mentioned above, the influence of the compliance is especially important in diseased lungs and strongly varies regionally. Due to the complex behavior of a non-linear pressure volume system, only single bifurcation models with compliant endings exist so far.

A variation in boundary conditions was applied by Yang et al. [121] who investigated the influence of airway obstruction on the flow. Elad et al. [26] simulate the flow partitioning in a single bifurcation with various compliant endings. Lee et al. [64] investigated the flow behavior during HFOV by means of Particle Image Velocimetry (PIV) - measurements in a rigid single bifurcation model with compliant endings.

2.5 Flow characteristics in the human lung

Velocity profiles

The branch curvature and bifurcations themselves, occurring in the human lung, lead to skewed velocity profiles. The centrifugal forces push the fluid to the outside wall of the curvature. Hence, velocity profiles are asymmetric with the velocity maximum near the outer wall of a curvature. Thereby, asymmetric flow partitioning is created [3, 10].

Separation regions occur whose number, size and location depend on the Reynolds number [83]. As shown by Bruecker and Riethmuller [10] the flow in bifurcating networks can undergo low-frequency oscillations. This is due to a type of resonance effects caused by the multiple interaction of flow separation and shear layer-edge interaction.

It was further shown that the velocity profiles in the upper airways differ between inspiration and expiration [94].

These asymmetric velocity profiles occur in the center plane of the lung heading from the left to the right side. In the transverse plane, from the front to the rear side of a curved branch, the velocity profiles are symmetric and M-shaped. Compare Fig. 2.5a) for front/rear and left/right positions in the lung branches. Usually, one expects M-shaped velocity profiles in oscillatory tube flow due to the phase shift of low inertia near wall flow and high inertia center flow [105]. However, this M-shaped velocity profile also occurs for steady flow in curved tubes (e.g. [12, 69] in the front-rear-plane due to the streamline curvature [69]. These M-shaped velocity profiles are related to secondary flows and hence, skewed velocity profiles. At low flow velocity, the velocity profile in the transverse plane remains parabolic due to weaker secondary flow [69].

Secondary flow

The tube curvature causes secondary flows due to centrifugal instabilities. The emerging vortices are known as Dean vortices [18]. Thereby, fluid at the centerline of the bend is forced to the outer wall where it splits symmetrically, moves circumferentially to the inner curvature wall where it merges and proceeds again to the outer wall. Two counter-rotating vortices are generated during inspiration (Fig. 2.5b)). Whereat, during expiration a quadruple vortex occurs (Fig. 2.5c)).

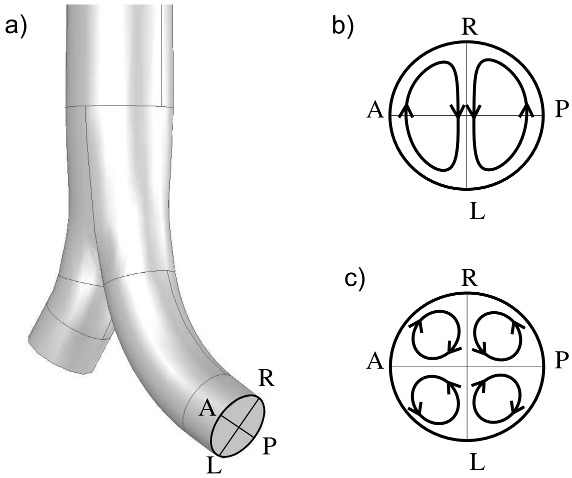

Figure 2.5: Secondary vortex structure, a) Nomenclature of the branches, with R - right side of the branch, L - left side of the branch, A - anterior (front) side, P - posterior (rear) side, b) secondary flow structure during inspiration, c) secondary flow structure during expiration.

Augmented Dispersion

Augmented dispersion denotes the combination of lateral mixing by secondary motions and axial convection [21,34]. Redistribution of mass by secondary flows in the respiratory system is termed augmented dispersion [33]. This type of cycle-to-cycle streaming is similar to the process of molecular diffusion, however the transfer rates are orders of magnitudes higher [21].

Trap and release effect

The oscillatory nature of the lung flow also induces effects which do not occur during steady flow. Mochizuki [77] observed a trap and release effect in the upper airways due to the cyclic built-up and wash-out of flow separation regions leading to a net mass transport into the lung.

Steady Streaming

The effect of steady streaming is known in various applications such as oscillatory flows in tapered channels [38], curved or flexible tubes [25], [20,113].

Steady streaming was first described for the human lung by Haselton and Scherer [43] within a single bifurcation tube model. According to them the Y-shaped bifurcating geometry of the airways leads to steady streaming. Due to this geometry, the upstream and downstream directed flow through the airways is not symmetrical and characterized by different velocity profiles. Hence, after one oscillation period particles do not return to their initial position but are shifted. As a result of the oscillating flow and the different velocity profiles in the bifurcations fluid particles travel either down to the distal end or up to the trachea, depending on their initial location in the cross section of the tube (near to the center or near to the wall). Thus a bidirectional mass transport is induced by the bifurcating lung geometry. Theunissen and Riethmuller [103] observed the net transport of particles after one breathing cycle. They confirmed that particles near to the wall move downwards, whereas particles near the center move up.

The occurrence of the mean motion called steady streaming is forced by Reynolds stress gradients similar to turbulence [67]. By time averaging the fluctuation terms in the Navier Stokes equations the resulting body force terms are the gradients of Reynolds stresses. Since the body force terms are proportional to the Reynolds number, it can be assumed that the streaming increases with increasing Reynolds number [41]. This dependency on the Reynolds number was also observed by Haselton and Scherer [43].

Steady streaming was not only described for the upper airways, it does also occur in the alveoli if surfactant is artificially added to surfactant depleted alveoli. Steady streaming helps to further distribute the surfactant. Another, very typical flow in the alveoli is a net flow from regions of low to high surface tension leading to the distribution of surfactant. This is called Marangoni flow [115].

Pendelluft

An important influence on mass transport is due to the differences of time constants in the lung which lead to asynchronous filling and emptying. This can in turn lead to a mass flow from the emptying to the filling branches known as pendelluft. The pendelluft effect is mainly observed during HFOV [13,64,106] due to the short inspiration times compared to different time constants of different lung regions.

Turbulence

Some numerical flow studies in the human lung consider turbulent flow in the upper airways. However, Lin et al. [68] reported that turbulence becomes only important if the laryngeal geometry is included. Van Ertbruggen [107] et al. performed numerical flow simulations in a model of the human bronchial tree without laryngeal geometry by incorporating both, a turbulence model ($k - \epsilon$ - model) and laminar flow. They found no significant difference between both simulations.

Researchers who performed turbulent flow simulations in the human lung used different approaches. Luo et al. [72] and Gemci et al. [40] employed Large Eddy Simulation (LES) models, Zhang and Kleinstreuer [123] and Van Ertbruggen [107] used low Reynolds $k - \epsilon$ - models. Lin et al. [68] even used a Direct Numerical Simulation (DNS) in order to resolve turbulent eddies at all scales.

As could be seen, there are a lot of different studies concerning the investigation of human lung flow. Many flow phenomena could be described. Nevertheless, the mass transport mechanisms in the human lung are still not fully understood, especially during HFOV. Questions like how to recruit collapsed airway regions without further damage of healthy lung regions, or, why is HFOV as efficient as CMV, are still unanswered. Past studies have mainly focussed on selected regions or flow phenomena. Therefore, further studies concerning the flow in the upper airways have been carried out, here.

2.6 Characteristic flow parameters

The flow in the upper airways of the human lung can be defined by three non-dimensional characteristic numbers, the Womersley number α, the Reynolds number Re and the Dean number Dn. The Womersley number represents a non-dimensional frequency in oscillatory tube flow defined by the breathing frequency f, the kinematic viscosity ν of the fluid and the diameter D of the trachea (equation 2.1).

$$\alpha_{trachea} = \frac{D}{2}\sqrt{\frac{2 \cdot \pi \cdot f}{\nu}}. \tag{2.1}$$

It describes the unsteady nature of fluid flow in response to an unsteady pressure gradient and is a ratio of inertia to viscous forces in oscillatory flows [118]. For very small Womersley numbers ($\alpha < 3$), quasi-stationary flow can be assumed with velocity profiles similar to a laminar parabolic profile with the flow maximum in the pipe center [105]. For increasing α the axial velocity profiles are no longer parabolic and the bulk flow is phase-shifted in time relative to the oscillating pressure gradient [105]. Consequently, the velocity maximum is shifted to the tube wall and the velocity profiles are characterized by an annular shape. In order to keep the Womersley numbers constant for the same geometric scale in model and original, the ratio of frequency to viscosity has to be kept constant.

The Reynolds number of the flow in the trachea indicates the laminar or turbulent character of the flow. It is defined as the ratio of inertia to viscous forces (equation 2.2).

$$Re_{trachea} = \frac{\rho U^2 A}{\eta \frac{U}{D} A} = \frac{U \cdot D}{\nu}. \tag{2.2}$$

In equation 2.2 ρ denotes the fluid density, η the dynamic viscosity, A is the cross section area, D the diameter of the trachea and U denotes the characteristic velocity which is the maximum of the mean axial velocity over the cross section of the trachea in this case. The maximum velocity depends on the tidal volume V and the oscillatory frequency f according to equation 2.3.

$$U = \frac{V}{2} \cdot \frac{2 \cdot \pi \cdot f}{A_{trachea}} = \frac{4 \cdot V \cdot f}{D^2}. \tag{2.3}$$

Hence, the Reynolds number can be written as

$$Re_{trachea} = \frac{4 \cdot V \cdot f}{D \cdot \nu}. \tag{2.4}$$

The last characteristic number, the Dean number is a measure for the ratio between centrifugal and viscous forces in a curved tube. It is defined as

$$Dn = Re\sqrt{\frac{D/2}{R}}. \tag{2.5}$$

The variable R denotes the curvature radius. Fresconi and Prasad [31] found for their experimental lung model that at a Dean number around $Dn = 10$ secondary vortices, as described above, start to form. The strength of the vortices increases with Dn and linearly with Re up to $Re = 100$. For higher Re, the strength increases only slightly. One reason is that despite higher Re, the secondary flow does not have the sufficient length within the lung branches to fully develop. Subsequent bifurcations interrupt the development. Additionally, for increasing generation number, Re and Dn decrease. Hence, as assumed by Fresconi and Prasad [32] secondary flows do not develop below the 10th generation of the lung for CMV and below the 13th generation for HFOV conditions.

3 Dynamic flow patterns in the upper airways

3.1 Objective

In the subsequent study the flow in the upper airways will be investigated by means of Particle Image Velocimetry (PIV)-measurements in a rigid bronchial tree model which consists of 6 bifurcating generations. The lung model represents a case, at which the outlets at the 6th generation have nearly constant pressure without additional resistance or compliance. As described above, the real lung structure from the 6th generation down to the alveoli has an additional impedance which may vary from branch to branch. The model, used here, is based on an idealized geometry and the behavior of a real lung may be different. However, it offers the advantage to compare experimental and numerical results for exactly the same geometry.

The aim of the study is a more comprehensive physical understanding of the effects during CMV and the influence of high frequency oscillatory ventilation (HFOV) on the flow patterns and mass flow distribution. To what extend the flow characteristics described above are changed at the transition from normal breathing to HFOV is not yet clear. Previous studies on HFOV focused on the 15th-18th generation in which inertia is not dominant [64, 90].

3.2 Experimental methods

3.2.1 Transparent lung model

The geometry of the airway model is based on two different data sets. The radius of the curvature with its origin at the daughter branch (see. Tab. 3.1) as well as the transition zones between the parent and the daughter branches are based on Horsfield [48] data. For the diameters and lengths of the generations, data from Weibel [116] were taken which apply for an ideal bifurcation of the lung. In order to create an asymmetric geometry the branch lengths l_r and l_l in each bifurcation relate to each other according to the golden ratio with $l_r/l_l \approx 1.62$. The mean value of the branch length $l = (l_r + l_l)/2$ in each bifurcation corresponds to the value given by Weibel. Each daughter bifurcation is connected to the parent branch by rotating the plane of the daughter branches by 90° with respect to the previous orientation. The only exception is the first generation which is connected to the trachea by a rotation angle of 60°. All geometrical data which were used for the design of the lung model are summarized in Tab. 3.1.

	Gen.	D	l_l	l_r	R_l	R_r
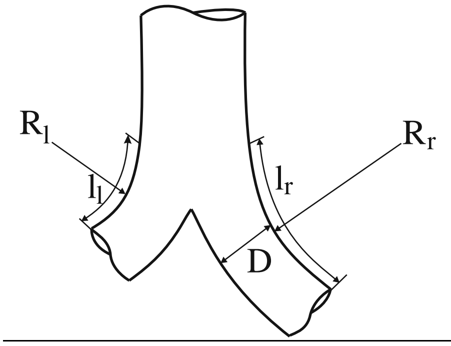	0	18.0	150			
	1	12.2	36.8	59.3	36.6	55.0
	2	8.3	14.7	23.6	52.2	29.0
	3	5.6	5.8	9.4	33.2	45.0
	4	4.5	9.8	15.8	17.8	18.7
	5	3.5	8.2	13.3	21.1	21.8
	6	2.8	6.9	11.2	25.0	31.2

Table 3.1: Geometrical data of the lung model in mm.

For the manufacturing of the model a core was first made of a low melting point alloy (woods metal, ®Alfa Aesar, Germany, melting point: $70°C$). Therefor, the liquid alloy was poured into single negatives of each lung generation. An image of a negative of one bifurcation is shown in Fig. 3.1 a). In order to connect the single bifurcations each single model had a hole in the parent branch and a tip at each daughter branch (see Fig. 3.1 a) and b). Altogether, 63 single bifurcations have been poured.

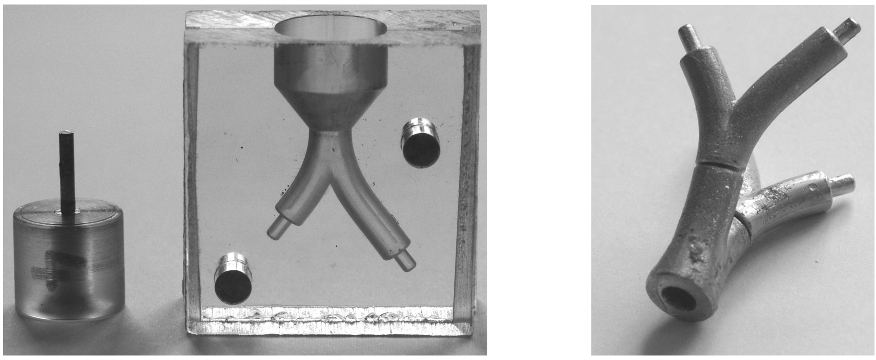
a) b)

Figure 3.1: Negative model of one lung bifurcation made from ®Plexiglas (a), composition of two subsequent bifurcations with a rotation angle of 90° (b).

After solidification of the metal the single bifurcations were connected piecewise to a 3D branching tree with 6 generations. In Fig. 3.1 b) the composition of two subsequent generations is presented. Obviously, the surface quality is very coarse. Thus, the surface had to been smoothened by a water soluble glue. The complete 3D-model (see Fig. 3.2 a)) was placed into a container, that was subsequently filled with transparent silicone (Elastosil, Drawin®, Germany). Finally, the alloy kernel was melted out, such that the flow can enter the model through the trachea and leave it trough the branches of the 6th generation. The final cast model, consisting of the tree of hollow branches, is shown in Fig. 3.2 b).

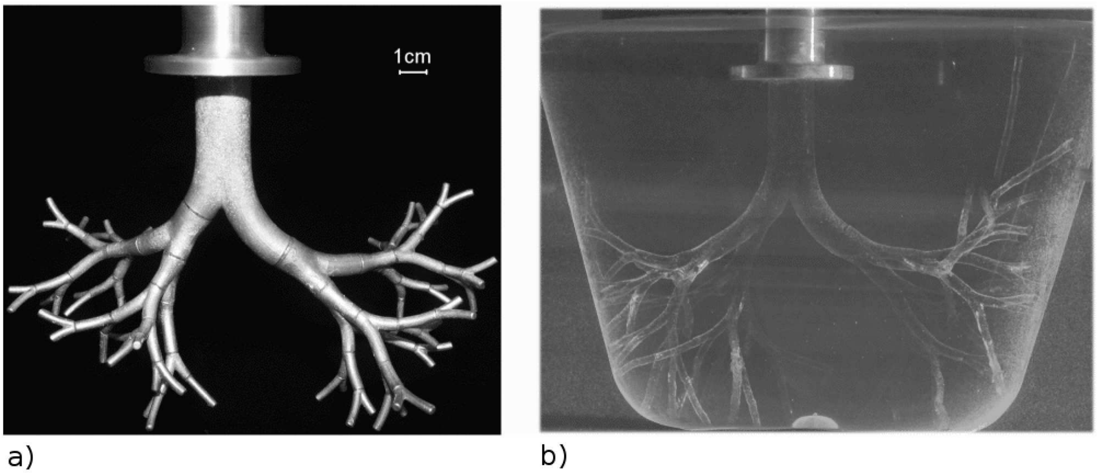

Figure 3.2: Positive model of the human bronchial tree (a), silicone model with hollow branches of the bronchial tree used for flow measurements (b), for this image the model was illuminated by laser light.

3.2.2 Flow parameters

The lung model was submerged in a ®Plexiglas box completely filled with a mixture of glycerine and water (mass ratio 60:40, density $\rho = 1150\,\mathrm{kg/m^3}$, kinematic viscosity $\nu = 8.4 \cdot 10^{-6}\,\mathrm{m^2/s}$) which matches the refractive index of the silicone model ($n = 1.41$). This method allowed to observe the in- and outflow in the complex biological branch geometries using optical flow measurement methods. An oscillatory flow was generated using a linear actuator (MOOG, G400 Series) driving a piston in sinusoidal motion (Fig. 3.3a)). In forward motion of the piston the fluid enters the lung model trough the distal branches in the 6th generation and exits at the trachea. This phase represents the expiration. The reverse flow direction represents the inspiration phase where the piston is retraced to its bottom dead position. A photograph of the test stand during the measurements is illustrated in Fig. 3.3 b). A CCD-camera (PCO 1600, 1600x1200 pixels resolution, 15 fps at full resolution, 2GB RAM) and the laser used for Particle Image Velocimetry (PIV)-measurements are depicted here. The laser is a 120mJ Nd:YAG double pulse laser (Solo XT 120, New Wave) with a wavelength of 532 nm.

The applied parameters for Womersley, Reynolds and Dean numbers in the trachea as well as the according tidal volumes and frequencies used during the measurements are

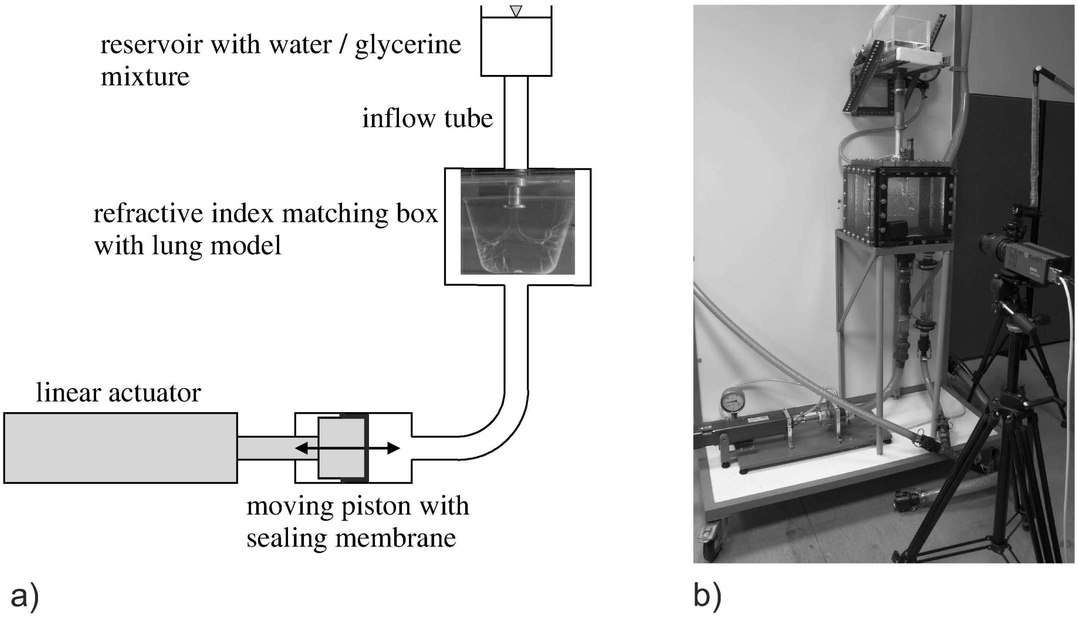

Figure 3.3: Schematic set-up for flow measurements in the lung model at oscillating flow (a), fotograph of the complete test stand including camera and laser (b).

given in Tab. 3.2. Note that two Dean numbers are given here, for the right main branch and for the left main branch. The latter is given in brackets.

case No.	Frequency (Hz)	Tidal volume (ml)	Reynolds number Re	Womersley number α	Dean number Dn
1	0.05	500	670	1.7	270 (330)
2	0.15	500	2020	3.0	820 (1000)
3 (with tube)	0.15	500	2020	3.0	820 (1000)
4	0.3	500	4040	4.3	1630 (2000)
5	0.5	75	990	5.5	400 (490)
6	1.0	75	1980	7.8	800 (980)
7	1.5	75	2960	9.5	1200 (1460)

Table 3.2: Experimental settings and values of the characteristic flow numbers in the trachea, the values for the Dean number Dn apply for the right main branch and for left main branch in brackets.

3.2.3 Particle Image Velocimetry - PIV-Measurements

Flow visualization and PIV-measurements were carried out for the parameters given in table 3.2. For PIV-measurements, small tracer particles are added to the flow which ideally follow the flow with negligible slip. Hence, the particle velocity represents the flow velocity. The particles are illuminated in a plane (light sheet) by two light pulses of a very short interval (few μs). Very frequently, lasers are used for particle illumination due to their high light intensity. The light, scattered by the particles in an angle of 90° is recorded by a camera in two subsequent frames. A typical set-up for PIV-measurements is depicted in Fig. 3.4.

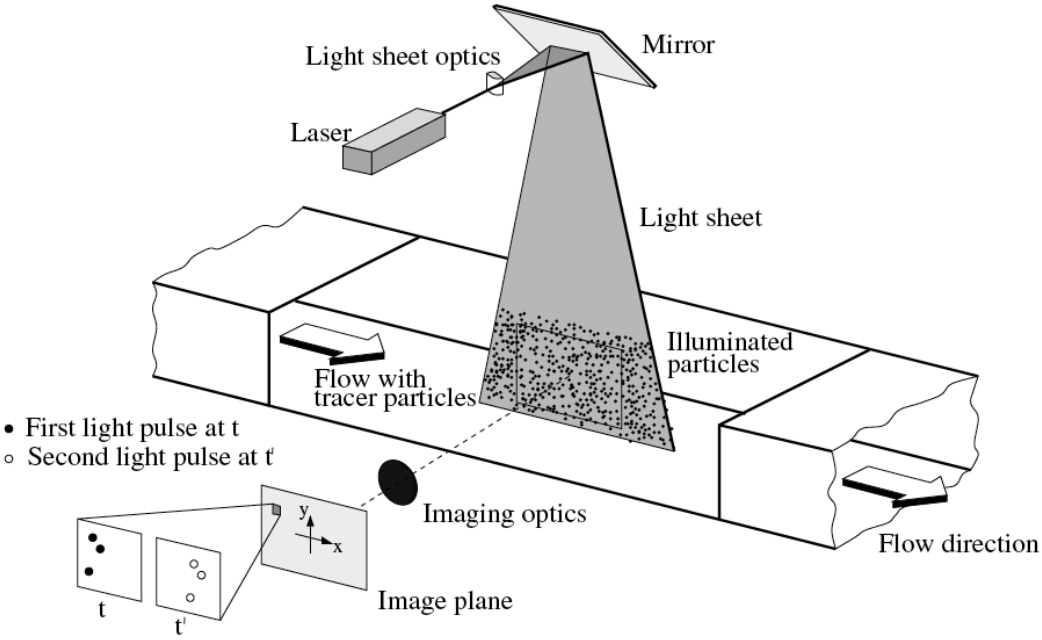

Figure 3.4: Example of a set-up for PIV-measurements in a wind tunnel (from [89]).

For the evaluation of the velocity field the images are first divided into small subareas called *interrogation areas*. Within each interrogation area a certain amount of tracer particles occurs. The particles within one interrogation area are treated as pattern which changes position from the first to the second frame. This pattern is identified in the first and second frame by the method of cross correlation [89]. From the displacement of the particle pattern and the time delay between the subsequent frames the flow velocity can be calculated. It is assumed that the particle motion is linear in the short period of time.

The spatial resolution of the PIV results depends on the size of the interrogation area. The smaller the interrogation size, the higher is the flow resolution. For each interrogation area one velocity vector is received which represents the average velocity of this area. Typically, an interrogation window size of 32x32 pixels is used (see e.g. [45,89]). The quality of cross correlation increases with higher particle density in one interrogation area. In order to ensure 95 % detection rate of the particle patterns, a number of $N > 8$ for particles in one interrogation area is required [56]. Additionally, interrogation areas overlap in order to detect particles that have left into the adjacent interrogation window. Typically, an overlap of 50 % into the vertical and horizontal direction is used.

A representative PIV-image of the upper main branches in the human lung is given in Fig. 3.5. It shows the measurement plane with the distribution of tracer particles.

Figure 3.5: Tracer particle distribution during PIV-measurements in the center plane of the upper branches in the human lung.

For the PIV-measurements carried out here, polyamide-particles with a mean diameter of 20 μm were used as tracer particles. The density of the polyamide-particles is identical to the liquid density ($\rho = 1150\,\mathrm{kg/m^3}$). Hence, a slip error due to gravity does not occur. The error due to particle inertia can be estimated by the Stokes number defined by

$$St = \frac{\tau_r}{\tau_c}, \tag{3.1}$$

where τ_c is a characteristic time scale, in the case of an oscillatory flow it is the periodic time and τ_r is the relaxation time. This time can be calculated by [76]

$$\tau_r = \frac{\rho_p \cdot d_p^2}{18\eta_{fl} \cdot f_w}. \tag{3.2}$$

The variables ρ_p and d_p denote the particle density and diameter, respectively, η_{fl} is the dynamic viscosity of the fluid and f_w is a drag coefficient which can be set to $f_w = 1$ for spherical particles in laminar flow [76] which is assumed for the lung flow. With the parameters of the particles and a dynamic viscosity for the working fluid water-glycerine of $\eta_{fl} = 9.66 \cdot 10^{-3}\,\mathrm{Pa \cdot s}$ a relaxation time of $\tau_r = 2.64\,\mu\mathrm{s}$ is obtained for the particles. The lowest characteristic time scale occurring at the measurements was $\tau_c = 0.6\,\mathrm{s}$ (1.5 Hz).

The resulting Stokes number is $St = 4.4 \cdot 10^{-6}$. According to Dring [23] for Stokes numbers $St < 0.01$ the error induced by particle inertia is below 0.7%, hence the error induced by these $20\,\mu$m particles is even less and can be neglected.

PIV-measurements were done at different planes defined by light-sheet positions of the laser as shown in Fig. 3.6. The flow structure was first analyzed in main flow direction within generation 0 and 1 (light sheet 1). The pulse delay for measurements in main flow direction was set to $90 - 200\,\mu$s and a light sheet thickness of 1.5 mm was applied. Since it is known that the flow through curved tubes and bifurcations is characterized by secondary motions, the secondary flow structure in the trachea (light sheet 2, Fig. 3.6) and in the left branch (in medical sense) of generation 1 (light sheet 3, Fig. 3.6) was also investigated. In order to avoid optical distortions, the light sheet 3 is not perpendicular to the main flow direction of generation 1 but to the Plexiglas-container walls in which the model was placed. The light sheet thickness was increased to 3 mm to ensure the presence of the tracer particles in the first and second illuminated picture. Further, the pulse delay had to be increased to about $1000\,\mu$s in order to resolve the secondary motions.

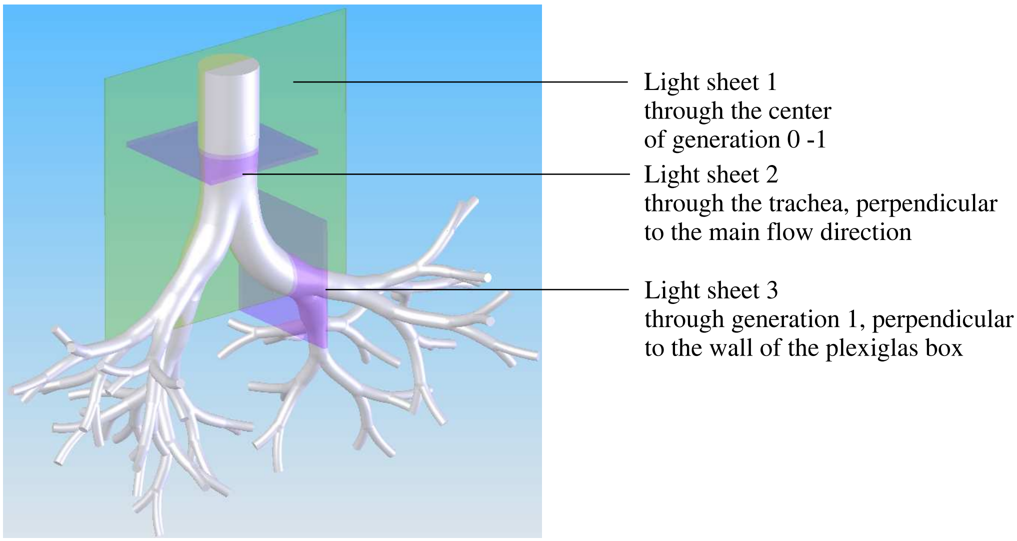

Figure 3.6: Lung model with light sheet position and orientation.

For image evaluation, i.e. cross correlation, an interrogation window size of 32x32 pixel with an overlap of 50 % was applied. Hence, the final grid size is 16x16 pixel. With an average trachea diameter of about 260 pixels in the images, the trachea could be resolved by approximately 16 interrogation windows in radial direction.

3.3 Results and discussion

3.3.1 Flow structure for breathing under rest conditions

The results of the velocity measurement will be presented for four different phase angles within one breathing cycle. The trigger signal was received from an internal position encoder of the actuator (piston). Hence, the trigger time was exactly reproducible. The phase angles are marked with capital letters in Fig. 3.7 which show the piston position of the linear actuator during one breathing cycle. The solid line of the curve represents the expiration cycle, the dashed line the inspiration phase. That means, as the piston is in forward (positive slope) motion, fluid is pushed through the lung model from the 6th generation up to the trachea (compare Fig. 3.2 on page 24), which marks the expiration. The backwards (negative slope) motion marks the inspiration. The zero-crossing marks the maximum velocity of the piston. A total number of 50 subsequent pictures have been taken at every phase position marked in Fig. 3.7 in order to receive a phase averaged result. This number represents a compromise between long term damage of the piston unit due to high pressure loss in the system and a sufficient number of images for mean flow analysis.

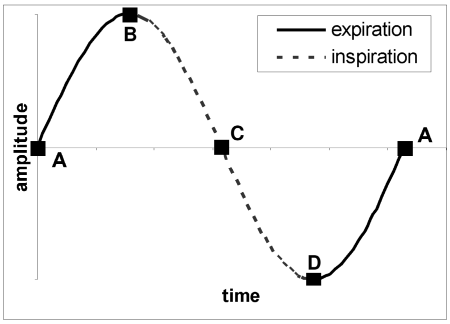

Figure 3.7: Piston movement during one breathing cycle.

The PIV results for different frequencies at the phase positions A, B, C and D are presented in Fig. 3.8. The applied frequencies correspond to normal ventilation conditions. Each image includes the velocity profiles and the color-coded vorticity distribution normalized to the maximum value for the vorticity. It has to be mentioned that, for reference, the left daughter branch (in medical sense) is shown on the right hand side in the subsequent figures.

Phase A: The piston crosses the zero position with maximum velocity, which corresponds to the phase of peak expiration flow. The frequency of 0.05 Hz with a Womersley number of $\alpha = 1.7$ corresponds to quasi-steady flow. At a frequency of 0.15 Hz with $\alpha = 3.0$ and higher, the flow can no longer be regarded as quasi-steady. It is obvious that the flow shown in Fig. 3.8a) is not symmetric. In the trachea the maximum velocity is shifted to the left side at $f = 0.05$ Hz. At 0.15 Hz the maximum velocity in the trachea is shifted to the right side. In contrast the left side is characterized by a large separation region. This separation region is still present at a frequency of 0.3 Hz, although its extension is smaller. It is assumed that this separation is a consequence of the lung model geometry.

Considering the first generation, the velocity maximum at $f = 0.05$ Hz can be found near the inner walls of the bifurcation. For $f = 0.15$ Hz and 0.3 Hz the region of maximum velocity is slightly shifted to the outer walls of the bifurcation. The same effect has been previously described theoretically by Eckmann and Grotberg [25]. For oscillatory flows in curved tubes they observed a shift of the velocity maximum to the inner wall of the curvature which is in our case the outer wall of the bifurcation. This occurs due to the predominant pressure gradient compared to the centrifugal forces at $\alpha \gg 1$. The centrifugal forces usually "push" the fluid to the outer wall in steady flows. Since the distance at the inner curvature is shorter than at the outer wall the pressure gradient has increased and consequently the velocity at the inner wall. This effect becomes more pronounced with higher Womersley numbers. The contour plot of the vorticity represents the shear rates that occur within the lung model (Fig. 3.8). The maximum vorticity during expiration is at about $300 s^{-1}$ and occurs in the separation regions.

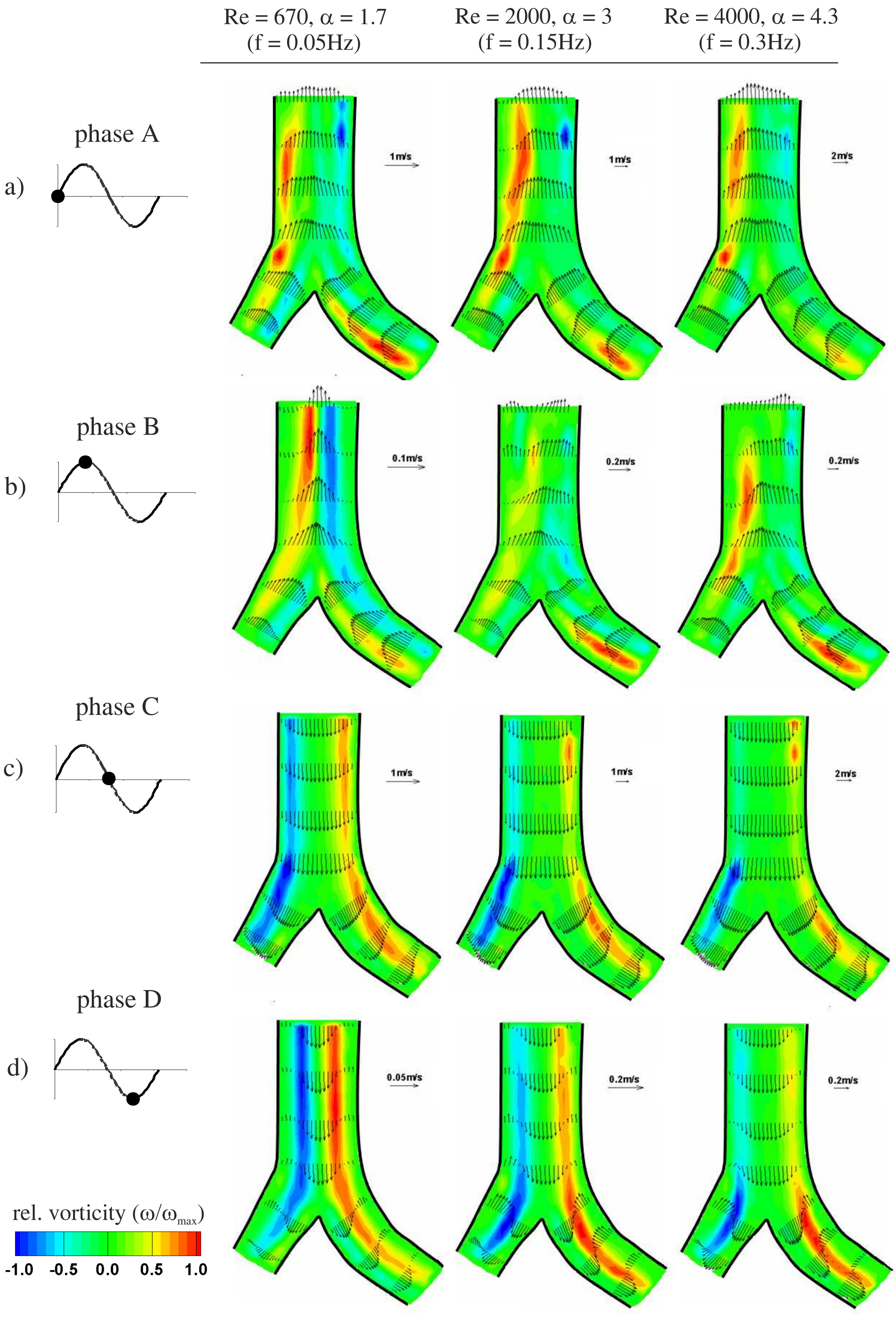

Figure 3.8: Velocity profiles and relative vorticity contour plots at phases A-D during normal breathing, diagrams denote the respective piston position at each phase.

Phase B: The piston has reached its top dead end and the flow in the lung changes direction from expiration to inspiration (Fig. 3.8b)). At a frequency of 0.05 Hz the reverse of the flow is nearly axisymmetric in the trachea which confirms the quasi-steady flow conditions. At higher frequencies/Womersley numbers the symmetry is broken. The flow starts turning at the separation region in the trachea. Flow transition is initiated in regions of low velocity, i.e. low inertia.

Phase C: This phase denotes the maximum inspiration (Fig. 3.8c)). At a frequency of 0.05 Hz the velocity profile in the trachea is characterized by a nearly parabolic shape. The maximum velocity in the daughter branches occurs near the inner walls of the bifurcation due to centrifugal forces. During expiration this region was characterized by a velocity minimum. Considering the whole breathing cycle, the transformation of the velocity profiles creates a steady net mass flow of "fresh" fluid into the model along the centerline and the inner walls of the bifurcation. This is compensated with a net mass outflow of "old" fluid to the trachea along the outer walls of the bifurcation. This effect may be attributed to steady streaming in bifurcations first mentioned for the lung by Haselton & Scherer [43].

At increasing frequency/Womersley-numbers the parabolic velocity profile in the trachea is more flattened. However, the M-shaped velocity profile which typically occurs in oscillatory tube flow for $\alpha \geqslant 3$ [105] could not be observed.

The region of the peak velocity is again slightly shifted to the outer walls of the bifurcation with increasing Womersley-number, which was already stated during peak expiration, nevertheless the peak velocity can is still located near the inner walls of the bifurcation (outer walls of the bend). Comparing the results for inspiration and expiration, the vorticity contour plot reveals a more symmetric pattern during inspiration. The highest values of the vorticity occur in the first generation. Whereas in the trachea, the velocity profiles are more homogenous which leads to low shear rates and vorticity, respectively.

Phase D: This phase again represents the peak amplitude of the piston and its velocity is zero. The lung flow changes its direction from inspiration to expiration. The phase shift of the flow can be well seen (Fig. 3.8d)). The core flow in the trachea is still directed downwards into the lung, while the flow near the wall already moves out. In the daughter branches this reverse flow is similar for all Womersley numbers. However, in the trachea, the reverse of the core flow is increasingly shifted in phase with higher α. This could be a consequence of the larger velocity during peak inspiration.

3.3.2 Flow structure with endotracheal tube

In a clinical situation, the patient will be ventilated using a tube, which means a change of the inflow conditions. To study this effect on the flow structure, a typical ventilation tube with an inner diameter of 9.5 mm was inserted into the lung model. The flow was again analyzed by PIV in the measurement plane defined by light sheet 1 (Fig. 3.6). As the flow leaves the tube it enters the trachea in form of a jet (Fig. 3.9 a) and b)). Further downstream, the flow is characterized by large separation regions near the outer bifurcation walls and by unsteady vortices in the shear layer. The ventilation has changed dramatically as compared to flow without tube. Fig. 3.9 demonstrates the strong influence of the tube position on ventilation. A slight shift of the tube to the right side (Fig. 3.9 b)) leads to preferred ventilation of the right branch.

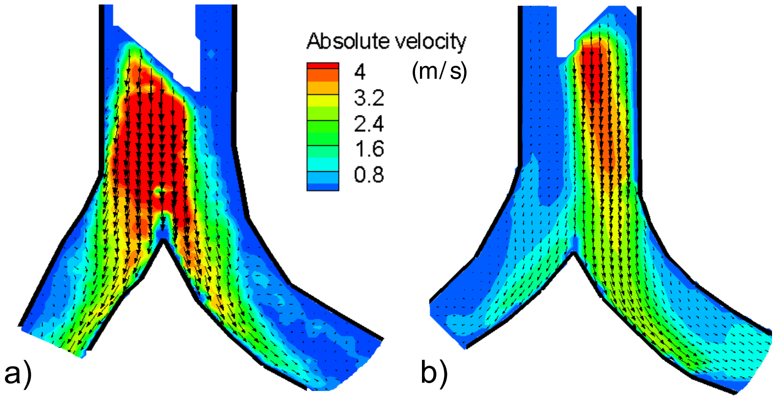

Figure 3.9: Peak inspiration through endotracheal tube, velocity vectors and magnitude, tube position in the trachea centre (a), tube position slightly shifted to the right branch (b), $Re = 2000$, $\alpha = 3$.

However, during the expiration phase the influence of the tube vanishes. The flow with and without tube is similar as shown in Fig. 3.10. This means that the flow disturbances induced by the tube jet during the inspiration are not conserved until the expiration phase.

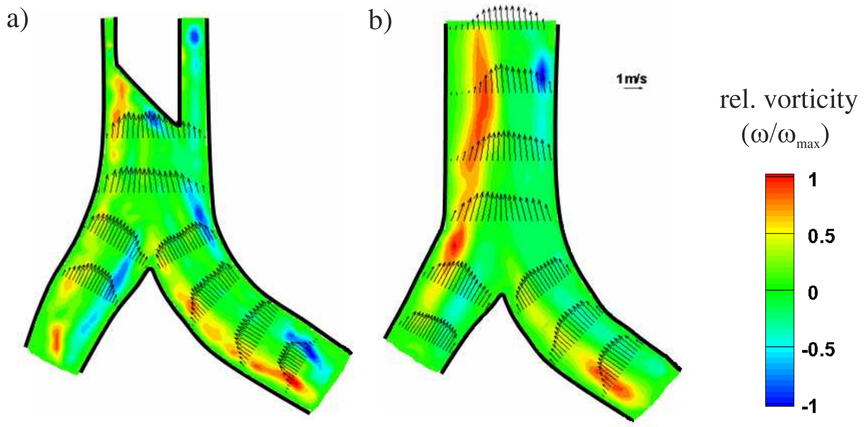

Figure 3.10: Comparision of peak expiration with tube (a) and peak expiration without tube (b), color-coded is shown the contour plot of the vorticity in relation to the maximum vorticity superposed with velocity profiles.

3.4 Results for HFOV

Figure 3.11 represents the results for high frequency conditions for the same phase angles as during normal ventilation conditions (compare Fig. 3.8). The vorticity values are again normalized with the maximum vorticity. The case of $\alpha = 9.5$ corresponds to 3 Hz used in clinical treatment. Higher frequencies could not be realized due to the high pressure loss and limitations of the linear actuator.

Phase A: Fig. 3.11a) shows the results at peak expiration. It can be seen that for all cases the velocity profiles in the daughter branches are skewed to the inner walls of the curvatures as already stated during normal breathing conditions. A parabolic velocity shape can be found in the trachea for all Womersley numbers. A comparison with the results at normal breathing conditions for this phase shows that during HFOV the flow structure is more symmetrical, especially in the trachea the separation region has vanished. Furthermore, the overall vorticity is much higher than during normal breathing. This is in particular the case in the trachea, where the maximum vorticity occurs with values of $600\,\mathrm{s}^{-1}$. The vorticity strength has doubled from normal breathing to HFOV, despite of the same Reynolds number for the cases of $f = 0.15\,\mathrm{Hz}$ and $f = 1\,\mathrm{Hz}$. That means the shear rates have increased during HFOV.

Phase B: In contrast to breathing under rest conditions an initial point for the reverse flow can not be identified during HFOV.

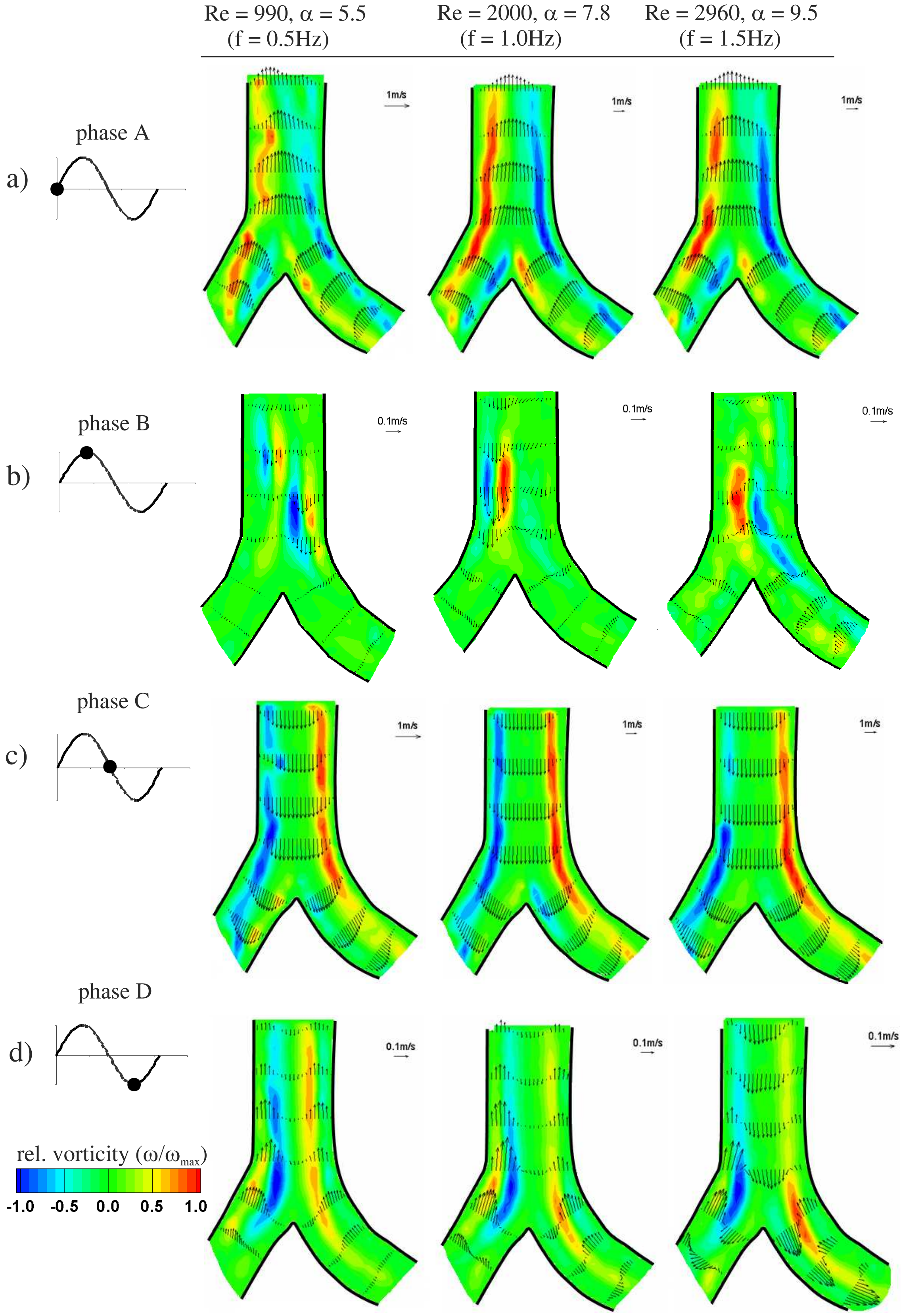

Figure 3.11: Velocity profile and relative vorticity contour plot at phases A-D during HFOV.

Phase C and D: Qualitatively, the results are similar to the inspiration phase. The maximum vorticity occurs again in the trachea, whereas the velocity profiles in the first generation are more homogenous and less skewed than during normal breathing leading to lower vorticity.

Increasing the Womersley number leads to a more flattened velocity profile (Fig. 3.11c)) and the shift of the velocity maximum to the outer walls of the bifurcation as already observed during normal breathing. The typical phase shift of velocity profiles between the core flow and near wall flow could be observed during the changes of flow direction (Fig. 3.11d) and Fig. 3.12). In comparison to the lower frequencies, the phase shift of the flow in the daughter branches is no longer symmetrical. For $f = 1.5\,\mathrm{Hz}$, Fig. 3.11d) reveals a higher velocity into the lung at the right main branch. The consequence is a net mass flow from the left to the right branch which is visualized by the streamlines in Fig. 3.12 for $\alpha = 9.5$. Hence, with increasing frequency the tendency of cross exchange of mass between the daughter tubes increases. This type of mass exchange is already known as pendelluft [64] but so far it has been attributed mainly to the flow in the lowest generations near the alveoli. Note that Fig. 3.11d)) represents the phase averaged results, hence the direction for the pendelluft does not change periodically, but remains constant, which was also confirmed by the instantaneous PIV results. This allows to conclude that the Pendelluft correlates with the local topology of the lung.

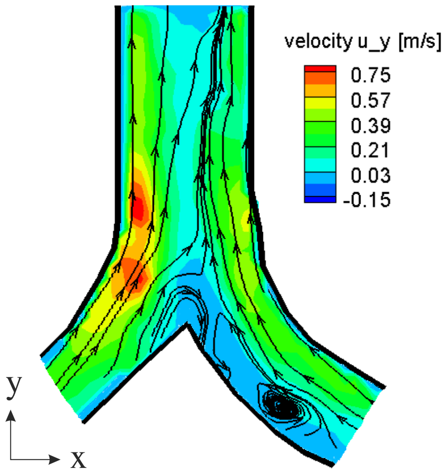

Figure 3.12: Transition from inspiration to expiration during HFOV, $Re = 2960$, $\alpha = 9.5$, color-coded velocity in the y-direction with red indicating positive (outflow) direction and blue indicating negative (inflow) direction, superposed are streamlines.

3.4.1 Cross sectional flow

The secondary motions in the model were measured in cross sections of the trachea and of the left daughter branch, respectively, again during phase angles A-D. The location of the cross sections was shown in Fig. 3.6 (light sheets 2 and 3). This was only done for a frequency of $f = 0.5\,\mathrm{Hz}$ since for higher frequencies the main flow velocity was too high to guarantee that the particles remain in the laser light sheet during the PIV measurements. The Dean number for this case is $Dn = 400$.

Secondary motions in the trachea

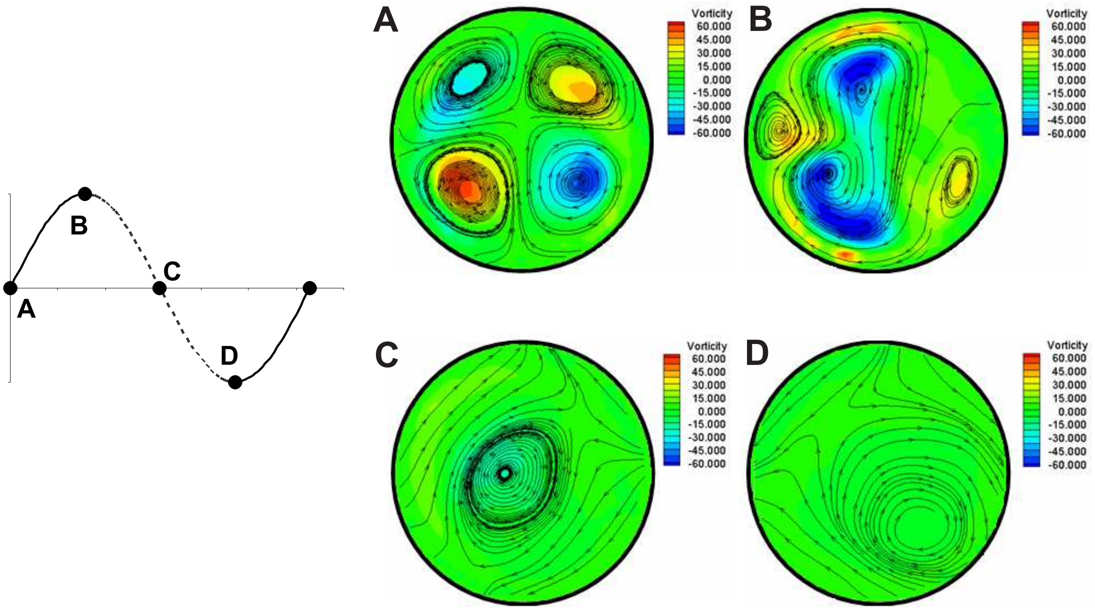

Figure 3.13: Sectional streamlines and streamwise vorticity in the cross section of the trachea at phase angles A-D, $Re = 990$, $\alpha = 5.5$; the diagram represents positions of the piston at distinct phase angles.

Fig. 3.13 presents the results for the secondary flows in the trachea. During peak expiration (phase A) two pairs of counter-rotating vortices are generated within the trachea as marked by the different senses of orientation of the streamlines. The vorticity marks the strength of the vortices. Red color indicates high vortex strength with positive orientation, blue, high strength with negative orientation. The double vortex pair is a consequence of the vortex pairs approaching from each daughter generation. A similar flow structure was also presented in Fresconi and Prasad [31].

The secondary flow in the transition phase B is still characterized by a double vortex structure, even with a similar strength as during peak expiration. The intensity of the secondary vortices seems to remain constant during the expiration phase.

During peak inspiration (phase C) the flow is characterized by a very slight swirl. It is assumed that the swirling is a result of the inflow from a water reservoir. During transition from inspiration to expiration (phase D) the double vortex structure already starts to form.

All results presented here show the phase averaged flow structures. Considering the instantaneous PIV results, especially during expiration, leads to the assumption that there are only weak differences concerning the secondary flow structure. That means that regardless of the flow history in the lower branches, which is most likely not identical from period to period, the flow structure in the trachea remains approximately unaffected.

Secondary motions in the first daughter branch

During peak expiration (phase A) an asymmetric swirl structure can be observed in the first daughter branch (Fig. 3.14, Phase A). The symmetric double vortex observed in the trachea has seemingly vanished. It is assumed that this asymmetric structure occurs due to the asymmetric, three-dimensional geometry of the airway model. In a study by Fresconi and Prasad [31] the secondary motions were symmetric for all branches. However, their

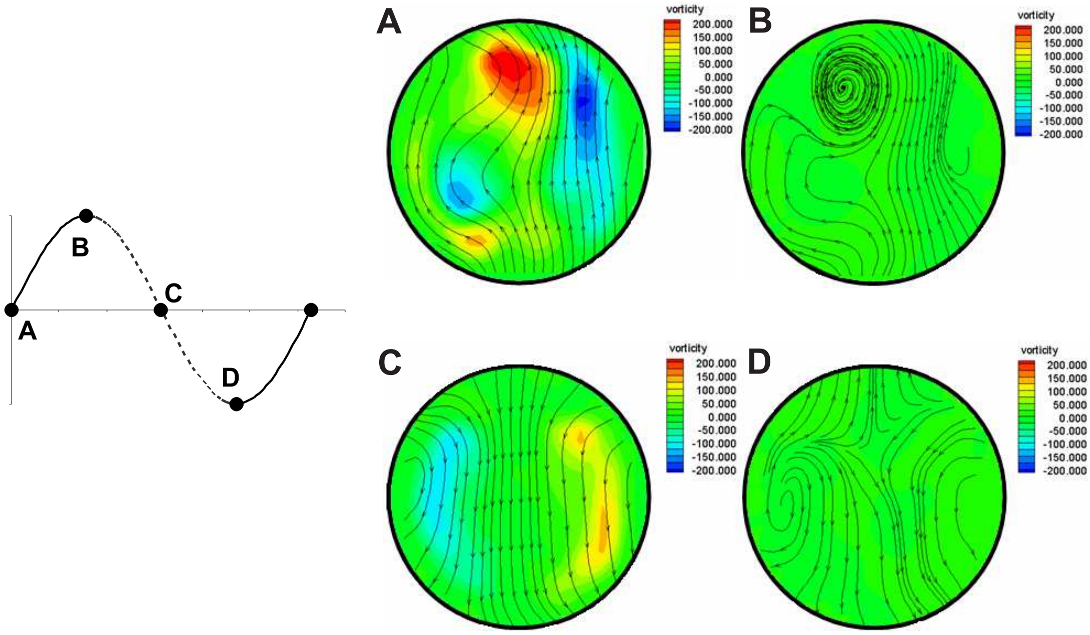

Figure 3.14: Section streamlines and streamwise vorticity in the cross section of the right branch of the first generation at phase angles A-D, Re = 990, α = 5.5, diagram represents positions of the piston at distinct phase angles.

model was symmetric and plain. Therefore, it is assumed that this asymmetric vortex structure would rather occur in a real lung.

During peak inspiration, the typical vortex pair for curved tubes can be observed Fig.3.14, Phase C). Note that the streamlines do not show closed circular patterns because the light sheet position is not perfectly perpendicular to the main flow direction. Thus, the resulting vectors show a superposition of main flow and secondary flow. Nevertheless the qualitative structure of the secondary flow can still be recognized. During the reverse flow (phases B and D, Fig. 3.14) the secondary flow is characterized by unstructured vortices.

3.5 Conclusions

In this study the flow in a realistic 3D model of the upper human lung airways was investigated experimentally by means of PIV-measurements. The lung model used here was computer-generated; hence, each bifurcation can be described analytically. Therefore, it is possible to create reproducible models and compare the experimental results to those obtained by numerical calculations. Note, that the studies presented herein represent a case where the outflow conditions at the 6th generation are governed by nearly constant pressure without additional resistance or compliance. However, the real lung structure from the 6th generation down to the alveoli acts as an additional impedance which will be considered in a subsequent study (Chapter 6).

The experimental investigations presented here were performed for normal breathing conditions and high frequency ventilation using PIV measurements. For higher frequencies, a shift of maximum velocity to the outer wall of the bifurcation (inner wall of the bend) could be observed. The velocity profiles in the first generation are less skewed during high frequency ventilation. Besides pendelluft, this effect might be a further explanation for a more homogenous distribution of mass during HFOV. Nevertheless, the velocity maximum still occurs for all frequencies near the inner wall of the bifurcation. In contrast, the maximum velocity occurs near the outer wall of the bifurcation during expiration. Consequently, a simultaneous net mass outflow of used air and net mass inflow of fresh air into the lung is created.

Using an endotracheal tube in the lung model creates a completely different inflow situation. During mechanical ventilation, the correct tube position is very critical since it strongly influences the quality of ventilation. If the position is not correctly centered in the trachea, e.g. the tube is shifted to the left side, mainly this part of the lung is ventilated which might lead to lung overdistension. However, this effect could also be used as advantage to guide the air preferentially into collapsed lungs regions without overdistension of healthy parts. It has to be mentioned that the tube only changes the inflow conditions but not the outflow which is similar to normal breathing without tube.

Furthermore, the complete lung is characterized by secondary flow structures occurring during the whole breathing cycle. The secondary flows contribute to a lateral mixing in the human lung. During one breathing cycle, the secondary flows change their structure according to the main flow direction. However, considering the instantaneous, phase locked PIV-measurements, there is only a weak variation of the secondary flow structure in the trachea, especially during expiration. That means, there are no fluctuations between subsequent breathing cycles. The symmetric secondary flow patterns in the cross sections suggest, that the asymmetrically bifurcating lung geometry does not influence the secondary flow.

A comparison of both ventilation conditions, CMV and HFOV, revealed only slight differences between the flow patterns. At HFOV the flow is more symmetrical in the trachea during expiration. During change from inspiration to expiration a mass exchange between the daughter generations was found, which could not be been seen during normal breathing conditions. This mass exchange could be attributed to pendelluft and is a consequence of the asymmetric lung topology which determines the local pressure loss in the model and therefore apparently predicts the mass flow direction of the pendelluft.

4 Numerical study of the flow in the human lung

4.1 Objective

The experimental investigations have still left several open questions since measurements could be carried out only at selected regions within the model. Since the model provides the great advantage that it was computer generated, an identical model for numerical simulation is available. These simulations are part of the ongoing and future work. With the numerical simulation three dimensional structures can be visualized as well as flow information even in the lowest generations of the lung model can be received. The numerical simulations were carried out with the open source software *OpenFoam V.1.51 dev.* The most important results of the first numerical simulations will be presented here.

4.2 Numerical model

The governing equations for incompressible, unsteady fluid flow are the continuity equation and the Navier-Stokes-equations. In tensor notation they are

$$\frac{\partial u_i}{\partial x_i} = 0, \tag{4.1}$$

$$\frac{\partial u_i}{\partial t} + u_j \frac{\partial u_i}{\partial x_j} = -\frac{1}{\rho}\frac{\partial p}{\partial x_i} + \frac{\partial}{\partial x_j}\left(\nu \frac{\partial u_i}{\partial x_j}\right) + g_i, \tag{4.2}$$

where u_i and u_j are the components of the velocity vector, p is the pressure, ρ and ν the fluid density and kinematic viscosity, respectivly. Here, the Einstein summation is used so that the repeated index implies summation. Furthermore, an additional volume force is considered here which includes the gravity g since for comparison to the experimental results, the properties of the experimental liquid (water-glycerine) were invoked.

Numerical Methods

For numerical simulation of the lung flow, the Finite Volume Method (FVM) was applied. Therefore, the equations 4.1 and 4.2 were integrated over a control volume and then discretized. The FVM requires a decomposition of the field of interest into grid cells. The discretization of the governing equations is invoked at the knots of the numerical grid. After discretization, a linear set of equations is received which are solved by the solver

GAMG (Geometric Agglomerated algebraic MultiGrid solver) which is implemented in OpenFoam. This solver first coarsens the grid to approximate a fast starting solution for a finer grid [7]. All methods applied for numerical flow simulation are summarized in Tab. 4.1

Mathmatical operation	Numerical method
spacial discretization of convective terms	Gauss upwind, 1st order
discretization of time derivatives	backward differencing scheme
pressure-velocity coupling	PISO algorithm

Table 4.1: Numerical methods for simulation of the lung flow.

The PISO algorithm mentioned in table 4.1 stands for Pressure Implicit with Splitting of Operators [110]) whereat two interpolation loops were employed, here. The iterations, necessary to calculate the solution of each time step, were stopped as a truncation error of 10^{-8} was reached.

Numerical grid model

The lung model which has been described in section 3.2.1 was also used for numerical flow simulation. It was discretized by 1,926,391 tetrahedral cells which form an unstructured mesh. The mesh was created with ICEM CFD V.11 from ANSYS. Fig. 4.1a) depicts the discretized lung model. The enlarged views show the grid structure of the inlet boundary with a diameter of 18 mm (Fig. 4.1b)) and one of the outlet boundaries (Fig. 4.1c)) with a diameter of only 2.8 mm.

It can be seen that the grid resolution is still quite coarse, especially in the tube center and in the complete cross section of the lowest branches. The boundary layer in the tubes with large diameter is well resolved. However, in order to receive a fully mesh independent solution a total number of about 100,000-150,000 cells per bifurcation would be necessary [12]. Given the bifurcation number of 63 in our lung model, this leads to about 10,000,000 cells. A refined mesh with such a large number of cells leads to a calculation time of more than one year for just one period (with the currently available computer resources), even though the calculation could be parallelized. Hence, only the coarse grid was used so far for flow simulation.

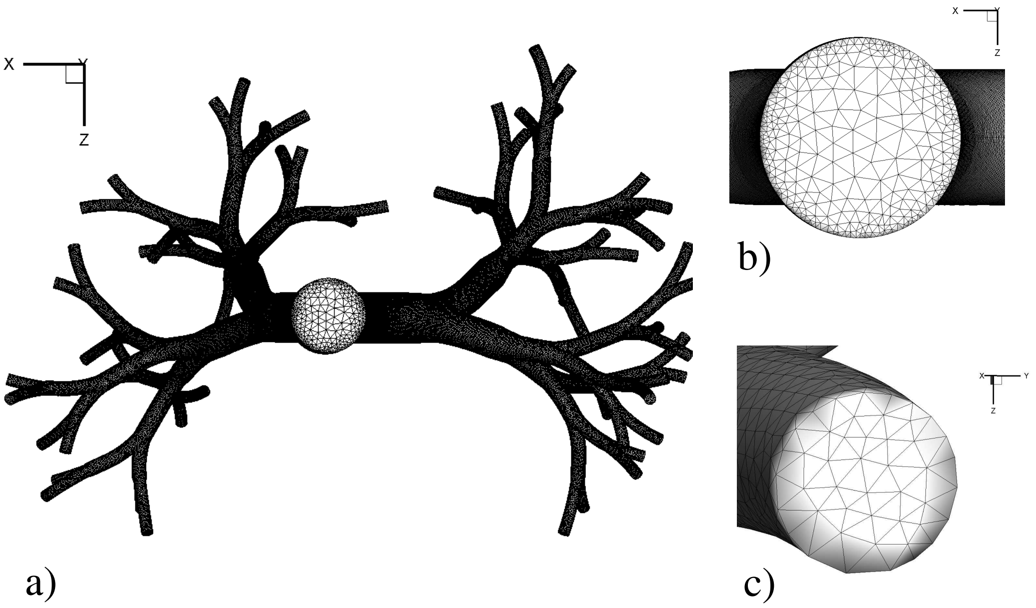

Figure 4.1: Numerical grid structure of the lung model, a) complete lung model, b) enlarged view of the grid structure of the inlet boundary (top of the trachea), c) enlarged view of the grid structure of one of the outlet boundaries (distal end of the 6th generation).

Boundary and Starting conditions

The linear set of equations can only be solved if both, starting and boundary conditions are available. The complete region of interest is initialized with zero pressure relative to the ambient pressure and zero velocity. For boundary conditions two different types of boundary conditions are used:

- Dirichlet boundary condition: a value of the variable is given
- Neumann boundary condition: a derivative of the variable is given

Boundary conditions have to specified for the inlet, the outlets and the wall, whereat the lung model contains one inlet and 64 outlets. The positions of the boundary conditions are depicted in Fig. 4.2.

The boundary conditions used for the simulation of the human lung flow are summarized in Tab. 4.2.

The values given in Tab. 4.2 apply perpendicular to the boundaries. The maximum velocity $\underline{u}_{max}$ was determined according to equation 2.3 on page 19. The velocity was applied as uniform value at the inlet boundary. Therefore, the inflow tube (trachea) was lengthened to a total tube length of 20 cm in order to receive a more developed flow at

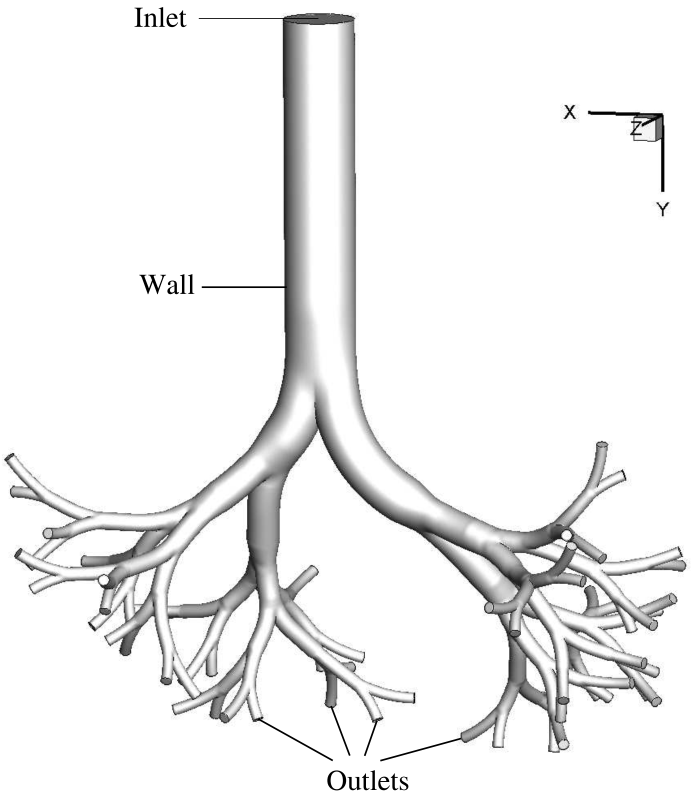

Figure 4.2: Lung model with the positions of the boundary conditions.

Boundary	Variable	Condition	Type
Inlet	velocity u	$\underline{u} = \underline{u}_{max} \cdot sin(\omega t)$	Dirichlet
	pressure p	$\underline{n} \cdot \bigtriangledown p = 0$	Neumann
Outlet	velocity u	$\underline{n} \cdot \bigtriangledown \underline{u} = 0$	Neumann
	pressure p	$p = 0$	Dirichlet
Wall	velocity u	$\underline{u} = 0$	Dirichlet
	pressure p	$\underline{n} \cdot \bigtriangledown p = 0$	Neumann

Table 4.2: Boundary conditions for the simulation of human lung flow.

the first model bifurcation. The original tube length of the model was 12 cm. In the experimental set-up, the trachea was also artificially lengthened due to the inflow tube, as shown in Fig. 3.3. According to Durst [24], the entrance length l to receive fully developed flow in a tube depends on the tube diameter D and the Reynolds number Re:

$$l = \left[0.619^{\frac{1}{6}} + (0.0567 Re)^{\frac{1}{6}} \right]^{\frac{1}{6}} D. \tag{4.3}$$

Equation 4.3 is valid for laminar pipe flow in the range of $0 < Re < \infty$ [24]. For a Reynolds number of $Re = 2000$ and a tube diameter of 18 mm an entrance length of 22 cm would be necessary to receive fully developed flow. Hence, the tube length of the trachea in the numerical model represents a very good compromise between reliable results and numerical effort due to a large geometry, which needs to be discretized.

The numerical simulations were performed on the PC Farm Deimos of the ZIH (Center for Information Services and High Performance Computing) at the Technische Universität Dresden. Altogether, Deimos consists of 2576 processor cores [54] of which 64 were used. The time step size was varied between 10^{-4} s and $5 \cdot 10^{-4}$ s depending on the oscillatory frequency of the lung flow. With this time step size the average duration of the calculation of one period is about 48 h.

4.3 Validation of the numerical results

For validation of the numerical code, a comparison to the experimental PIV-results of the first bifurcation is given. First, the case of normal breathing under rest condition is chosen. The Reynolds number is $Re = 2000$, the Womersley number is $\alpha = 3$. Figs. 4.3 and 4.4 depict the velocity contours and profiles in the center plane of the main branches for inspiration and expiration, respectively. The comparison of inspiration shows good agreement of PIV-measurements and numerical results (Fig. 4.3). The regions

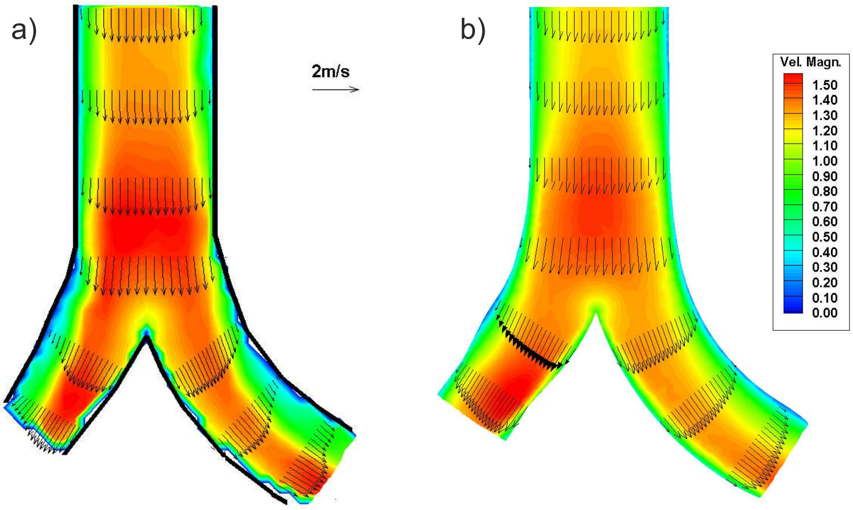

Figure 4.3: Velocity contours and profiles during peak inspiration, PIV - results (a), numerical results (b), $Re = 2000$, $\alpha = 3$.

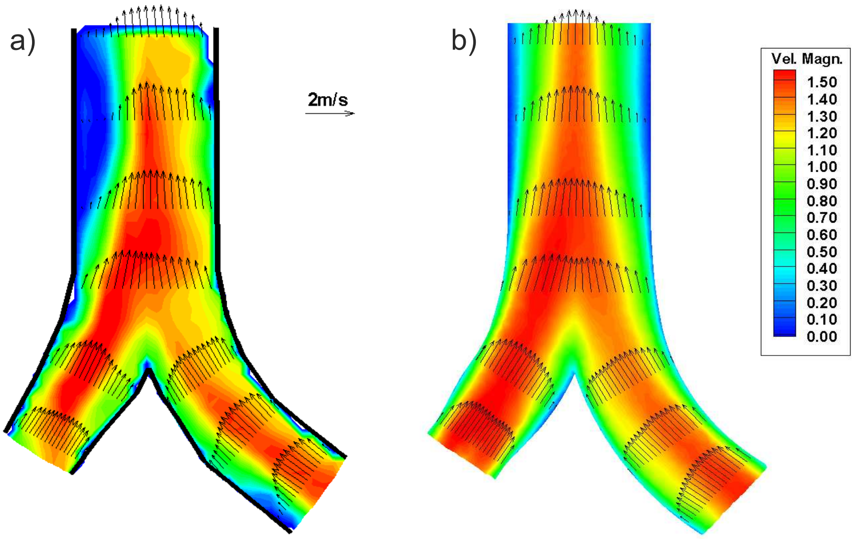

Figure 4.4: Velocity contours and profiles during peak expiration, PIV - results (a), numerical results (b), $Re = 2000$, $\alpha = 3$.

of high velocity have similar extensions. During inspiration the acceleration of the flow ahead of the bifurcation is found in both cases. A small deviation occurs for the velocity profiles which have higher gradients near the wall in the PIV - measurements. A possible explanation could be the numerical grid, which might be too coarse to fully resolve the stokes boundary layer, especially in the lower branches. Furthermore, the peak velocity at the top of the trachea is higher than in the numerical calculation, probably due to a shorter entrance length of the numerical model.

During expiration (Fig. 4.4) the numerical and experimental results are still in acceptable agreement. The velocity is in a similar range for both cases and the velocity profiles are characterized by a comparable asymmetry.

The PIV-measurements suggest a separation region in the trachea which does not occur in the numerical calculation. However, this separation region was only observed experimentally for this single case of Re and α given above. Therefore, it is not assumed to be typical for the flow in the lung model and the numerical data should be correct for this case.

The cross sectional flow is compared for one case of high frequency ventilation with $Re = 1000$ and $\alpha = 5.5$ (compare Tab. 3.2 on page 25). Fig. 4.5 shows the flow patterns in the cross section of the trachea during maximum expiration. For the exact position of the cross section, refer to Fig. 3.6 on page 28. Fig. 4.5 a) presents the experimental result, Fig. 4.5 b) the numerical result, whereat the color coded contour of the vorticity is superposed with the cross sectional stream lines.

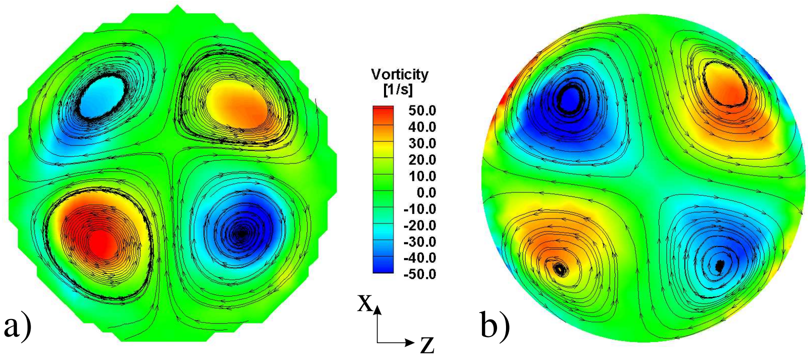

Figure 4.5: Vorticity contours, color coded, where blue indicates clockwise (negative) and red counterclockwise (positive) sense of rotation, respectively, superposed are cross sectional streamlines, $Re = 1000$, $\alpha = 5.5$, (a) PIV - results, (b) numerical results.

Qualitatively as well as quantitatively there is a good agreement between both results. The double vortex pair occurs in both cases at even similar strength. The vortex structure of the numerical simulation is more symmetric than the experimental result and the vortex shapes vary slightly.

To conclude, based on the validation results, the numerical simulation can be used to predict the flow behavior in regions, at which experimental data are not available. There are small deviations concerning the velocity profiles in the first daughter branch. These can have different reasons. First, the numerical grid is quite coarse considering the cross sectional resolution of the flow. Thereby, small structures were probably not fully resolved. Second, the size of the interrogation areas, chosen for the PIV-evaluation, also determines the resolution of the experimental results. Here, the distance of two grid points was about 1.1 mm. Hence, the trachea was resolved by approximately 16 grid points. Since this resolution is also quite coarse, it is possible that small flow details are not resolved due to the averaging of the velocity field across one interrogation area. Nevertheless, both, experimental and numerical results are in good agreement with results from other researchers presented in the literature, e.g. [12,20,31,63,64,90] and typical flow phenomena could be shown.

4.4 Numerical results

Numerical results are given for the velocity distribution by iso-surfaces of the velocity magnitude. Fig. 4.6 shows the surface of constant velocity vector magnitude of $0.95 m/s$ for peak inspiration (a) and peak expiration (b) during normal breathing.

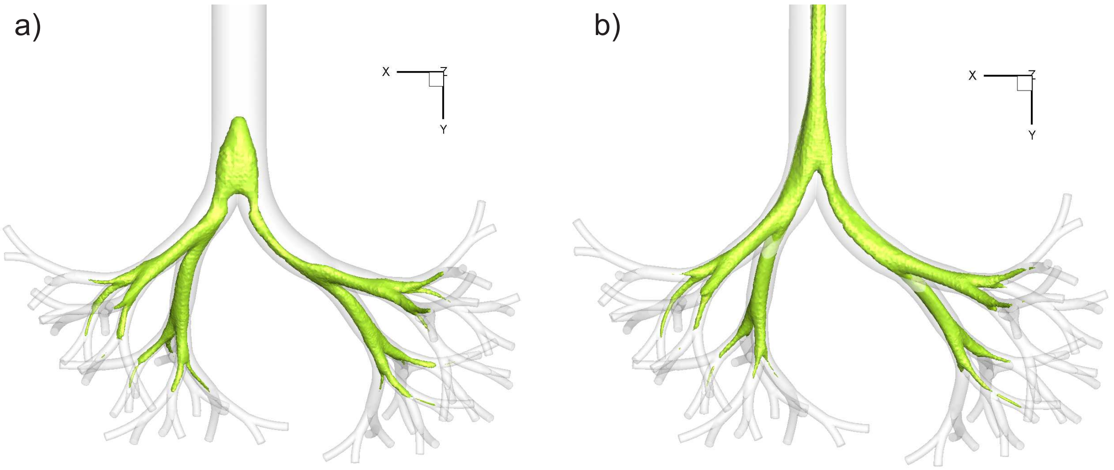

Figure 4.6: Iso-contours of the velocity magnitude for $0.95 m/s$ for peak inspiration (a) and peak expiration (b), $Re = 2000$, $\alpha = 3$, the complete lung geometry is superposed.

During inspiration, the velocity seems to increase from the trachea down to the 3rd generation as marked by the increasing area which is occupied by the iso-surface (Fig. 4.6a)). This can be explained by the slightly decreasing total cross section area down to this generation. Ahead of each bifurcation, a further increase of velocity occurs, which is also caused by the contraction of the flow at this point. The orientation of the iso-surface changes strongly from generation to generation. The fluid is always pushed to the outer walls of the curvature as already found in the experiments. The distribution between left and right main branch is asymmetric which is obviously a consequence of the smaller curvature radius of the right main branch and hence, a higher pressure loss.

At the first glance, the iso-surfaces of the same velocity during expiration show a similar distribution as for inspiration (Fig. 4.6b)). Even these branches of the 4th generation which were characterized by higher velocities during inspiration show enlarged contour surfaces during expiration. This means that the pressure loss difference between the branches is the same for inspiration and expiration.

However, a closer look at the iso-surfaces reveals their different shape during inspiration and expiration. During inspiration, the contours are curved following the branch geometry, while during expiration, the contours appear to run straight through the branches. As already observed in the experiments, the location of the same velocity contour has shifted. Additionally, the three-dimensional shapes of the iso-surfaces have changed. In the left branch of the first generation the surface has the largest extension in z-direction (during inspiration). In the trachea, the maximum extension of the iso-surface occurs in the x-y-plane. In contrast, during expiration, the directions of the maximum extension are twisted. In the first generation, the maximum extension occurs in the x-y-plane, in the trachea, it occurs in the perpendicular y-z-plane.

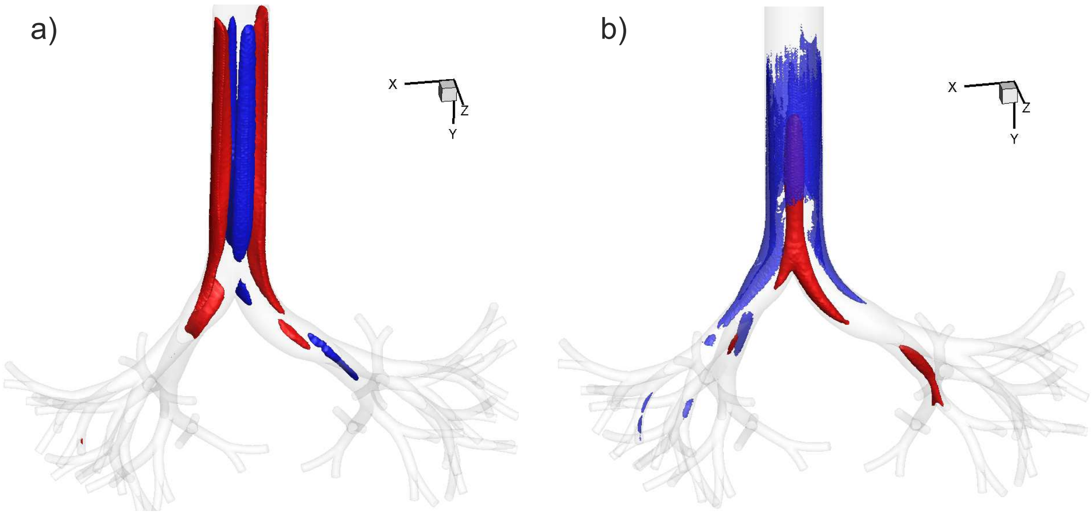

Figure 4.7: Iso-contours of the y-velocity during transition from expiration to inspiration (a) and from inspiration to expiration (b), red and blue color indicates positive and negative velocity in the y-direction, respectively.

The transitions from expiration to inspiration and from inspiration to expiration are shown in Fig. 4.7 a) and b), respectively. The figures represent the iso-contours of the y-velocity, where red contours mark positive flow direction (downwards into the lung), while blue contours mark negative flow direction (upwards). The phase shift of the flow during the transition times can be clearly seen. Fig. 4.7 reveals a characteristic structure of the transition zones. Typically, the return of the flow is initiated in the low inertia zones, in particular, zones of lower velocities. During change from expiration to inspiration (Fig. 4.7a)) two pairs of characteristic zones emerge in the trachea. On the left and right sides, the flow is directed into the model (red structure), i.e. the inspiration has already started, whereas at the front (anterior) and rear (posterior) center of the trachea, expiration (blue structure) still takes place. A comparison to the iso-contour during maximum expiration reveals that the maximum flow velocity occurs in the y-z-plane. Hence, the plane of lower inertia flow is the x-y-plane in which the change of flow direction is initiated.

During change from inspiration to expiration (Fig. 4.7b)) the flow structure is completely different. The core flow is still directed into the lung, whereas at the wall an annulus of fluid is already directed upwards.

Considering the secondary flows in a realistic lung geometry, their structure varies strongly even within one branch. Experimentally, the flow in two selected planes in the trachea and left branch of the first generation was analysed and presented above. It was assumed that these secondary flow structures are representative for the selected branches. Now, as numerical data are available, the secondary flow structure can be visualized in the complete model. Fig. 4.8 shows the iso-contours of the helicity for peak inspiration and expiration for normal breathing. The helicity is a measure for the strength of helical structures. It is defined by

$$H = \underline{u}(\bigtriangledown \times \underline{u}), \tag{4.4}$$

whereat a scalar value is received. Color coded, the helicity represents the different senses of rotation, i.e. red - positive, clockwise rotation, blue - negative, counterclockwise rotation and the shape of the helical vortices can be seen.

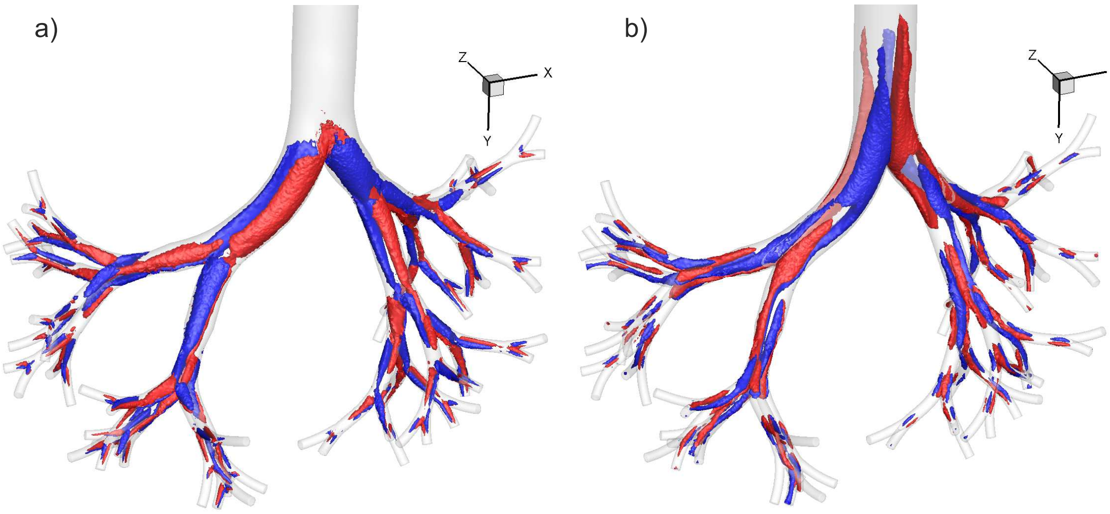

Figure 4.8: Iso-contours of the helicity during peak inspiration (a) and expiration (b), red indiciates positive, clockwise rotation, blue - negative, counterclockwise rotation.

During inspiration (Fig. 4.8 a), a vortex pair, can be found in each generation of the model. The extension of the vortex pair is maximal at the beginning of each generation and decreases slightly at the end. The helicity magnitude is preserved again down to the 3rd generation and decreases slightly further downstream, which can be seen from the smaller iso-contour surfaces. Consequently, it is assumed that the secondary vortices scale with the local velocity which remains constant down to the 3rd generation.

During expiration, the PIV results have shown a double vortex pair in the trachea (compare Figs. 3.14 and 3.13 on page 38). This structure was not observed in the first branch. Now, the complete structure of the vortex generation in the whole model can be visualized (Fig. 4.8 b). It can be seen that the double vortex pair starts to form upstream at each bifurcation originating from a single vortex pair which approaches from the two daughter branches. Further upstream, the double vortex pair vanishes due to the influence of the curvature of the branches. Hence, a new vortex pair is generated at the outside of the bend. As no curvature exists, which is the case in the trachea, the vortex only loses strength. The maximum secondary velocity found here is about 20% of the average main flow velocity, which is in agreement with Ref. [32].

To confirm the assumption that the vortices scale with the local main velocity, i.e. Reynolds number, the velocity vectors in combination with the helicity contours are illustrated in Fig. 4.9 for two different Reynolds numbers, $Re = 2000$ (Fig. 4.9 a) and $Re = 3000$ (Fig. 4.9 b). Each image shows the same cross section of the first generation (upper cross section in Fig. 4.10). It can be seen that for $Re = 3000$ the helicity is about three times higher than for $Re = 2000$. The in-plane velocity has approximately doubled. This means that secondary vortex strength strongly increases with higher Re and the relation is not linear. These findings are in contrast to Fresconi and Prasad [32] who stated that up to a critical Reynolds number of $Re = 100$, secondary vortex strength increases linearly with Re and above this number, the vortex strength remains nearly constant.

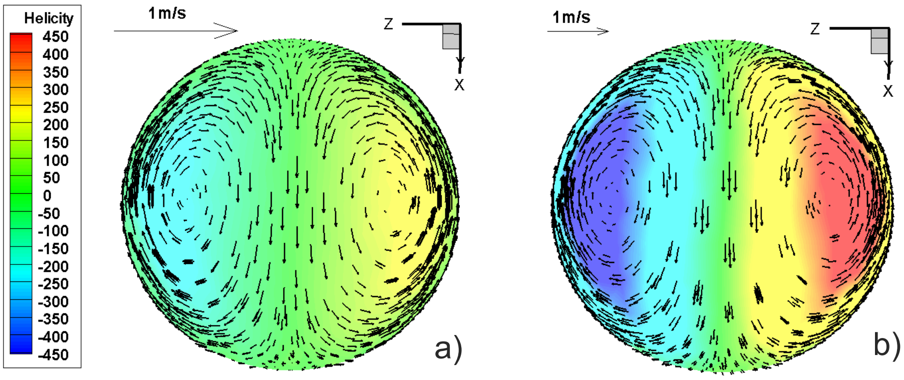

Figure 4.9: Velocity vectors and contour of the helicity in a cross section of generation 1 for two different Reynolds numbers, a) Re = 2000, b) Re = 3000.

In order to gain more information about the vortex structure, different planes of the first and second generation are selected and the in-plane streamlines are plotted (Fig. 4.10). At the beginning of each branch the vortex pair is symmetric and well pronounced, the strength is maximal. Further downstream, it loses strength and the characteristic symmetric vortex pair vanishes. The sectional streamlines rather indicate a single swirl. At the bifurcation, two new vortex pairs start to emerge.

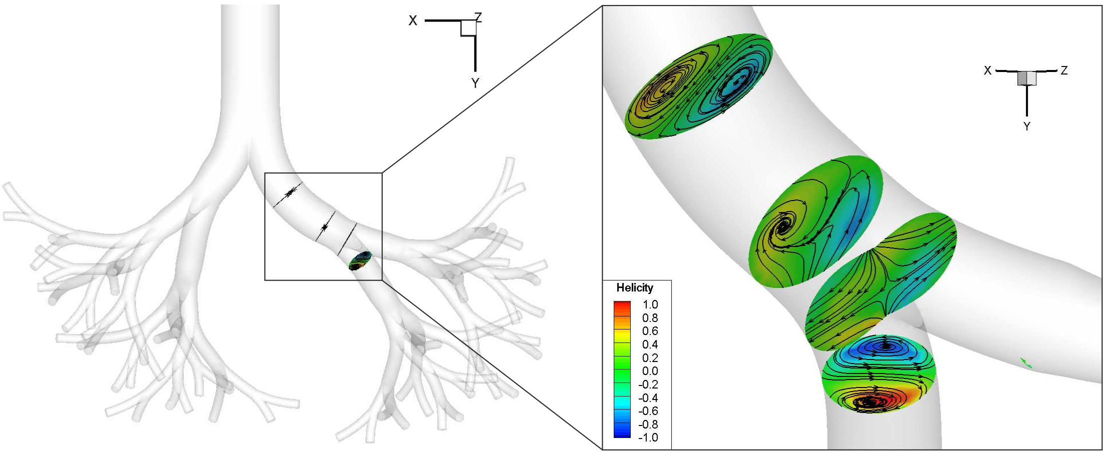

Figure 4.10: Secondary flow structures in selected cross section of the right main branch, color contours represent the helicity, superposed are in-plane streamlines.

These numerical results show that structure of the secondary vortices strongly varies along the branch. Hence, the experimental measurements were apparently carried out in a plane in which the vortex structure has vanished. This finding is in contrast to Fresconi and Prasad [32] who assumed a constant vortex structure throughout the complete branch.

4.5 Conclusions

The numerical simulation was in good agreement with the experimental results. Hence, flow phenomena which could not be measured were visualized by numerical data. At the times of flow transitions from ex- to inspiration and ins- to expiration, the flow is bidirectional due to the phase shift of oscillatory flow; characteristic regions with different flow directions develop. These regions reflect the different flow structure during ins- and expiration. Since during expiration the maximum flow velocity occurs in the y-z-plane in the center of the tube, the return of the flow has to be initiated at the outside of the perpendicular x-y-plane. During inspiration such a characteristic plane of maximum velocity does not develop. Hence, the flow starts turning annularly close to the wall. Furthermore, it could be shown that vortical structures occur in all generations during inspiration and expiration. Vortex pairs are generated during inspiration in each branch by centrifugal forces. Due to the change in curvature and bifurcating geometry, vortex pairs are not conserved beyond a bifurcation but rather develop anew. In contrast, the vortex pairs from the daughter branches unite in the parent branch to two vortex pairs during expiration. However, halfway through the tube the vortex pairs have vanished and start to develop again. Consequently, the flow structure depends on the local curvature and does not have a history from the upstream flow.

5 Visualization of mass flow distribution

5.1 Objective

The method of HFOV is frequently used and well established for clinical treatment of pediatric diseases. However, the overall cycle-to-cycle net transport mechanisms including all currently known effects (for details refer to literature review (Chapter 2) are still not fully understood.

Fredberg et al. [30] have shown that the local distribution of air and the change of the pressure in the alveoli can be influenced when the ventilation frequency is close to the resonant frequency of the local lung region. They further speculated that by variation of the frequency and the pressure distribution, the ventilation of different areas of the lung can be controlled. Based on this idea, this study will focus on flow partitioning visualized by advecting particles at flow conditions characteristic for HFOV. The probability distribution of particles representative for mass transport in different branches of the lung will be investigated here under varying boundary conditions. Therefore, the long-term particle motion within the in-vitro lung model is analyzed. This model is identical to the one, which was used in the previous study (chapter 3).

5.2 Experimental methods

5.2.1 Flow parameters

The characteristic flow parameters which were chosen for the subsequent experiments are summarized in Tab. 5.1.

The tidal volume used in clinical HFOV ($TV \approx 60 - 100\,\mathrm{ml}$) usually represents $40 - 70\%$ of the geometry dead space. The dead space of the model used here is only $60\,\mathrm{ml}$ due to the limited number of bifurcation generations. In order to keep the same volume ratio the tidal volume was reduced to $30 - 50\,\mathrm{ml}$ in the experiments. Typical frequencies applied during HFOV are between 3 and $10\,\mathrm{Hz}$ [117]. With the values given above, Reynolds numbers for clinical HFOV can vary between 2500 and 14000, Womersley numbers between 9 and 18. Consequently, the characteristic flow parameters applied during these experiments are in the lower range of clinical HFOV in real lungs and slightly below, respectively.

Tidal volume (ml)	Frequency (Hz)	Reynolds number $Re_{trachea}$	Womersley number $\alpha_{trachea}$	Corresponding frequency in air (Hz)
30	0.5	400	5.5	0.9
30	1.0	800	7.8	1.9
30	1.5	1190	9.5	2.8
30	2.0	1590	11.0	3.7
30	2.5	1980	12.3	4.6
40	0.5	530	5.5	0.9
40	1.0	1060	7.8	1.9
40	1.5	1590	9.5	2.8
40	2.0	2120	11.0	3.7
50	0.5	660	5.5	0.9
50	1.0	1320	7.8	1.9
50	1.5	1980	9.5	2.8
50	2.0	2650	11.0	3.7

Table 5.1: Experimental settings for visualization of the distribution of mass.

5.2.2 Visualization technique

In this section, the visualization technique to measure mass flow distribution is presented. Therefore, larger particles with a mean diameter of 200 μm were used which were visualized directly. These particles were again neutrally buoyant polyamide tracer particles with a density of $\rho = 1150 kg/m^3$. For an approximation of their ability to follow the flow with negligible slip error, the Stokes number has to be calculated again.

At the given maximum frequency of 2.5 Hz and a particle size of 200 μm the resulting Stokes number is $St = 6.6 \cdot 10^{-4}$. Since for $St < 0.01$ the response error of particles due to velocity changes is below 0.7%, the slip velocity error may still be neglected.

In order to observe the cycle to cycle transport effects within the lung the model was free of particles at the beginning of each measurement. Just before the piston motion was started a bolus of fluid (1 ml) with 300-350 particles was inserted into the system at the top end of the trachea and their positions were recorded thereafter over a large number of ventilation cycles. The number of particles was counted by visual inspection of the bolus in a small glass tube prior to injection to ensure that a similar number of particles was used in each experiment.

A lab-made telecentric background illumination with parallel light allowed to obtain a projection of all particles in the lung model onto a single CCD-sensor (Fig. 5.1). The telecentric set-up consisted of 3 lenses as shown in Fig. 5.1.

Since, in the projection the branches overlap only in very small areas, we could distinguish the different paths of the particles in the network just by the known geometry of the bronchial tree. The particle motion in all branches of the 3D lung model could be recorded simultaneously. Uncertainty due to superposition of particles at the same x-y position and different z-positions could be neglected because of the low particle concentration.

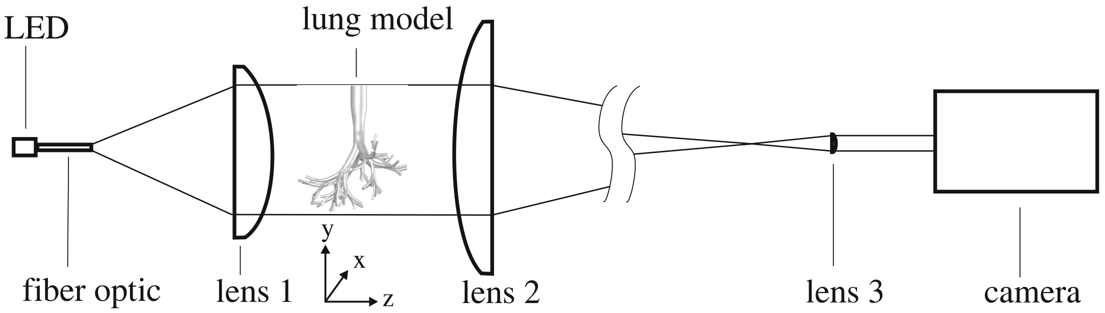

Figure 5.1: Schematic set-up for telecentric image acquisition, including the optical paths.

A pulsed light emitting diode (LED) was used as light source (GaAlAs super bright light emitting diode, model: 383URC-3, Roithner Lasertechnik). It was driven by a constant current of 1 A with a pulse duration of 1 μs. A fibre optic was connected to the LED scattering the light beam by an angle of 60° at its end.

The advantage of an LED is that the intensity of all light pulses is identical since the emitted light intensity is proportional to the current through the LED. Furthermore, due to the method of back light illumination, the whole lung model was illuminated homogeneously without speckle noise whereas the illumination by a laser beam would cause a Gaussian distribution of light intensity on the images. Thereby, it was very important to cover this illumination set-up from ambient light. This would lead again to different light intensities on the images.

The camera used for image acquisition is a high speed camera (Photron APX RS) running with a resolution of 512x512 pixels. The frame rate for image recording was adapted according to the applied frequency which was in the range of 65-230 frame per second (fps). For an adequate displacement of particles between subsequent pictures, 130 images per period were recorded. Consequently, the displacement of particles between two subsequent images remained in the same range despite varying frequencies at constant tidal volumes. With the given image resolution a total number of 8192 could be saved on the camera memory chip. This leads to a number of 63 ventilation periods which could be recorded.

5.2.3 Image processing

Subsequently, the image processing steps to achieve a final result of the particle probability distribution are explained. First, the method to separate the moving particles from the background of the images is described.

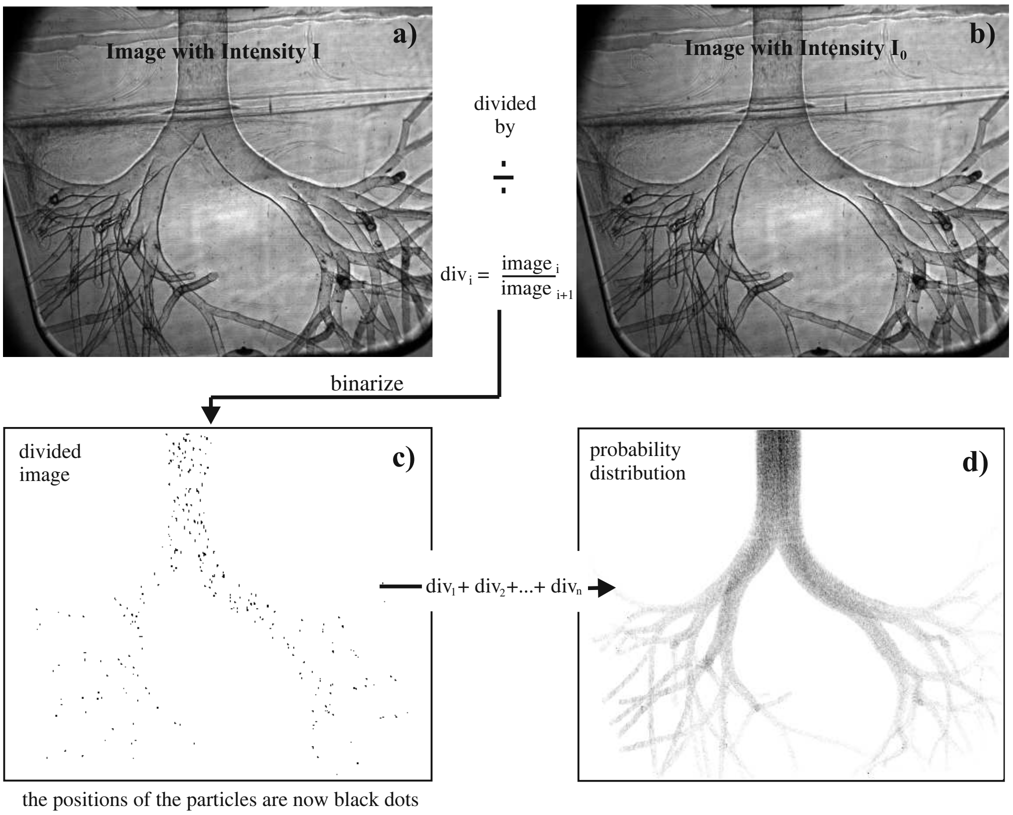

Figure 5.2: Flow chart for image evaluation, (a) originally recorded image, (b) subsequent original image, (c) image after division of two subsequent images with particles shown as black dots, (d) superposition of all images of one data set representing probability distribution, darker regions denote higher particle probability.

The raw data are long sequences of images containing the particle position represented by a gray value distribution between 0 (black) and 255 (white). Particles can be identified as dark shadows on a lighter background (Fig. 5.2a) and b)) with a typical diameter of 1.5 pixels. To separate the particles from the background, each image was divided pixel by pixel by its subsequent picture. As a result regions of moving objects appear as dark pixel areas whereas the stationary background of the lung model becomes bright (Fig. 5.2c)). This image processing technique is only possible because of the constant light intensity of each LED pulse. The two images are identical except for regions where particles have moved within the time span between two successive images. The dividing technique is especially suitable for the method of backlight illumination since a constant background can be completely eliminated. The division of a picture by a reference picture is based on equation 5.1 for the modulation of parallel light.

$$I(x,y) = I_0(x,y) \cdot m(x,y), \tag{5.1}$$

In equation 5.1 $I(x,y)$ denotes the light intensity measured at a pixel at the position x and y. $I_0(x,y)$ is the intensity of the reference image at this position and $m(x,y)$ denotes the modulation of light produced by an object. Here, it is basically the shadow of the particles which modulates the light (since they are much larger than the wavelength of the light). Therefore, the image with intensity I corresponds to each frame (Fig. 5.2a)), I_0 to the successive frame of the frame series (Fig. 5.2b)). The divided image (Fig. 5.2c)) contains only the information of the modulation function due to the moving particles and is therefore completely independent from the intensity distribution of the background. Fig. 5.2d) shows the final particle probability distribution, which will be explained in the next paragraph.

5.2.4 Calculation of the Probability distribution

The resulting modulation of light $m(x,y)$ of the divided images was then inverted and binarized by the application of a suitable threshold according to equation 5.2 and a new modulation function $M(x,y)$ was received:

$$M(x,y) = \left\{ \begin{array}{lll} 0 & for & 1 - m(x,y) < 0.85 \\ 1 & for & 1 - m(x,y) > 0.85 \end{array} \right\}. \tag{5.2}$$

In the new images, which contain the information of the modulation function $M(x,y)$, the pixels of the value 1 represent the positions of the moving particles and the background has the value 0 (black). The probability $\phi(x,y)$ of particles, passing a certain location (x,y) in the images n, was determined by the following equation

$$\phi(x,y) = \sum_{n=1}^{N} \frac{M_n(x,y)}{max(\phi)}. \tag{5.3}$$

The variable N denotes the total number of images (130 x 63 ventilation periods = 8190). The higher the value $\phi(x,y)$ the more often particles have passed a specific position (x,y) in the images of the branching network (maximum 100%). At positions never passed by a particle the value remains zero. The maximum probability value which was calculated was $max(\phi) = 63$, only. This value is the reference value of 100% for all experiments. The theoretical maximum of 8190 was not reached, firstly due to the method of inserting a small definite number of particles at the beginning of each measurement, secondly particles leave the model over time either at the inlet trachea or at the distal outlets.

The aim of the analysis was to compare the particle probability representative for mass transport within the lung for different non-dimensional parameters applied during ventilation. Consequently, the absolute values are less important compared to the relative deviations between the results. Therefore, all values were scaled with the maximum of 63. For visualization of the probability distribution in an 8bit image, the range was stretched to span the color range from 0 to 255 now representing 100%.

The probability distribution of the final image as shown Fig. 5.2d) was inverted for better visualization. Here, the darkest pixels represent highest particle probability. This probability density of particles is representative for the flow partitioning in the upper airways of the human lung. The speckled intensity distribution is due to discrete distribution of particles. For the parameter settings given in Tab. 5.1 each measurement was repeated 10 times and averaged in order to receive statistically reliable results of the particle probability. Thereby, the results become independent of the initial particle locations in the bolus (initial boundary conditions) and of slight variations of total particle numbers in each experiment.

5.3 Results and discussion

General probability distribution

A typical probability distribution is presented for $\alpha = 11.0$ and $Re = 1590$ in Fig. 5.3, where the probability distribution is color-coded. Since the bolus was inserted at the entrance of the trachea the highest probability values occur within this region since particles oscillate in the trachea and the main branches during several ventilation cycles until they enter the lower generations. The probability decreases while moving deeper into the network. Nevertheless, particles occur in all lower branches of the model. Although the tidal volume for the case presented in Fig. 5.3 was only 50% of the model's dead space mass transport is observed through all branches. Transport phenomena such as steady streaming, pendelluft and trap and release effects [77] contribute to an effective exchange of mass within the lung.

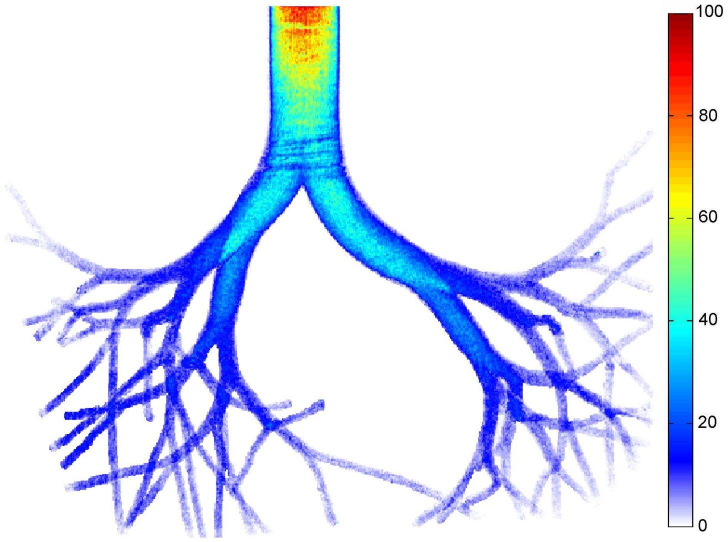

Figure 5.3: Relative particle probability distribution in the lung model exemplarily for $\alpha = 11.0$ and $Re = 1590$, color scale represents probability values in % related to the maximum value of 63.

Parameter variations - Reynolds number effects

In Fig. 5.4 the results for constant Womersley numbers (within each row) but increasing Reynolds numbers are shown. For comparison of the probability distribution, three contour lines, each representing one specific contour level, are shown. The extension of the contour lines of the same probability can be interpreted as penetration depth of the particles into the different branches. Comparing the low Womersley number cases ($\alpha = 5.5$, first row), a symmetric probability distribution with a value of 15% can be seen in the daughter branches of the left main branch. The Reynolds numbers are approximately in the same range between 400 and 600. Consequently, differences between the maximum penetration depths are small and only slightly increased at $Re = 660$. Even though the tidal volume has almost doubled from 30 ml to 50 ml its influence on probability distribution is only marginal. One exception is the probability in the second generation of the

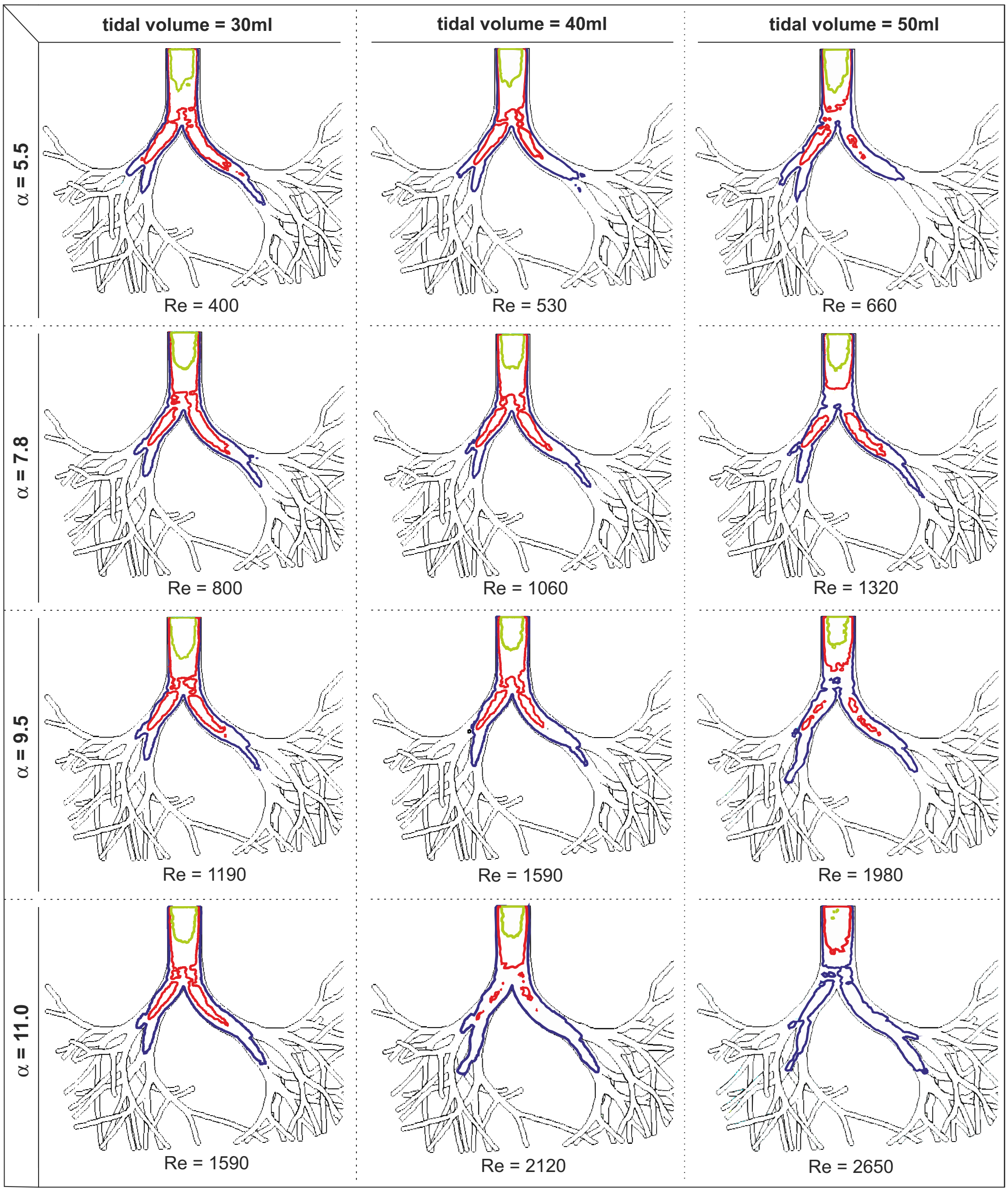

Figure 5.4: Contour lines of probability distributions within the human lung model for varying Womersley and Reynolds numbers, green contour lines represent 50% probability, red 30% and blue 15%.

right lobe at $Re = 400$. Here, the probability is higher than for $Re = 530$ and 660. A possible explanation is that particles need more cycles in the main branches before they reach lower generations and axial streaming is reduced. Hence, particle probability in the generations 3-6 has to be significantly lower at $Re = 400$ compared to $Re = 530$ and 660. The symmetric distribution in the second generation of the left lobe is due to the low Reynolds number. The pressure loss in the lower branches is small and therefore, the pressure distribution between parallel branches remains homogeneous. Consequently, mass is equally distributed and the influence of asymmetric geometry seems to be negligible.

Comparing the cases with $\alpha = 11.0$ (last row in Fig. 5.4), variations in penetration depths are more significantly pronounced due to the larger increase of the Reynolds number from 1590 to 2650. It can be observed that the symmetric distribution found for low Re and α has changed. Now, the inner branches of the second generation mark the preferred pathways as marked by the contour lines for 15% probability. In those generations, characterized by a strong change of curvature, lower probabilities are found. Strong changes in flow direction lead to increased pressure loss and hence to an asymmetric pressure distribution within parallel branches.

The phenomenon of preferred pathways was already found for steady flow by Snyder et al. [96] who observed flow partitioning non-uniformly among daughter branches with the medial branches receiving a greater proportion of the flow than the lateral branches, especially at increased Reynolds numbers. Furthermore, as the penetration depth increases for higher Re the contours for the probability of 15% are narrowed in the main daughter branches. As also stated by Fresconi and Prasad [33] the particle penetration is stretched axially leading to higher probability in lower generations due to increased axial streaming.

In contrast, the extension of higher probability contour lines has strongly decreased. The contour lines of 50% probability at $\alpha = 11$ and $Re = 2650$ have almost vanished, the contour line of 30% can only be observed within the trachea. A shift of probability distribution has occurred leading to lower probabilities in the main upper airways and higher probabilities in the lower generations. It can be assumed, that particles reach the lower generations within a shorter period of time. An improved mass transport through the lung bifurcations at higher Reynolds numbers associated with higher tidal volumes was also described by Fang et al. [27] and Tarbell et al. [101]. At larger Re the concentration profile is skewed to the inside wall of the bifurcation in the branches with strong curvature. In general, for increasing Reynolds number, centrifugal forces increase and thus the secondary motions which result in enhanced mixing and streaming processes as well as in augmented dispersion. The distorted concentration profiles mimic the velocity profiles described in Adler and Brücker [1]. The agreement of velocity and concentration profiles for curved tubes has previously been stated by Eckmann and Grotberg [25] based on theoretical investigations. At increasing tidal volume and Reynolds number, mass transport is enhanced due to higher concentration in the regions of higher velocity. Therefore mass transport in curved tubes exceeds that of oscillatory flow in straight tubes.

Comparing the results for the same tidal volume (refer to each column in Fig. 5.4) but increasing Womersley number, an even larger increase of penetration depth could be observed for the cases with a tidal volume of 40 and 50ml. At constant tidal volume the values of Womersley and Reynolds numbers were changed simultaneously. Hence, effects of Womersley and Reynolds number could not be separated. This observation of increased penetration depths at constant tidal volume is in contrast to the suggestions of Fang et al. [27] who drew the conclusion that tidal volume plays a more important role in mass transport than the frequency. However, their assumptions are based on mass transport by steady streaming per ventilation cycle. Here, the results represent probability distributions over a larger number of cycles. Time-dependent effects such as pendelluft or steady streaming accumulate. Therefore, it is reasonable that the results, presented here, differ from those of Fang et al. [27].

Womersley number effects

Fig. 5.5 displays the results for constant Reynolds number (each row) but increasing frequency. The probability distribution is again coded by iso-contour lines.

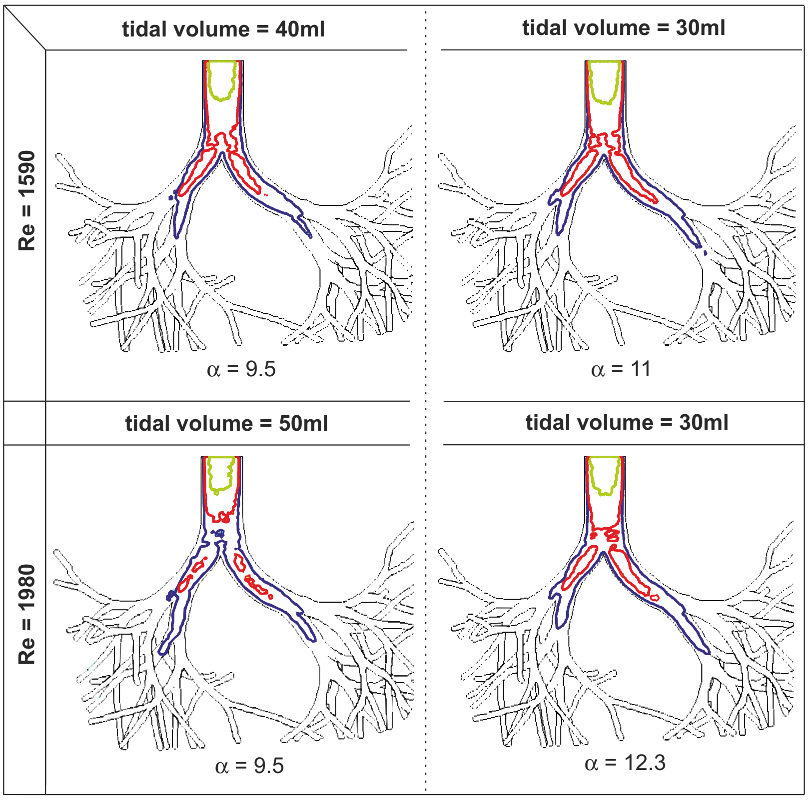

Figure 5.5: Contour lines of probability distributions within the human lung for different Womersley but constant Reynolds number, green contour lines represent 50% probability, red 30%, blue 15%.

Due to the already high Reynolds numbers, preferred pathways into the inner branches could be observed for all cases. However, for the cases of higher Womersley number the probabilities within each branch are more homogeneous. The radial extension has increased as can be seen from the contour profiles. Additionally, in the second generation at the right-hand side of the lung model a higher penetration depth can be found for lower tidal volume but higher Womersley number. This observation confirms once more the assumption made above, that the influence of the tidal volume on mass transport is lower than the influence of the Womersley number.

Probability distribution in each generation

For better quantification of the distribution of mass the average values of the probability at selected cross sections down to the 6th generation are given (Fig. 5.6 and 5.7). The influence of increasing Womersley number at constant Re is presented in Fig. 5.6. The results for increasing Re at constant α are shown in Fig. 5.7. Since the longitudinal distances of the cross sections from the carina vary strongly within the branches of one generation, these values are summarized in Tab. 5.2. In the nomenclature of the branches the letter G stands for "generation", the number denotes the generation. R and L denote the right and left branch of each bifurcation, respectively. The maximum difference between the longitudinal distances within one generation occurs at generation 5 with a difference of 26 mm between the cross sections.

Branch (nomenclature)	Generation	Longitudinal distance from the carina (mm)
G1L, G1R	1	13
G2LL, G2LR	2	40
G2RR, G2RL	2	64
G3LLL, G3LLR	3	54
G3RRR, G3RRL	3	76
G4LLLR, G4LLLL	4	60
G4RRRR, G4RRRL	4	82
G5LLLLL, G5LLLLR	5	75
G5RLLRL, G5RLLRR	5	101
G5RRRRR, G5RRRRL	5	91
G6LLLLLL, G6LLLLLR	6	89
G6RLLRLL, G6RLLRLR	6	114
G6RRRRR, G6RRRRL	6	105

Table 5.2: Longitudinal distances from the carina of selected cross sections.

Comparing the cases of different Womersley numbers, the probability in the cross section of the main branches (1st generation) is less symmetric for higher α. As already stated by Elad et al. [26], HFOV leads to enhanced asymmetry effects for asymmetric lung geometries. In the second and third generations, asymmetric probability distributions can be found for both Womersley numbers. From the 4th generation to more distal branches, the probability becomes more symmetric for the higher Womersley number. At $\alpha = 12.3$ the probability in all analyzed branches of the 4th generation is at about 6% whereas at $\alpha = 9.5$ the averaged cross sectional probability varies there between 5.6% and 12.7%. This asymmetry at $\alpha = 9.5$ could be explained by the different distances from the carina. For all branches distal to the left main branch the distance is about 22 mm less than the distance to the distal branches of the right main branch (see Tab. 5.2). For $\alpha = 12.3$, differences in flow partitioning due to the influence of asymmetric lengths and curvatures (i.e. different downstream pressure losses) have been decreased. Phase shift of flow between parallel branches occurs which leads to an exchange of mass, i.e. pendelluft. Consequently, high frequencies compensate the effects of asymmetric geometry and mass distribution in the lower branches. Additionally, higher frequencies increase the inlet pressure within the trachea and large differences in compliance become less important [6, 26]. In these references it is shown that despite large differences between the compliances at the distal ends of the lung model, high frequency leads to homogenization of flow partitioning.

Although a more homogeneous distribution was observed for a higher Womersley number, the probability in the central branches G5RLLRL, G5RLLRR and G6RLLRLL, G6RLLRLR is still higher (about twice as high) than in the lateral branches. As stated above, the overall probability in the medial branches (G2LR and G2RL) is much higher than in the lateral branches, even for higher Womersley numbers. This asymmetry could not be compensated by mass exchange between parallel branches. Pendelluft effects are therefore seemingly not important within the main branches, at least not for the Womersley numbers applied during our investigations and the model we used. Consequently, strong asymmetries occurring within the first and second generation might also propagate into the lower generations.

For increasing Reynolds number but constant Womersley number (Fig. 5.7), a significant change in probabilities could only be observed in the upper main branches (generation 1 and 2). As the probability decreases in the first generation, it increases in the medial branches of the second generation. In the lower generations the integral probabilities remain at the same level or even decrease (G6RLLRLL and G6RLLRLR). These obser-

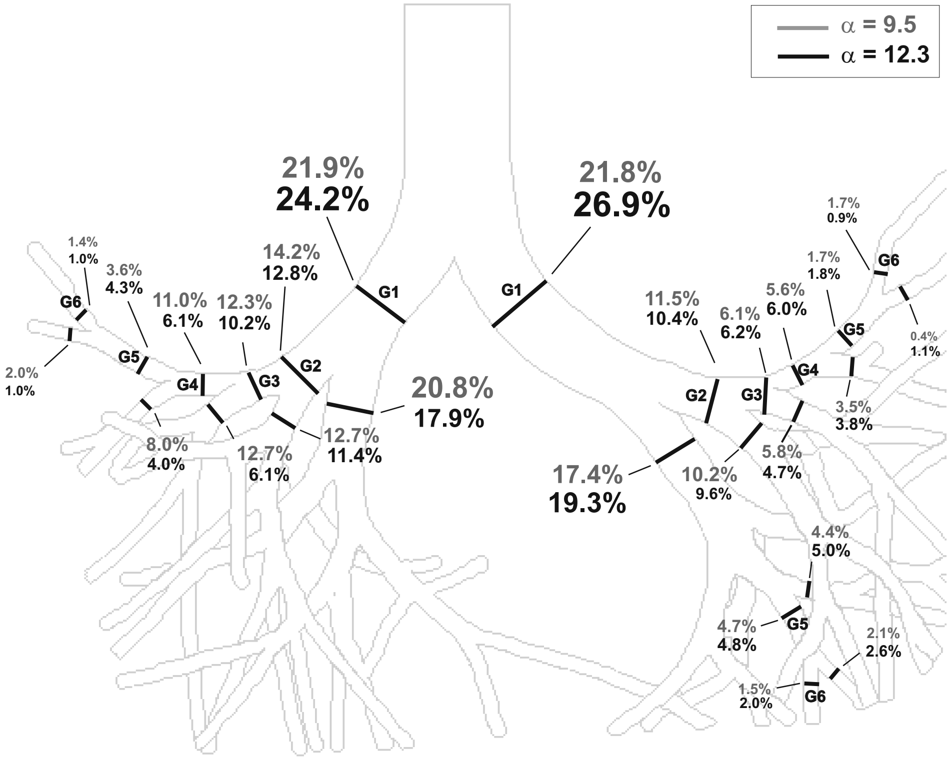

Figure 5.6: Average probability distribution at selected cross sections of each generation for different Womersley numbers at Re = 1980, higher probabilities are coded by larger font size.

vations suggest a faster axial streaming through the bifurcation tree at higher *Re*. For all cases presented in Fig. 5.6 and Fig. 5.7 the sum of the average probability of the daughter branches is always higher than the probability in the mother branch. This is due to the cyclic mass transport of particles. As they enter the model they reach only a certain penetration depth. In the subsequent inspiration cycle the penetration is slightly deeper into the lung but particles still return to the mother branch. Due to strong secondary motions within the lung bifurcations, particles never return to their original position. Hence, it happens that the same particle passes two different parallel branches within two subsequent inspiration phases leading in sum to higher probabilities in the daughter branches than in the mother branch. It needs to be mentioned that this effect can not be associated with pendelluft since it could be observed in branches without phase shifts as well.

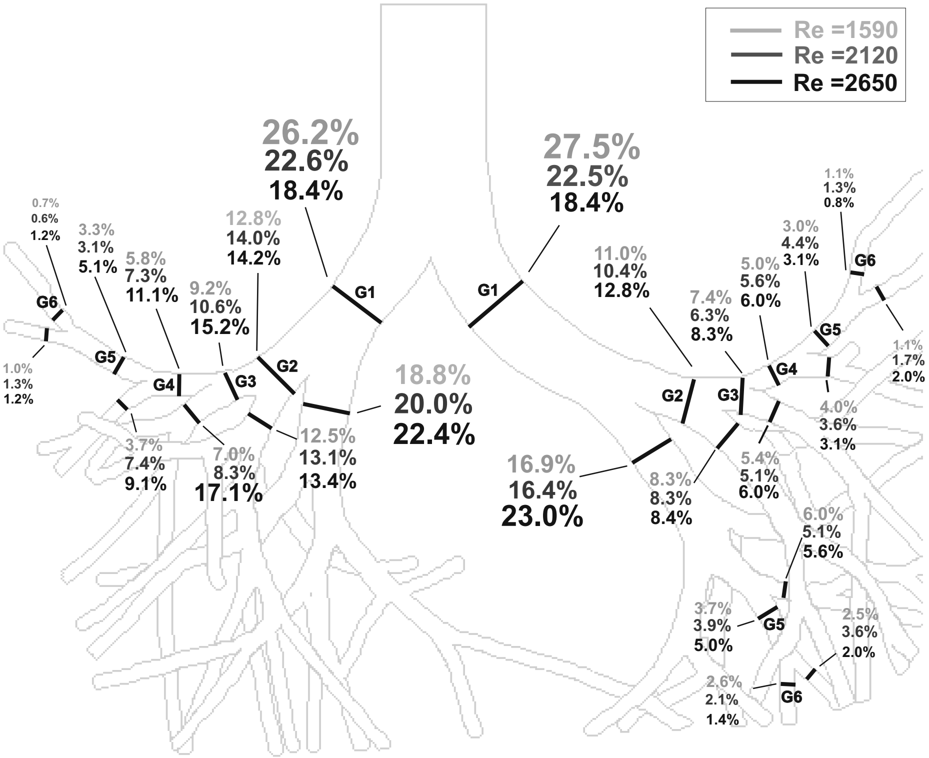

Figure 5.7: Probability distribution at selected cross sections of each generation for different Reynolds numbers at $\alpha = 11$, higher probabilities are coded by larger font size.

5.4 Conclusions

In this study flow partitioning in a branching network was visualized by particle advection under high frequency oscillatory ventilation (HFOV) conditions. This method allows to analyze the probability distribution of fluid elements passing certain branches in the lung network for a large number of cycles. The confirmation of results already stated by other researchers proves the suitability of this measurement technique to investigate the distribution of mass flow within human lung. The influence of different characteristic flow numbers could be shown independently.

The application of different Womersley numbers α at constant Reynolds number Re has shown that for increasing α (i.e. increasing frequency), a larger number of cycles is needed to transport mass in the lower generations. Note, that the tidal volume had to be decreased in order to keep the Reynolds number constant. Nevertheless, the total time for the particles to reach the lower branches remains the same for higher frequencies, thus the streaming velocity is comparable. Consequently, HFOV is not only assumed to be more protective [60] than conventional mechanical ventilation, but it is also characterized by the same efficiency. Increasing α at constant Re reveals that particles are more homogeneously distributed within the lower branches. Asymmetries observed at lower Womersley numbers in generations 4-6 may be compensated by enhanced secondary motion and pendelluft effects. However, it was also shown that strong asymmetries in flow partitioning within the upper branches (2nd generation) could not be compensated by mass exchange effects occurring at higher frequencies. This indicates that the influence of the lower generations does not propagate up to the generations 0 to 2. The impedances of the lower branches do seemingly not influence the transport of mass within the main branches.

An interesting fact is that the tidal volume (TV) plays only a minor role. Even a decrease of the TV leads to the same transport efficiency at increasing Womersley number.

6 Role of ventilation frequency in airway reopening

6.1 Introduction

For conventional mechanical ventilation the time constants of different lung regions are only of minor relevance due to the relatively long inspiration and expiration times. However, during HFOV, inspiration duration is shortened significantly and subsequently the distribution of air increasingly depends on the pulmonary characteristics, too. Furthermore, a variation of ventilation frequency during HFOV is associated with a shift of ventilation distribution (see section 5.3). Hence, frequency-dependent ventilation could be used to selectively recruit atelectatic lung areas.

The present study focuses on the role of HFOV in airway reopening. A simplified model represents a highly inhomogeneous lung region consisting of a collapsed and an open airway branch next to each other in a single bifurcation. The phenomena found with the simplified model will be verified for a more realistic, three-dimensional model of the human lung including the first 6 airway generations. Using these models we have studied the inflation dynamics of lungs with inhomogeneous lung parts characterized by collapsed regions adjacent to healthy and open lung areas.

6.2 Material and methods

6.2.1 In-vitro lung model

The in-vitro investigations were carried out at two different models of the airway network. For further reference, these models will be indicated by the index “M”, the original lung is indicated by “O”. The first model is a rigid transparent tube model with a single bifurcation consisting of the trachea and main branches in the same scale as a human adult lung. It is used to quantitatively analyze the airway reopening mechanisms (see Fig.6.1a) and b)). For comparison of the results in the single bifurcation to a more realistic representation of the bronchial tree, a second model was used which covers the upper airways down to the 6th generation (Fig. 6.1c)). The geometry of the trachea and first generation is identical to the single bifurcation model. The geometry and manufacturing of the 6-generation model is identical to the previous studies and has been described in section 3.2.1. The single bifurcation model includes a collapsed airway passage which is represented by a thin $45 \mu m$ natural rubber latex membrane (Ansell, Austria) which closes one exit of the bifurcation branches (left branch in Fig.6.1 a) and b)). The other branch was left open to the ambient representing the impedance of a free flow pathway further down into the lung. The aim of the study was to demonstrate the opening mechanisms of the membrane as function of different ventilatory frequencies. This model thereby characterizes a lung region with a large difference in the time constants and inhomogeneous compliance. In the same way as in the single bifurcation model, all distal ends of the left main branch in the 6 generation model were closed again by thin rubber membranes (see Fig.6.1c)), representing a collapsed lung lobe.

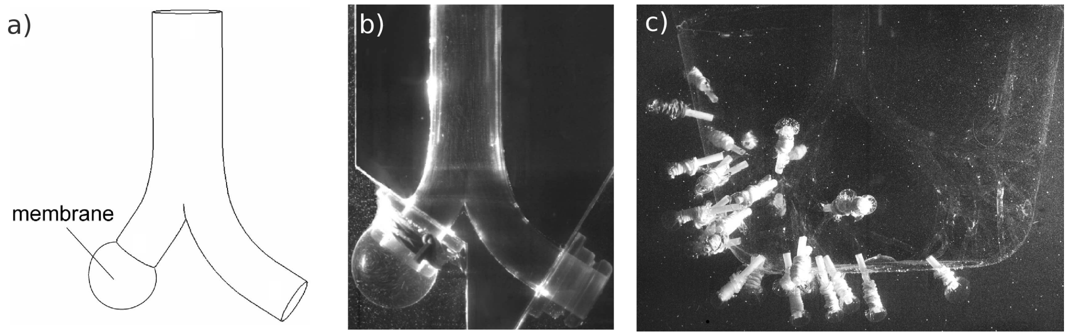

Figure 6.1: Geometry of the single bifurcation model, original model computer designed (a), Plexiglas model with membrane at one branch at the inflated state(b),6-generation silicone model with membranes at the distal ends of the left main branch (c).

Besides the Womersley, Reynolds and Dean numbers which were introduced in the studies above, a fourth important characteristic number contributes to this problem. It characterizes the opening pressure Δp of the membrane relative to the dynamic pressure in the flow. This characteristic number is equivalent to the so called Euler-number

$$Eu = \frac{\Delta p_{opening}}{\varrho/2 \cdot U^2}. \tag{6.1}$$

The variable ϱ denotes the fluid density. For the same non-dimensional opening pressure of the simplified membrane model and a collapsed lung regime, a comparable physical behavior is ensured for the reopening and initial phase of filling. From this condition the appropriate membrane stiffness for the liquid model can be determined. Therefore, the opening pressure Δp in equation 6.1 is replaced by $\Delta V/C$, where ΔV is the tidal volume and C denotes the compliance of the membrane. Given that $U = 2 \cdot \pi \cdot f \cdot h \approx f \cdot \Delta V/D^2$ (h = piston amplitude) leads to the following expression for the Euler number

$$Eu = \frac{\Delta V/C}{\varrho/2 \cdot (f \cdot \Delta V/D^2)^2} \approx \frac{D^8}{\varrho \cdot C \cdot \nu^2 \cdot \Delta V} \cdot \frac{1}{\alpha^4}. \tag{6.2}$$

If one additionally replaces the frequency f in equation 6.2 by the Womersley number α from equation 2.1 one ends up with a ratio of the model and the original compliances:

$$\Rightarrow \frac{C_M}{C_O} = \left(\frac{\Delta V_M}{\Delta V_O}\right)^{-1} \cdot \left(\frac{\varrho_M}{\varrho_O}\right)^{-1} \cdot \left(\frac{\nu_M}{\nu_O}\right)^{-2} \cdot \left(\frac{D_M}{D_O}\right)^{8}. \qquad (6.3)$$

With a density ratio of $\varrho_M/\varrho_O = 960(\varrho_{liquid} = 1150\,\mathrm{kg/m^3}, \varrho_{air} = 1.2\,\mathrm{kg/m^3})$, a kinematic viscosity ratio of $\nu_M/\nu_O = 0.54$ ($\nu_{liquid} = 8.4{\cdot}10^{-6}\,\mathrm{m^2s^{-1}}, \nu_{air} = 15.6{\cdot}10^{-6}\,\mathrm{m^2s^{-1}}$), a scaling factor of $D_M/D_O = 1$ and therefore $\Delta V_M/\Delta V_O = 1$ it is obtained that the compliance of the membrane needs to be a factor of 1/280 smaller than the values representative for typical atelectatic lungs in order to simulate a realistic airway reopening and recruitment behavior in our liquid model.

For a healthy adult lung a typical value of the compliance is in the range of $100 - 150\,\mathrm{ml/cmH_2O}$. For an atelectatic lung these values are reduced by 1/10 down to $10 - 15\,\mathrm{ml/cmH_2O}$ [87]. Therefore, the compliance of the membrane should be in the range between 0.036 and $0.054\,\mathrm{ml/cmH_2O}$.

6.2.2 Pressure-volume relationship of the membrane

The pressure-volume (p-v) curves of the membranes were measured by using a syringe which displaces a specific volume of fluid into the branch to inflate the membrane into a balloon shape and by measuring the static pressure simultaneously with a pressure sensor (Kistler, type 4043A2).

As shown in Fig.6.2, the p-v curve (solid line) is characterized by a small slope in volume in the initial inflation phase (bulged membrane, see A,B) until the pressure reaches a critical value (B). Beyond, the membrane expands to the shape of an inflated balloon with a corresponding volume increase until it reaches a new equilibrium position at a lower pressure. This represents a negative stiffness behavior as a result of the different states of the membrane shape changing from a bulged membrane (B) via a jump-like transformation to an inflated balloon like shape (D). Therefore, the model features a similar, non-linear pressure-volume (p-v) behavior during inflation as measured by Suki et al. [100] and Alencar et al. [2] for the collapsed lung in the process of being inflated, i.e., a steep increase of pressure up to the opening pressure and thereafter a relaxation and ongoing filling of the recruited area which they called a phase of “negative elastance”. The pressure peak at which the membrane expands to its shape of a balloon is defined as

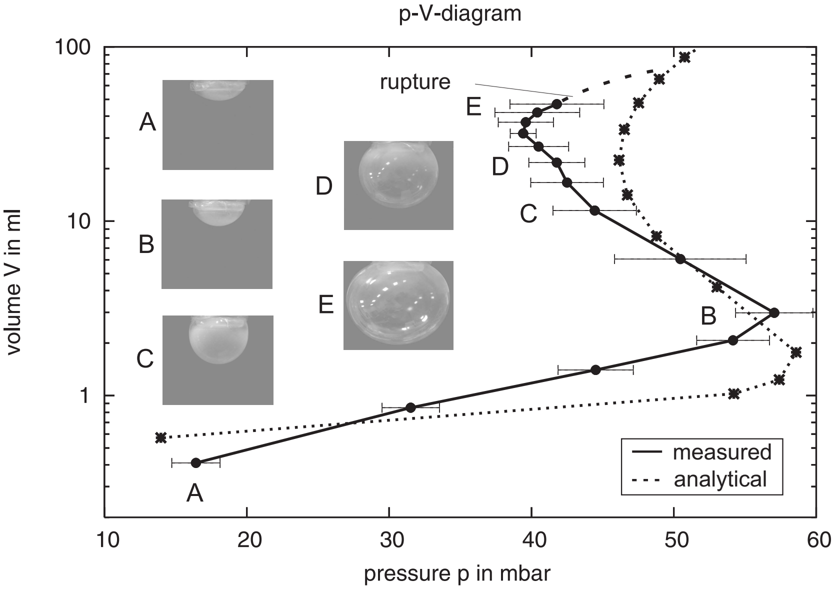

Figure 6.2: Pressure-volume characteristic curve of a silicone rubber membrane (solid line), analytically calculated pressure-volume characteristic (dashed line); the volume represents the amount of fluid displaced by the membrane from the initial plane stretched state.

the "opening pressure". Based on the measured p-v curve the corresponding compliance C_M of the membrane was determined from a linear curve fit in the range AB (see equation 6.4),

$$C_M = \frac{\Delta}{V_{opening}} \Delta p_{opening} = \frac{2.8\,\mathrm{ml}}{57\,\mathrm{cm}_{\mathrm{H_2O}}} = 0.05\,\mathrm{ml/cm}_{\mathrm{H_2O}}. \tag{6.4}$$

This value for the compliance corresponds to the physiological compliance C_O of atelectatic lung areas with the scaling factor of equation 6.3.

For validation of the experimentally determined pressure-volume relation, the results are compared to the analytical solution for a rubber balloon [79]:

$$\Delta p = 2 \cdot G \cdot \frac{d_0}{r_0} \cdot \left[\left(\frac{r}{r_0} \right)^{-1} - \left(\frac{r}{r_0} \right)^{-7} \right] \cdot \left[1 + \frac{\beta}{G} \cdot \left(\frac{r}{r_0} \right)^{2} \right]. \tag{6.5}$$

In equation 6.5 G denotes the shear modulus, d_0 and r_0 denote the material thickness and equivalent balloon radius before distension, β/G is a constant for rubber balloons. These variables were set as follows according to the manufacturer:

$$G = 4.5 \cdot 10^5\,\mathrm{Pa} \qquad d_0 = 0.045\,\mathrm{mm} \qquad r_0 = 5\,\mathrm{mm} \qquad \beta/G = 0.08$$

The analytically calculated pressure-volume characteristic is additionally plotted in Fig. 6.2 (dashed line). It can be seen that the trend is similar to the experiments. Deviations between experimental and analytical results can be explained by different initial conditions as the analytical calculation assumes a spherical balloon shape. Additionally, small material inhomogeneities might alter the results.

6.2.3 Measurement methods

For the analysis of the inflation dynamics, the opening stages of the membrane as function of time and frequency were recorded by a high speed camera (Photron APX RS). Moreover, the method of Particle Image Velocimetry (PIV) was applied in order to analyze the flow structures within the in-vitro models. For this method, small tracer particles ($d = 22\,\mu$m) were added to the flow. Their displacement within a defined time delay is a measure for the local flow velocity. In order to illuminate a specific plane in the lung models, a light sheet was generated by a high speed laser (Pegasus, NEW WAVE). Images were recorded again by the high speed camera.

6.3 Results

The net influx into the collapsed branch is measured by the displaced volume of the membrane during a complete breathing cycle in the period T for different non-dimensional ventilation frequencies α (see Fig. 6.3a). The net influx is shown in relation to the total tidal volume. Even if one end of the bifurcation is "open" the membrane at the opposite branch starts to expand with increasing frequencies. At a critical Womersley number of $\alpha = 10$ the membrane suddenly expands to form a balloon. The large increase in volume indicates that the critical opening pressure of about 55 mbar (Fig. 6.2) must have been reached. About 14% of the preset tidal volume entered the balloon. Further increase of the frequency enhances the net mass flow into the reopened branch.

Fig.6.3b) compares the net flux results to the 6 generation model. As can be seen, the opening behavior of the membranes and the net flux into the collapsed part in the 6 generation model are similar to the single bifurcation model. The dashed curve in Fig.6.3a) and b) indicates that with increasing Womersley number the instant of maximum extension is shifted in time towards the end of the inspiration phase. Actually, the inflation phase of the balloon continues although the pressure is starting to fall, which can be attributed to the non-linear behavior of the membrane and inertial effects. The shape of the mem-

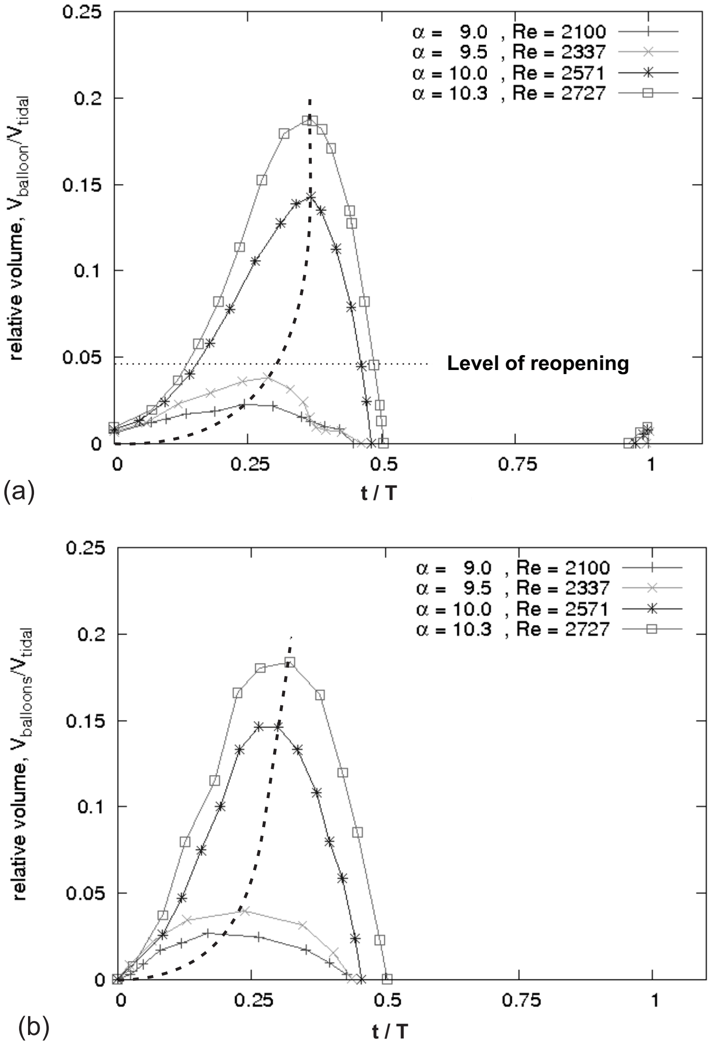

Figure 6.3: Relative balloon volume for different Womersley numbers as function of the non-dimensional cycle time, t/T denotes the time t related to the cycle time T; the level of reopening represents the instant at which the membrane expands to the shape of a balloon. The dashed line marks the point of maximum filling of the membrane; (a) inflated relative volume of the single bifurcation, (b) relative volume of the inflated balloons of the 6 generation model.

brane at selected stages during inflation is shown in Fig.6.4. Since the model including the membrane is transparent, the mass and momentum flux into the reopened membrane was visualized here using long time exposures of the tracer particles. The formation of a vortex ring serves as an indicator for the fluid momentum entering the reopened branch by means of its size and circulation.

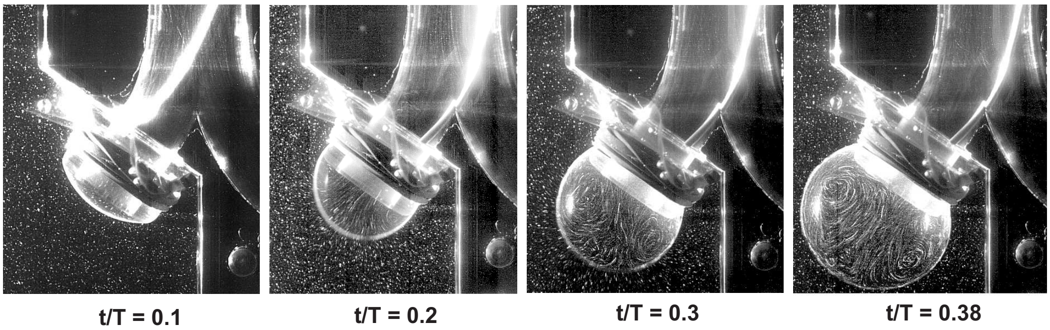

Figure 6.4: Opening stages of the membranes at different times during the inspiration at $\alpha = 10.3$.

6.3.1 Particle Image Velocimetry (PIV) - Measurements

For additional comparison of both models, PIV-measurements were performed in the center plane section of the trachea and the first daughter branches (see Fig. 6.5).

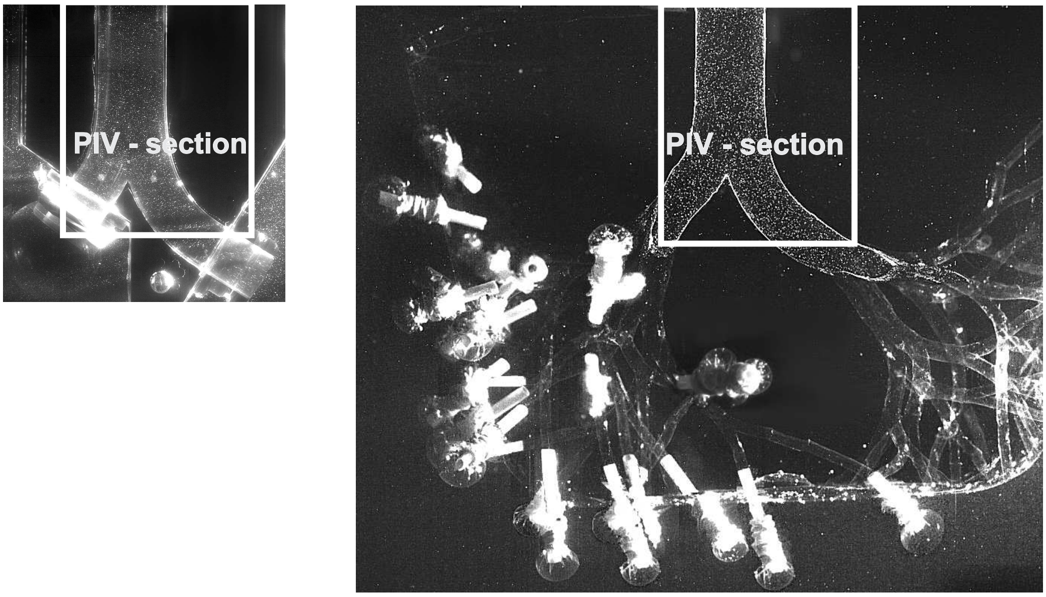

Figure 6.5: Selected sections of the lung models for PIV-investigations, a) single bifurcation model, b) 6-generation model.

The results are summarized in Fig. 6.6a) and b) showing the velocity vectors and velocity magnitude color coded for the instant of maximum inspiration for two different Womersley numbers, $\alpha = 6.7$ (Fig. 6.6a) and $\alpha = 10.3$ (Fig. 6.6b). For low Womersley numbers ($\alpha = 6.7$) no influx into the left branch could be observed for both lung models, whereas at $\alpha = 10.3$ a considerable amount of mass enters the left branch. The velocity profiles for the single bifurcation and 6 generation model are similar for $\alpha = 10.3$, too. The PIV results demonstrate that despite the simplicity of the single bifurcation model, the velocity profiles and membrane opening behavior are similar to the three-dimensional 6-generation model. This allows to conclude that flow partitioning in highly inhomogeneous lungs is mainly determined by the different compliances whilst the inhomogeneity of the tree network branching structure plays only a minor role.

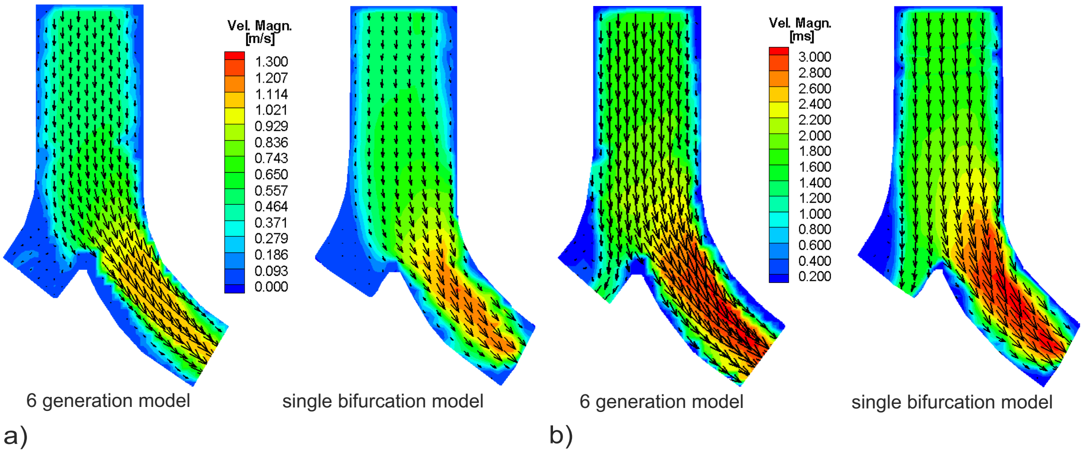

Figure 6.6: Results of the PIV-measurements, shown are velocity vectors and color-coded the velocity magnitude for two different Womersley numbers α and lung models at the instant of maximum inspiration, (a) $\alpha = 6.7, Re = 1169 (f_{air} = 1.4Hz, TV = 60ml)$, (b) $\alpha = 10.3, Re = 2727 (f_{air} = 3.3Hz, TV = 60ml)$.

6.4 Conclusion

The present study shows that ventilatory frequency has an important impact on airway reopening. According to the presented data, relatively stiff membranes at the distal ends of lung models, comparable to collapsed lung airways, are recruited successfully at higher frequencies (Womersley numbers). The higher frequencies of the flow induce higher velocities (the tidal volume was kept constant) and in consequence an increase of the viscous pressure loss of the flow in the free pathways of the lung. Consequently, the mean upper airway pressure will increase, whilst the balloon pressure in the lower “healthy units” remains unchanged. If this pressure increase in the upper airways exceeds the opening pressure of “low compliance” units, these regions will open up, inflate and their volume increase improves their compliance. Consequently, a successful recruitment largely depends on how far down in the bronchial tree the collapse is located. If upper regions of the lung are collapsed, it is easier to recruit these areas since the pressure loss in the remaining free airway pathways is larger. When the critical opening pressure of the membrane in the model is reached, the successive inflow becomes largely controlled by the non-linear pressure-volume characteristics of the membrane.

As the dashed line in Fig. 6.3a) and b) demonstrates, there is a phase shift of the maximum filling towards the end of the inspiration phase with increasing frequency. This behavior represents the "negative elastance" of the lung observed by Alencar et al. [2]. It can be explained by the change of the characteristic timescale $\tau = C \cdot R = \Delta V/\dot{V}$ before and after reopening. Up to the opening pressure, the time-scale of the atelectatic region is short due to both a low compliance and a low amount of displaced fluid. This changes dramatically after successful reopening where the time-scale largely increases due to the steep increase of the compliance and resistance. Consequently, the maximum filling occurs later in the inspiration cycle. Note also, that much larger time-scales can co-exist due to the interaction of branches in multiple flow networks as shown by Bruecker and Riethmuller [10]. These time-scales result from resonant interaction of flow separation in successively bifurcating branches. In addition, due to the increasing phase shift of the core flow relative to the oscillating pressure gradient with increasing frequency (annular-effect [105]), fluid regions of low inertia respond earlier to the change of the pressure gradient than flow regions with high inertia. This contributes to a further delay of the maximum filling state to the end of the inspiration cycle. Thus, both effects support the importance of the end-inspiratory pressure to keep the lung open.

7 Airway obstruction by liquid bridges

7.1 Introduction

The human lung airways are typically coated by a thin viscous liquid film called mucus. During diseases such as asthma or bronchitis mucus production is increased and can even obstruct the human airways [15, 55]. Especially in the case of neonates, a deficiency of surfactant often leads to airway closure due to higher surface tensions [42]. In more compliant lungs, higher surface tension can lead to a “compliant collapse” at which the airway walls are buckled/deformed [39].

In both cases the airways have to be recruited by mechanical ventilation which can again damage the lung tissue when conventional mechanical ventilation is applied [22,35]. Therefore, HFOV is frequently used as it might lead to less overdistension in the lungs at still sufficient gas exchange [60]. The airway reopening often takes place spontaneously as the liquid column breaks up into droplets. This effect is known as Rayleigh instability [42]. In reference [42] it was shown that, if frequency and amplitude are sufficiently large, airway closure does not occur.

In the case presented here, the oscillatory flow in a rigid tube with liquid-air interface representing an airway occlusion is investigated. The liquid break up conditions for varying frequencies and amplitudes are analyzed. The flow at the interface is furthermore investigated since it is characterized by steady streaming. This mean flow is induced by tangential stress at an interface or boundary layer [41, 62, 81]. The steady streaming patterns are analyzed by means of PIV-measurements and visualized directly by superposition of subsequent images. The conclusions about steady streaming in this simple geometry could be used to assign them to the streaming behavior in the lung bifurcations. The influences on steady streaming in the human lung are not fully understood, yet. The qualitative streaming patterns in a single bifurcation were suggested by Haselton and Scherer [43], based on the spreading of a liquid bolus in the bifurcation and theoretical assumptions. The velocity vector patterns of steady streaming in the human lung have never been visualized.

7.2 Experimental model

Oscillatory flow is investigated in a vertically oriented tube of 500 mm length with an open end at the top at ambient pressure (Fig. 7.1). Up to the height of $y = 400\,\mathrm{mm}$ the pipe is filled with oil (density $\rho = 840\,\mathrm{kg/m^3}$, kinematic viscosity $\nu = 31 \cdot 10^{-6}\,\mathrm{m^2/s}$, surface tension $\sigma = 23\,\mathrm{mN/m}$). The pipe diameter is $D = 12\,\mathrm{mm}$. At the bottom entrance a piston connected to a magnetically driven shaker (VEB Messelektronik Otto Schön, GDR) generates the vertical oscillation of fluid in the pipe.

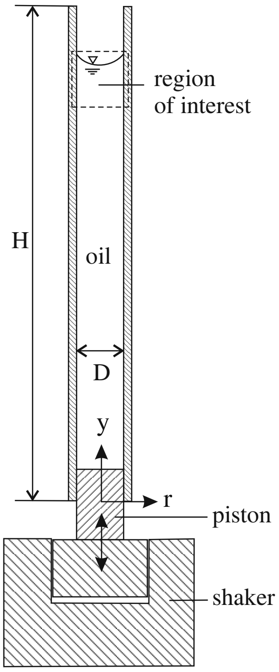

Figure 7.1: Experimental set-up (lengths ratios are not in true scale).

For application of the results on the human lung airway closure, characteristic flow parameters have to be considered. In the lung, airway occlusion usually occurs in the lower airways where gravitational effects do not play a role and the flow is dominated by capillary effects. As the wavelength decreases, gravitational waves become capillary waves. Below the wavelength of $\lambda_{min} = 2\pi\sqrt{\sigma/\rho g}$ capillary effects dominate. With the values given above, the critical wavelength is $\lambda_{min} = 10.5\,\mathrm{mm}$. Since the pipe diameter is 12 mm, the maximum wavelength occurring in the tube is expected to be below the value of λ_{min}. Hence, gravitational effects can be neglected in this case. Furthermore, an important characteristic number is the Capillary number Ca, which denotes the relation of viscous forces to surface tension.

$$Ca = \frac{\nu\rho u}{\sigma}. \tag{7.1}$$

Here, u denotes the characteristic flow velocity. When $Ca \gg 1$ the flow is dominated by viscous forces [39]. Here, the maximum Capillary number is $Ca = 0.2$ based on the maximum flow velocity. Hence, surface tension dominated effects can be assumed near the interface.

For free surface flow, the Weber number, denoting the relation of fluid's inertia to surface tension with

$$We = \frac{\rho u^2 l}{\sigma}, \tag{7.2}$$

is furthermore important. For the variable l, the oscillatory amplitude is set here as the characteristic length. Since oscillatory flow is investigated, the Womersley number α is used here again. The flow investigations were performed for different oscillatory amplitudes and frequencies.

All relevant flow parameters, used for the experimental analysis of the interface flow, are given in Tab. 7.1. The Reynolds number was not used here, since the flow is dominated by surface tension effects and not viscous forces. Additionally, the Reynolds number is also based on the flow velocity which is already considered by the Weber number.

Case No.	Frequency (Hz)	Amplitude (mm)	Womersley number α	Weber number We
1	10	0.5	8.5	0.018
2	10	0.7	8.5	0.049
3	10	1.0	8.5	0.14
4	10	1.25	8.5	0.28
5	10	1.5	8.5	0.49
6	10	1.75	8.5	0.77
8	15	0.5	10.5	0.041
9	15	0.7	10.5	0.11
10	20	0.63	12.1	0.14
11	25	0.5	13.5	0.11
12	30	0.5	14.8	0.16

Table 7.1: Experimental settings and values of the characteristic flow numbers at the interface of oscillatory tube flow.

For these parameters steady streaming flow at the interface was investigated in detail. For flow characterization PIV (Particle image Velocimetry) measurements have been carried out. Therefore tracer particles (Fillite, hollow spheres) with a mean diameter of $20\,\mu$m were added to the liquid and the center plane of the pipe was illuminated by a 10mJ Nd:YAG high speed laser (Pegasus, NewWave) with a wavelength of 532 nm. Images were recorded using a high speed camera (Photron, Fastcam PCI 1024). In order to visualize the steady streaming, phase locked images were taken. Therefore, a trigger signal was received from an accelerometer (KD 35, Metra Meß- und Frequenztechnik, Germany) connected to the oscillating element of the shaker. Hence, the image cross correlation was made between two subsequent periods at the same phase angle. The value of the phase angle is not important since steady streaming does not depend on the phase angle. For all settings 100 images were taken and averaged in order to receive statistically firm results.

For the analysis of liquid break up, the maximum amplitudes and frequencies before the free surface becomes instable were measured.

7.3 Results

7.3.1 Instability at the interface

In this section the conditions for capillary instabilities at the air-liquid interface are discussed in relation to possible break-up of the liquid bridges into smaller droplets within the lung.

The stability of the interface is influenced by pressure perturbations due to time-dependent fluid acceleration and capillary forces due to fluid-wall relative motion [51]. Under HFOV such conditions are forced onto the liquid brigdes either by oscillatory pressure or wall motion. The resulting inferface oscillations can be described by the Mathieu equation [51, 104]. At excitation frequencies close to the natural frequency of the free surface wave the surface becomes unstable and breaks up forming smaller droplets. The natural frequency can be calculated according to [93]

$$\omega_{mn}^2 = gk_{mn}\left(1 + \frac{k_{mn}^2\sigma}{g\rho}\right)\tanh(k_{mn}h). \tag{7.3}$$

Here, g denotes the gravity, h is the liquid depth and k_{mn} is the wave number and the nth positive zero of the following equation [44]:

$$\left.\frac{dJ_m(k_{mn}r)}{dr}\right|_{r=R} = 0. \tag{7.4}$$

$J_m(k_{mn}r)$ is a Bessel function of the mth order. The zeros of equation 7.4 give the axisymmetric and asymmetric modes, respectively. The values calculated from equation 7.3 are valid only for the inviscid case. In order to incorporate damping by viscosity the parameter δ, denoting the ratio of actual to critical damping, is introduced according to [44] . The natural frequencies are shifted to lower values due to the influence of viscosity. A new, viscous-shifted frequency $\hat{\omega}_{mn}$ can be calculated according to

$$\hat{\omega}_{mn} = \omega_{mn}(1 - \delta). \tag{7.5}$$

The forcing amplitude A_0 at which instability occurs is [44]

$$A_0 = [k_1 \tanh(k_1 h)]^{-1} \left[\delta^2 + \frac{(\omega^2 - \hat{\omega}_1^2)^2}{(2\omega^2)^2}\right]^{\frac{1}{2}}. \tag{7.6}$$

In equation 7.6, ω is the excitation angular frequency, k_1 and $\hat{\omega}_1$ are the wave number and viscous natural frequency of the $n = 1$ mode, respectively.

Fig. 7.2 exemplarily shows the stability chart for the harmonic mode k_{01} with and without damping, i.e. for the inviscid case and the viscosity of the liquid used during our experiments. Furthermore, a stability curve for a cylinder of smaller radius ($R = 1\,\mathrm{mm}$) is added. As shown in Fig. 7.2, in case of no damping (dash-dotted curve), i.e. viscosity is reduced to zero, the natural frequency is slightly shifted to higher values. However, the excitation amplitude to induce instability decreases to zero. Hence, the lower the viscosity of the obstructing liquid, the better recruitment can be realized. If the tube diameter is

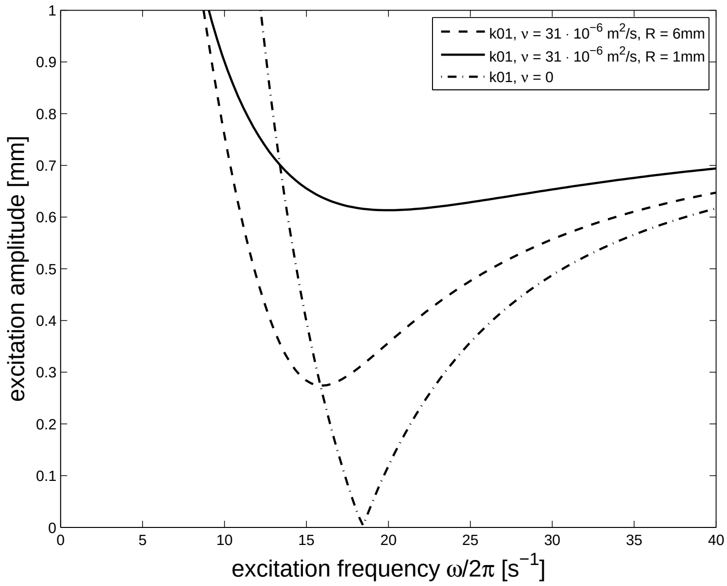

Figure 7.2: Instability chart for the harmonic mode k_{01} for the conditions applied in the experiment (dashed line), smaller pipe radius (solid line), viscous free case (dash-dotted line).

decreased (Fig. 7.2), solid curve), higher excitation amplitudes are necessary to induce instability. That means, if liquid bridges occur in the smaller airways, larger amplitudes are necessary for succesful recruitment. However, as mentioned above, higher amplitudes are coupled with higher tidal volumes which can induce additional lung injury. In order to avoid that, higher frequencies at lower tidal volumes are applied (HFOV).

In Fig. 7.3 the analytical results for several modes (symmetric and asymmetric) are presented. For frequencies below 10 Hz, instability occurs only at very high amplitudes. As the frequency increases, a minimum amplitude of about 0.2 mm at 30 Hz is necessary to induce a harmonic instability. As the amplitude further increases, single modes can not be separated anymore. A superposition of harmonic and subharmonic oscillations will rather occur. The points, at which instability of the free surface could be observed experimentally, were included for distinct frequencies in Fig. 7.3 (single circles). Below a frequency of 20 Hz instability could not be observed in the experiments, since the maximum excitation amplitude realizable with the shaker was 1.75 mm, only. It is assumed, that instability occurs only at even higher amplitudes for $f \leqslant 15$ Hz. The experimental values of the corresponding frequencies and amplitudes, at which instabilities were induced, are summarized in Tab. 7.2. The free surface behavior for beginning instabilities at frequencies from 20 Hz to 40 Hz is shown in Fig. 7.4.

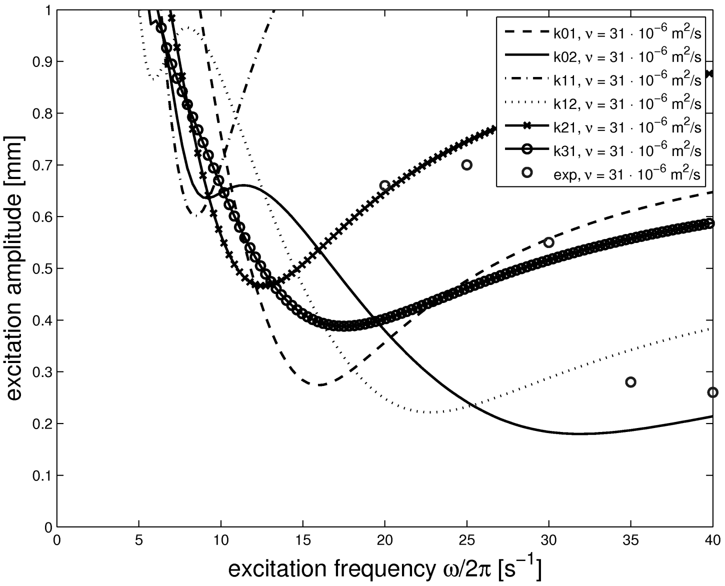

Figure 7.3: Instability chart for several modes of k, experimental data added by single circles.

Frequency (Hz)	Amplitude (mm)
20	0.66
25	0.7
30	0.55
35	0.28
40	0.25

Table 7.2: Frequencies and amplitudes at which free surface instabilities start to occur.

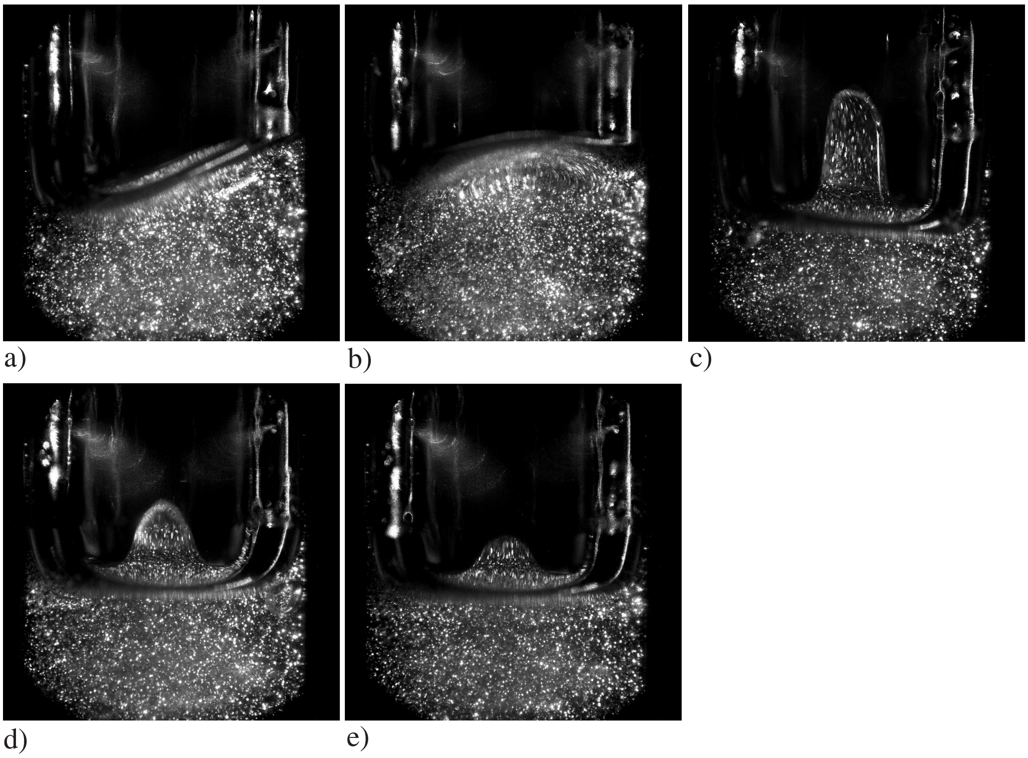

Figure 7.4: Visualization of the free surface contour for varying frequencies of the piston at which harmonic and subharmonic instabilities occur, a) 20 Hz, $A_0 = 0.66\,\mathrm{mm}$, b) 25 Hz, $A_0 = 0.7\,\mathrm{mm}$, c) 30 Hz, $A_0 = 0.55\,\mathrm{mm}$, d) 35 Hz, $A_0 = 0.28\,\mathrm{mm}$, e) 40 Hz, $A_0 = 0.25\,\mathrm{mm}$.

For 20 Hz and 25 Hz (Fig. 7.4 a) and b)) strongly asymmetric surface contours can be seen. It was further observed that these shapes oscillate with half of the excitation frequency which clearly indicates subharmonic behavior. Furthermore, as can be confirmed by the stability chart in Fig. 7.2b), several harmonic and subharmonic modes are superposed, while the subharmonics dominate. The observed instability at 30 Hz ((Fig. 7.4 c)) suggests harmonic behavior which can also be confirmed by the instability chart (Fig. 7.2b)). Here, the value of 30 Hz is on the curve of the first harmonic mode (dashed line). At 35 and

40 Hz (Fig. 7.4 d) and e)) the amplitudes to induce instability are strongly decreased and obviously, only the second harmonic mode (compare Fig. 7.2b) is existing.

7.3.2 Steady streaming motion near the stable interface

The mean motion of the fluid beneath the free surface is furthermore investigated. Fig. 7.5a) exemplarily illustrates the results of steady streaming flow by velocity vectors beneath the free surface at a frequency of 10 Hz and amplitude of 1 mm. The velocity vector lengths indicate regions of higher and lower streaming velocity amplitudes whereat the maximum streaming velocity occurs in the tube center.

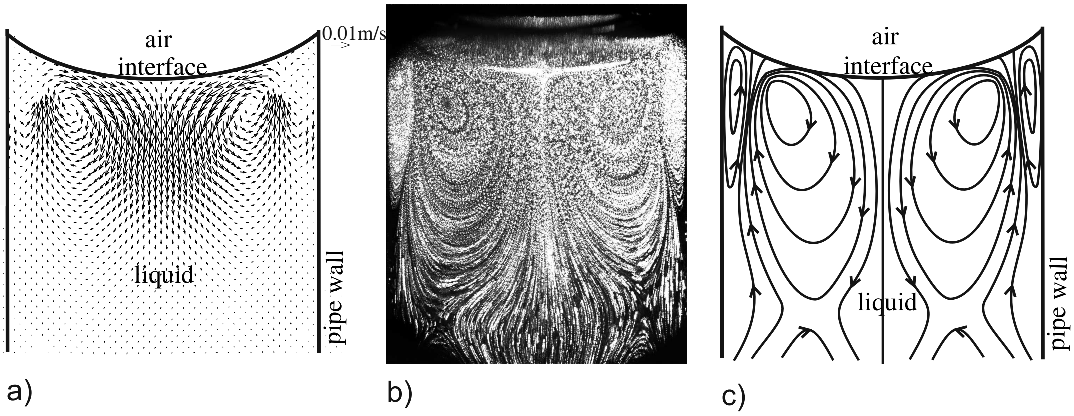

Figure 7.5: Velocity vectors below the free surface for $f = 10\,\mathrm{Hz}$ and $s_{max} = 1.00\,\mathrm{mm}$, a) averaged result of the steady mean flow, b) superposition of particle images for 35 subsequent periods, c) typical vortex pattern (schematically).

It can be seen that vortical structures have been generated consisting of a toroidal vortex in the tube center if considered as axisymmetric flow and a smaller outer vortex ring near the wall with opposite rotation to the larger vortex. The streaming velocity is more than one order of magnitude smaller than the maximum piston velocity. Both vortices are stretched in vertical direction, while the smaller vortex is further stretched in length up to three times of its diameter. The existence of the vortices suggests the existence of a double boundary layer as described by Gaver and Grotberg [38] for a tapered channel.

A good qualitative visualization of the vortex flows provides the superposition of subsequent particle images shown for 35 periods in Fig. 7.5b). It can be seen that the streaming flow extension is about one diameter into the pipe. Below, the influence of the free surface has vanished and the analytical solution for oscillatory pipe flow (see e.g. [105]) can be applied. The typical vortex pattern is shown schematically in Fig. 7.5c). It can be assumed that qualitatively, this streaming pattern can be found for all bounded oscillatory flows, i.e. in liquid bridges (see e.g. [81]) or near an end wall [41].

Variation of the Weber number We

In the following the variations of streaming patterns and velocity are analyzed for different variations of the characteristic parameters. The streaming patterns at constant Womersley number of $\alpha = 8.5$ and increasing Weber numbers (see Tab. 7.1), i.e. increasing oscillatory amplitude, are visualized in Fig. 7.6 by particle path lines. The formation of two counter rotating vortices can be identified very well in this illustration.

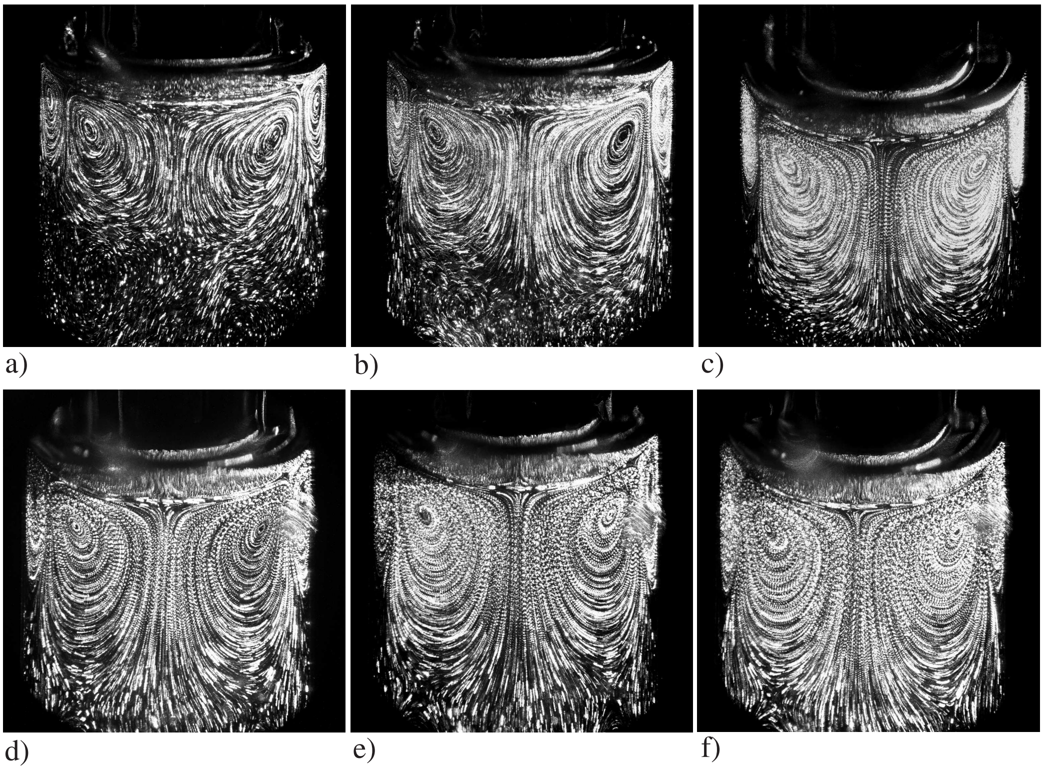

Figure 7.6: Superposed particle images for 35 subsequent periods at $\alpha = 8.5$, a) $We = 0.018$, b) $We = 0.049$, c) $We = 0.14$, d) $We = 0.28$, e) $We = 0.49$, f) $We = 0.77$.

In general, unbounded oscillatory pipe flows with constant Womersley number are characterized by an identical velocity profile in axial direction and therefore the same stokes layer thickness [105]. The path lines of the particles suggest only small changes of the characteristic streaming patterns. Increasing amplitudes lead to an increase of streaming penetration depth into the tube. For small amplitudes ($A_{max} = 0.5\,\mathrm{mm}$, Fig. 7.6a)) the axial extension of the vortices is only about $0.5D$ below the free surface. As the amplitude increases up to $A_{max} = 1.75\,\text{mm}$ (Fig. 7.6f)) the axial extension of the inner vortex has almost doubled. The axial extension of the outer vortex, however, remained constant.

In order to quantify the streaming velocity, the profiles of the axial velocity component at the axial position of the maximum streaming velocity are shown in Fig. 7.7. Here, bidirectional streaming can be observed, with the maximum streaming velocity in the pipe centre directed to the bottom entrance (negative y-direction). The shape of the velocity profiles is similar for all amplitudes. However, it can be seen that for increasing Weber numbers the streaming velocity in the pipe center has strongly increased. A doubling of the Weber number leads approximately to a three times larger value of the axial streaming velocity in the pipe center. Nevertheless, the overall streaming velocity is very low with a maximum of 8% of the maximum oscillatory velocity (piston velocity). The maximum streaming velocity was observed at a dimensionless axial distance of $y/D = 0.3$ from the interface.

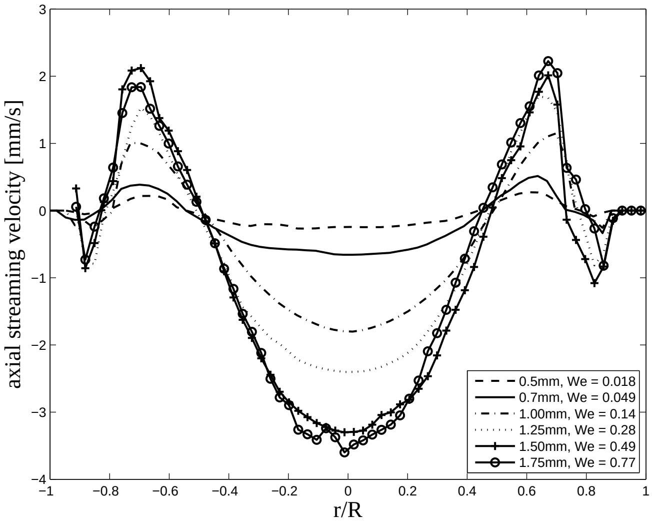

Figure 7.7: Axial velocity profiles at the location of the maximum streaming velocity at $\alpha = 8.5$ for different amplitudes.

Variation of the Womersley number α

As the results for constant Womersley number have shown (Fig. 7.7), the streaming velocity increases at higher Weber numbers. Hence, for the subsequent measurements, the Weber number was kept constant at $We = 0.14$ and the Womersley number was changed from $\alpha = 8.5$ to $\alpha = 17$. Note that, in order to keep the Weber number constant, the oscillatory amplitude A had to be reduced at higher Womersley numbers. The streaming patterns are presented in Fig. 7.8.

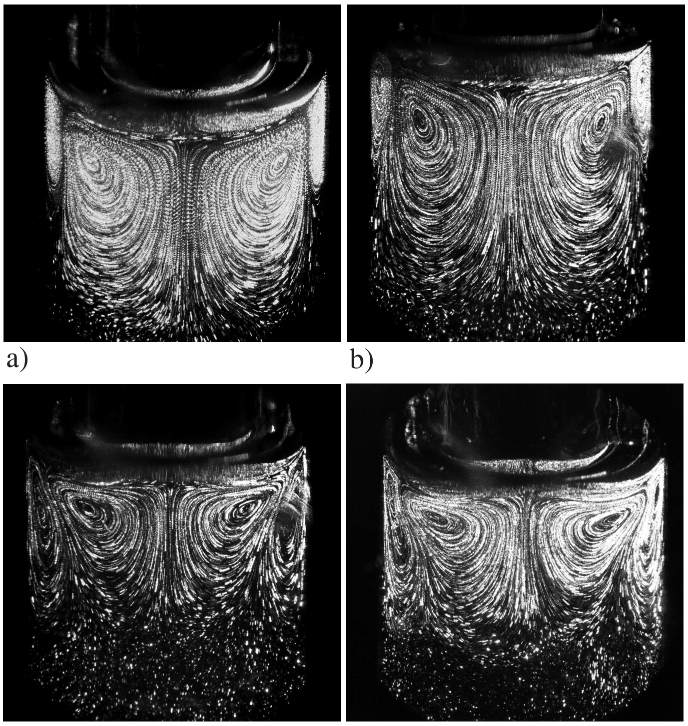

a) b) c) d)

Figure 7.8: Superposed particle images for 35 subsequent periods at We = 0.014, a) $\alpha = 8.5$, b) $\alpha = 10.5$, c) $\alpha = 12.1$, d) $\alpha = 13.5$.

It can be seen that the penetration depth of the streaming patterns decreases for higher Womersley numbers (due to lower excitation amplitudes). Additionally, the vortex patterns have changed. For lower Womersley numbers the vortex is axially stretched (Fig. 7.8a) and b)). The cross sectional shape corresponds to an ellipse. As α increases the inner vortex changes into the shape of a triangle (Fig. 7.8c) and d)). The radial extension of the outer vortex however increases. Consequently, the size of the inner and outer vortex is not related to the stokes layer thickness which decreases at higher Womersley numbers.

The velocity profiles at the axial position of the maximum streaming velocity are presented in Fig. 7.9 for constant Weber number of $We = 0.14$.

It can be seen that the maximum streaming velocities are constant for all Womersley numbers. Consequently, higher amplitudes compensate lower frequencies at constant Weber number in order to keep the maximum streaming velocity constant. Therefore, since the penetration depth of the streaming pattern decreases as the amplitude decreases, it might be advantageous to increase the amplitude, i.e. the tidal volume, rather than the ventilation frequency to achieve effective exchange of mass via liquid bridges. As already

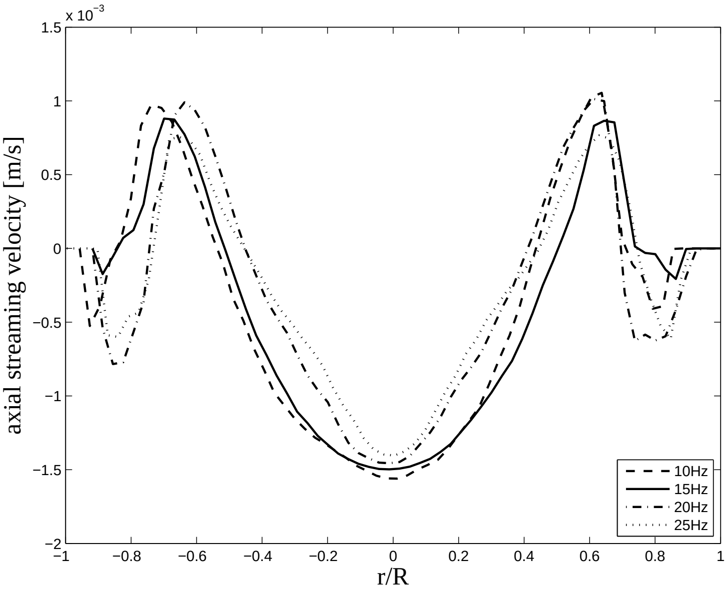

Figure 7.9: Axial velocity profiles at the location of the maximum streaming velocity at $We = 0.14$ for different Womersley numbers.

stated by Fang et al. [27], steady streaming effects are more enhanced by increasing tidal volume. The influence of frequency is only marginal.

Variation of the Boundary conditions

In order to confirm the influence of the free surface, a plate was put on the surface and the streaming pattern was observed for different Womersley numbers (frequencies) but constant amplitude. The results are shown in Fig. 7.10a) and d). The Womersley number increases from 10 to 15 but the streaming pattern remains constant since the free surface influence was suppressed at the wall. The Weber number is not relevant and hence, not given for Fig. 7.10a) and d).

For the cases depicted in Fig. 7.10b) and e), the Womersley number was again increased from 10 to 15, but here, a free surface exits. As can be clearly seen, the streaming patterns have strongly changed which indicated the strong influence of the Weber number. For additional analysis of the influence parameter on steady streaming, another liquid was used with a lower kinematic viscosity of $\nu = 15 \cdot 10^{-6}\,\mathrm{mm}^2/\mathrm{s}$ (Fig. 7.10c)). The Weber number is $We = 0.041$, the Womersley number is $\alpha = 15$. Hence, the Weber number corresponds to the case shown in Fig. 7.10b), the Womersley number to the case shown in Fig. 7.10e). The streaming pattern is again completely different from both cases. Consequently, a mixture of both, Womersley and Weber number, contributes to a typical

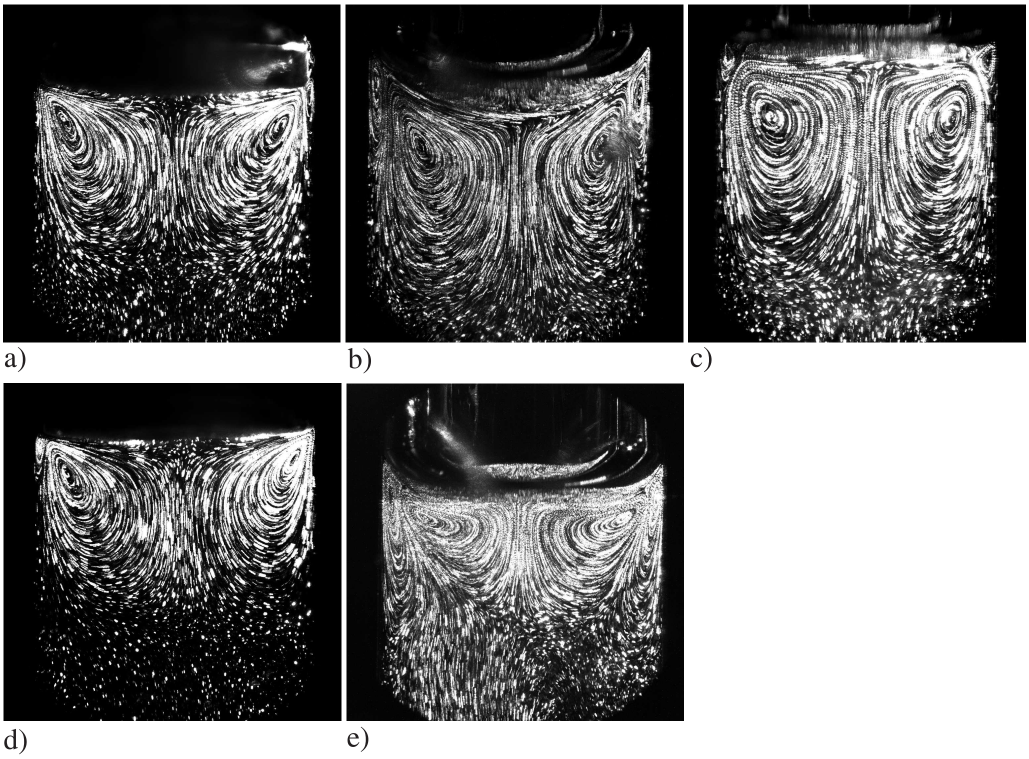

Figure 7.10: Visualization of steady streaming patterns a constant excitation amplitude of $A = 0.5\,\mathrm{mm}$, a) liquid-wall interface, $\alpha = 10.5$, b) free surface, $\alpha = 10.5$, $We = 0.041$, c) free surface, $\alpha = 15.0$, $We = 0.041$, d) liquid-wall interface, $\alpha = 14.8$, e) free surface, $\alpha = 14.8$, $We = 0.162$.

streaming pattern.

The maximum streaming velocity, determined for each case presented in Fig. 7.10, is depicted in Fig. 7.11. For the cases with "wall", the streaming velocity is similar and very low. Whereas those cases with a free surface are characterized by a higher streaming velocity. This suggests an amplification of steady streaming due to free surface instabilities. Higher Womersley numbers (e.g. by lower viscosity) lead to higher streaming velocity.

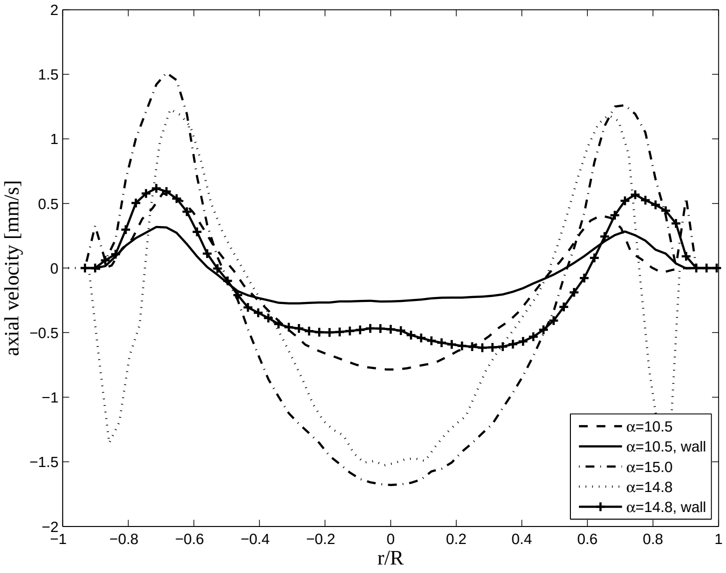

Figure 7.11: Axial streaming velocity for varying boundary conditions.

7.3.3 Steady streaming according to Reynolds Stress

Steady streaming as a mean motion forced by Reynolds stress has been introduced in chapter 2.5 on page 15. This assumption has to be verified by the calculation of the Reynolds stresses from the periodically unsteady velocity field. Therefore, PIV-measurements of the velocity vectors have been carried out. Altogether, 10 periods have been recorded with a resolution of 20 double-images per period. Exemplarily, the case of 10 Hz and excitation amplitude of 0.5 mm has been chosen.

The spatial variation of the Reynolds stress which causes a net force leading to steady streaming can be calculated according to [67]:

$$F_j = \frac{-\partial(\overline{\rho u_i' u_j'})}{\partial x_i}. \tag{7.7}$$

The variable u_i' denotes the fluctuating velocity in the directions of x_i according to the Einstein notation ($i = 1, 2, 3$). F_j represents the net rate of change of x_j-momentum in the x_i direction [67]. Since, the PIV-data are only available in a plane, the force is calculated only in two directions according to:

$$F_1 = -\rho \left(\frac{\partial(\overline{u_1'u_1'})}{\partial x_1} + \frac{\partial(\overline{u_2'u_1'})}{\partial x_2} \right), \tag{7.8}$$

$$F_2 = -\rho \left(\frac{\partial(\overline{u_1'u_2'})}{\partial x_1} + \frac{\partial(\overline{u_2'u_2'})}{\partial x_2} \right). \tag{7.9}$$

The differential equations 7.8 and 7.9 are discretisized by a Central Differencing Scheme (CDS), since velocity data are only available on a discrete grid. The procedure is first to calculate an average velocity field from all data. Then determine the fluctuations u_1' and u_2' at each grid point and insert them into the discretized form of equations 7.8 and 7.9. The resulting vector field F_j is illustrated in Fig. 7.12. The color contours represent the relative force magnitude. Fig. 7.12 reveals a similar vortex structure as received directly by the phase locked measurements. Hence, the assumption, that the Reynolds stress causes steady streaming could be confirmed. Note, that this calculation for two spatial directions is only possible due to the axisymmetric nature of the flow. For a fully three-dimensional flow, such as the flow through the human lung, the third component is necessary. Based on this knowledge, the steady streaming flow could be visualized directly from the velocity field in the human lung.

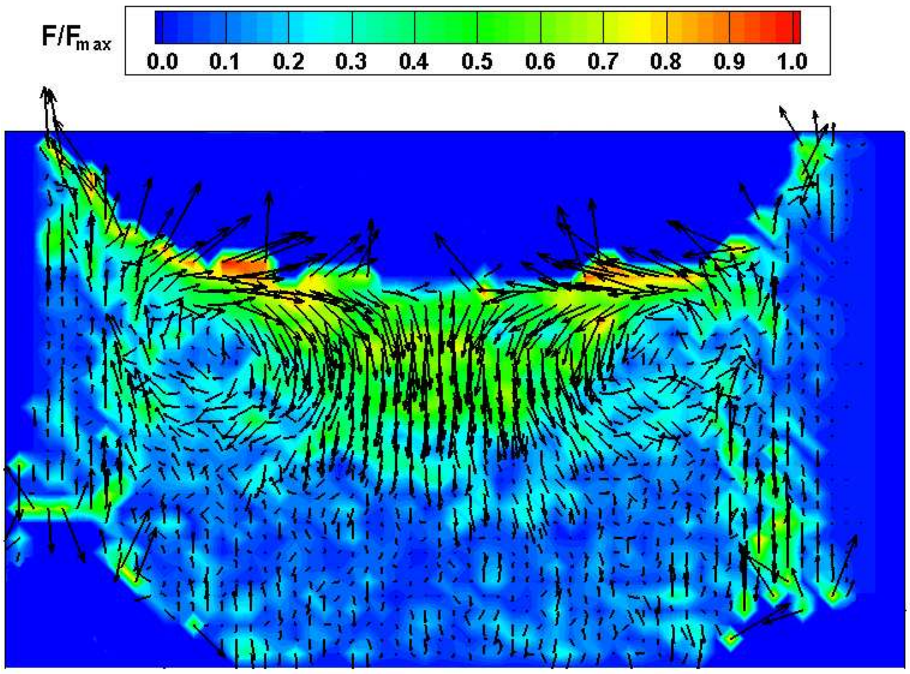

Figure 7.12: Vector field of the Reynolds stress, color contours represent the relative force magnitude F/F_{max}.

7.4 Conclusion

In this study the steady streaming and stability of oscillatory pipe flow with a free surface was analyzed. The experimental model used here could be compared to an occlusion of the upper human airway according to the order of magnitude of the characteristic flow numbers. The shear forces (Reynolds stress) caused by the interface boundary condition lead to a characteristic streaming pattern. The pattern shape mainly depends on the free surface interactions. That means, beginning instabilities deform the streaming pattern. Thereby this study can be regarded as a principle experiment for steady streaming flow and liquid bridge break up in the human lung. The calculation of the force caused by Reynolds stress gradients as well as the phase locked PIV-measurements reveal similar steady streaming patterns. Hence, this mathmatical method could be used to calculate the three-dimensional streaming patterns also for the human lung flow. It can be assumed that the parameters such as Reynolds number (which was here replaced by the Weber number) and Womersley number have the same impact on steady streaming flow in the human lung. That means increasing Reynolds number in the human lung also leads to enhanced steady streaming whereas the influence of the Womersley number (on steady streaming) is less important. It was found that the stokes layer thickness, governed by the Womersley number, is not related to steady streaming.

These steady streaming effects could be used to generate mass exchange even through liquid bridges, provided that gases are well enough solved in the liquid. For break up of the bridges, a certain oscillatory amplitude has to be exceeded which depends on the non-linear free surface oscillations.

8 Summary

In the studies presented here, the flow in the upper airways of the human lung was investigated experimentally as well as numerically for normal breathing conditions and high frequency oscillatory ventilation (HFOV) conditions. Therefore, a lung model consisting of 6 generations was generated which allowed exact comparison between experimental and numerical results. The model geometry is based on data from a real lung with a three-dimensional structure. Hence, the model is very realistic and the flow phenomena occurring in a real lung could be reliably reproduced. Flow characteristics in the human lung which were found in the literature could be confirmed with this model.

One restriction of the model is that the airways from the mouth to the larynx are not implemented. These parts of the airways have a strong influence on airflow into the trachea. However, the main interest of this work was to contribute to an improvement of the technique of mechanical ventilation. For the case of mechanical ventilation an endotracheal tube is used. Since the usage of a tube also leads to highly stochastic inflow situations depending on the tube position it was not implemented here. The main focus was on the difference in flow partitioning and flow structure caused by the parameter variation of e.g. Reynolds and Womersley numbers in the branching network.

For the experimental analysis, the model was made from transparent silicone in order to perform optical flow measurements. Here, the method of Particle Image Velocimetry (PIV)-measurements was used in the first study, in which flow patterns of the upper airways could be analysed. Novel insights, in particular details of the velocity patterns were found and analyzed for varying frequencies.

With the same geometry used for the experiments, numerical flow simulations have been carried out using the open source code OpenFoam. The validation with experimental results of the upper main branches revealed good agreement between both methods. Hence, the numerical simulations could be used to analyze the flow in regions that were not accessible for experimental measurements. Three-dimensional structures of the velocity patterns in the complete lung model could be analyzed which, to the best of our knowledge, was not reported before. The location of the maximum velocities is not only shifted from inspiration to expiration but also twisted. The development of secondary vortices within the branches could be explained in more detail by the illustration of the Helicity. Thereby, helical vortices could be visualized. Especially, the development of cloverleaf-like secondary patterns which occur during expiration, has been first explained. It was further shown that all velocity patterns rather depend on the local geometry but are not influenced by the upstream flow. Hence, it is reasonable that similar flow patterns could also be observed with single bifurcation models.

Considering flow partitioning, i.e. the distribution of mass between the branches, the resistances and compliances of the downstream branches are very important. Therefore, the three-dimensional geometry with a large number of generations is necessary. For investigation of flow partitioning, a new visualization technique was developed. Larger tracer particles were added to the flow and visualized by background illumination with parallel light and a telecentric lens set-up. The advantage of this visualization method was, that each image has the identical light intensity. The only difference between the images was the position of the particles represented by black dots. For each setting a very large number of images was acquired. After image processing and superposition of all images of one parameter set, a representative probability distribution of the particles was received which indicates the flow partitioning. The influence of different Reynolds and Womersley numbers (frequencies) on flow partitioning was investigated. Thereby, the tidal volume was always below the dead space of the model which was in accordance with the High Frequency Ventilation (HFV) technique. It was found that particles (all particles were injected at the top of the trachea) always pass the complete lung model and leave the model at the distal end. Even if the tidal volume was only half of the dead space. Higher Reynolds numbers lead to flow inhomogenization, i.e. preferred pathways through the medial branches, whereat higher Womersley numbers cause homogenization. The influence of the tidal volume is less important for mass transport. It was found that for decreasing tidal volume but higher Womersley numbers, mass transport is still enhanced. This allows to conclude that steady streaming, which is enhanced at higher tidal volumes, does not play a dominant role for mass transport through the human lung.

The compliant endings as occurring in a real lung were taken into account in the third study in which the opening behavior of a partly collapsed lung was simulated by rubber membranes. For better quantification of the membrane behavior a single bifurcation was used at which the membrane was fixed at one open end. The other branch was left open to the ambience. It could be shown that a higher frequency leads to an enhanced recruitment (membrane opening). This can be explained by two facts. First, higher frequencies cause higher pressure in the lung airways. Second, larger frequencies also increase the Reynolds number and hence, the pressure loss (resistance) in the lower airways. That means, for low frequencies, the flow partitioning is governed by the compliance of the different lung regions, i.e. material parameters. For increasing frequencies fluid mechanical parameters such as frictional and inertial forces dominate flow partitioning. Furthermore, the further up in the lung airway a collapse occurs, the easier the airways can be recruited due to the larger remaining pressure loss in the more distal airways.

For validation of the single bifurcation results, small membranes were fixed at all (32) distal openings of one main branch of the 6-generation model. The integral opening behavior was similar to the single membrane. Furthermore, PIV-measurements of the flow in the main branches of both models revealed very good correlation.

In the last study, the behavior of the flow in liquid bridges, i.e. a liquid obstructed airway, was analyzed. Therefore, oscillatory flow was applied in a liquid filled, vertical tube. The flow behavior at the liquid - air interface was investigated. According to the characteristic flow numbers, the behavior of the liquid column can be compared to liquid bridges in the human lung, which are dominated by surface forces. At the interface, a steady streaming pattern with toroidal shape is generated. It was found that the pattern strongly depends on the excitation amplitude, Weber and Womersley numbers. The streaming velocity depends on the Reynolds number. The break up of the liquid bridges was further investigated by stability analyses of the interface. For break up, the excitation amplitude is more important than the frequency. Especially in the smaller airways larger amplitudes are helpful to open blockages/obstructions. The smaller the diameter, the higher the amplitude is required for successful reopening. Additionally, decreasing the viscosity of the obstructing liquid (mucus) improves the reopening. Therefore, as airway blockage occurs, medicine which reduces the liquid viscosity should be inhaled. This study contributes to the understanding why a ventilation frequency, close to the natural frequency, leads to airway recruitment and which influence do the tidal volume and frequency have.

9 Outlook

Even though the human lung flow has been intensively investigated, there are still open questions. For example, the steady streaming flow which was frequently attributed to be important for gas exchange in the human lung is not well described up to date. Therefore, the three-dimensional numerical results could be used to calculate the steady streaming patterns in the human lung according to the study at the oscillatory tube interface. The challenge is here the three-dimensional nature of the human lung flow.

Furthermore, it was shown, that the human lung model, used here, incorporates a realistic geometry. Nevertheless, some features have not been implemented which contribute to an even more realistic lung behavior. These are among others, flexible airways, the airways from mouth/nose to the larynx or a higher number of generations. Especially the numerical flow simulation provides a great potential for further analyses. A first approach is to extend the grid cell number in order to receive a better resolution of the flow patterns.

A flexible lung geometry could be implemented by using fluid-structure interactions. According to Wall et al. [112] airflow patterns were quite different from flow simulations with stiff walls, despite a change in cross-sectional areas of only 2%. But, they also reported, that the change in flow distribution is moderate. Nevertheless, to implement fluid-structure interactions is a quite challenging task since many simulations run unstable or inefficient [112].

A further extension of the numerical model could be compliant endings which incorporate the behavior of a lung with collapsed regions. A final aim of such simulations should be a patient specific suggestion for the ideal ventilation technique.

Neutral buoyant particles can be added to the flow to receive more insights into flow partitioning as already investigated experimentally. A numerical simulation using particles has already been started and preliminary results show a distribution behavior that strongly depends on the initial position of particles within the lung model. Particles starting near the trachea wall travel preferentially to the outer branches, particles initially located in the trachea center propagate into the medial branches. Furthermore, the deposition of particles can investigated by inducing particles of different diameter and density. This is important for drug delivery or inhalation of toxic particles. Also the laryngeal geometry could be implemented which simulates the non-intubated case of normal breathing or breathing with the mask.

The experimental model could also be extended by artificial cilia (tiny hairs on the surface) and mucus which strongly influence the particle transport in the human airways. This is a very interesting but also challenging task.

The influence of the distensibility of the trachea on the distribution of mass in the human lung could be further analyzed.

Bibliography

[1] Adler, K., and Bruecker, C. Dynamic flow in a realistic model of the upper human lung airways. *Experiments in Fluids 43*, 2-3 (2007), 411–423.

[2] Alencar, A., Arold, S., Buldyrev, S., Majumdar, A., Stamenovic, D., Stanley, H., and Suki, B. Physiology: Dynamic instabilities in the inflating lung. *Nature 417*, 6891 (2002), 809–811.

[3] Andrade Jr., J., Alencar, A., Almeida, M., Mendes Filho, J., Buldyrev, S., Zappeeri, S., Stanley, H., and Suki, B. Asymmetric flow in symmetric branched structures. *Physical Review Letters 81*, 4 (1998), 926–929.

[4] Appell, H., and Stang-Voss, C. *Funktionelle Anatomie.* Springer Med. Verl., 2008.

[5] Banner, M., Jaeger, M., and Kirby, R. Components of the work of breathing and implications for monitoring ventilator-dependent patients. *Critical Care Medicine 22*, 3 (1994), 515–523.

[6] Bauer, K., and Bruecker, C. The role of ventilation frequency in airway reopening. *Journal of Biomechanics 42*, 8 (2009), 1108–1113.

[7] Behrens, T. Openfoam's basic solvers for linear systems of equations. *http://www.tfd.chalmers.se/~hani/kurser/OS_CFD_2008/TimBehrens/tibeh-report-fin.pdf.* (2009).

[8] Berghaus, A. *Hals-Nasen-Ohrenheilkunde.* Hippokrates Verlag, 1996.

[9] Brower, R., Matthay, M., Morris, A., Schoenfeld, D., Thompson, B., and Wheeler, A. Ventilation with lower tidal volumes as compared with traditional tidal volumes for acute lung injury and the acute respiratory distress syndrome. *New England Journal of Medicine 342*, 18 (2000), 1301–1308.

[10] Bruecker, C., and Riethmuller, M. Cyclic flow oscillations in a system of repeatedly branching channels. *Physics of Fluids 10*, 4 (1998), 877–885.

[11] Bruecker, C., and Schroeder, W. Flow visualization in a model of the bronchial tree in the human lung airways via 3-d piv. *Proceedings of PSFVIP-4, Chamonix, France* (2003).

[12] Calay, R., Kurujareon, J., and Holdo, A. Numerical simulation of respiratory flow patterns within human lung. *Respiration Physiology 130* (2002), 201–221.

[13] Carlon, G., Kahn, R., Howland, W., Ray Jr., C., and Turnbull, A. Clinical experience with high frequency jet ventilation. *Critical Care Medicine 9*, 1 (1981), 1–6.

[14] Chan, K., Stewart, T., and Mehta, S. High-frequency oscillatory ventilation for adult patients with ards. *Chest 131*, 6 (2007), 1907–1916.

[15] Cheng, G., Ueda, T., Sugiyama, K., Toda, M., and Fukuda, T. Compositional and functional changes of pulmonary surfactant in a guinea-pig model of chronic asthma. *Respiratory Medicine 95*, 3 (2001), 180–186.

[16] Courtney, S., Durand, D., Asselin, J., Hudak, M., Aschner, J., and Shoemaker, C. High-frequency oscillatory ventilation versus conventional mechanical ventilation for very-low-birth-weight infants. *New England Journal of Medicine 347*, 9 (2002), 643–652.

[17] David, M., and Werner, C. High-frequency oscillatory ventilation. ventilation procedure for adults with acute lung failure [hochfrequenz-oszillations-ventilation. beatmungsverfahren bei erwachsenen mit akutem lungenversagen]. *Anaesthesist 56*, 5 (2007), 485–490.

[18] Dean, W. Note on the notion of fluid in a curved pipe. *Philosophical Magazine 4*, 20, Sp. Iss. 7TH SERIES (JUL 1927), 208–223.

[19] Defares, J., and Donleben, P. Relationship between frequency-dependent compliance and unequal ventilation. *Journal of applied physiology 15* (1960), 166–169.

[20] Dragon, C., and Grotberg, J. B. Oscillatory flow and mass transport in a flexible tube. *Journal of Fluid Mechanics 231* (1991), 135–155.

[21] Drazen, J., Kamm, R., and Slutsky, A. High-frequency ventilation. *Physiological Reviews 64*, 2 (1984), 505–543.

[22] Dreyfuss, D., and Saumon, G. Role of tidal volume, frc, and end-inspiratory volume in the development of pulmonary edema following mechanical ventilation. *American Review of Respiratory Disease 148*, 5 (1993), 1194–1203.

[23] Dring, R. Sizing criteria for laser anemometry particles. *Journal Of Fluids Engineering-Transactions Of The ASME 104*, 1 (1982), 15–17.

[24] Durst, F., Ray, S., Ünsal, B., and Bayoumi, O. The development lengths of laminar pipe and channel flows. *Journal of Fluids Engineering 127 (6)* (2005), 1154–1161.

[25] Eckmann, D., and Grotberg, J. Oscillatory flow and mass transport in a curved tube. *Journal of Fluid Mechanics 188 , Mar. 1988* (1988), 509–527.

[26] Elad, D., Shochat, A., and Shiner, R. Computational model of oscillatory airflow in a bronchial bifurcation. *Respiration Physiology 112*, 1 (1998), 95–111.

[27] Fang, C., Cohen, B., and Lippmann, M. Aerosol tracer study of gas convective transport to 0.1-cm airways by high-frequency ventilation in a human lung airway cast. *Experimental Lung Research 18*, 5 (1992), 615–632.

[28] Farag, A., Hammersley, J., Olson, D., and Ng, T. Mechanics of the flow in the small and middle human airways. *Journal of Fluids Engineering, Transactions of the ASME 122*, 3 (2000), 576–584.

[29] Fisher, J., Mammel, M., Coleman, J., Bing, D., and Boros, S. Identifying lung overdistention during mechanical ventilation by using volume-pressure loops. *Pediatric pulmonology 5*, 1 (1988), 10–14.

[30] Fredberg, J., Keefe, D., and Glass, G. Alveolar pressure nonhomogeneity during small-amplitude high-frequency oscillation. *Journal of Applied Physiology Respiratory Environmental and Exercise Physiology 57*, 3 (1984), 788–800.

[31] Fresconi, F., and Prasad, A. Flow and convective dispersion in the conductive airways of the human lung. *Proceedings of the ASME Summer Bioengineering Conference* (2007), 101–102.

[32] Fresconi, F., and Prasad, A. Secondary velocity fields in the conducting air-

ways of the human lung. *Journal of Biomechanical Engineering 129*, 5 (2007), 722–732.

[33] Fresconi, F., and Prasad, A. Convective dispersion during steady flow in the conducting airways of the human lung. *Journal of biomechanical engineering 130*, 1 (2008), 011015.

[34] Fresconi, F., Wexler, A., and Prasad, A. Transport profiles in the conducting airways of the human lung. *International Journal of Heat and Mass Transfer 51*, 23-24 (2008), 5552–5561.

[35] Fuhrman, T., Gammon, R., Shin, M., and Buchalter, S. Pulmonary barotrauma in mechanical ventilation [8]. *Chest 104*, 3 (1993), 987.

[36] Fuhrmann, B., Paczan, P., and DeFrancisis, M. Perfluorocarbon-associated gas exchange. *Critical Care Medicine 19* (1991), 712–722.

[37] Gattinoni, L., Caironi, P., Cressoni, M., Chiumello, D., Ranieri, V., Quintel, M., Russo, S., Patroniti, N., Cornejo, R., and Bugedo, G. Lung recruitment in patients with the acute respiratory distress syndrome. *New England Journal of Medicine 354*, 17 (2006), 1775–1786.

[38] Gaver, D. P., and Grotberg, J. B. Experimental investigation of oscillating flow in a tapered channel. *Journal of Fluid Mechanics 172* (1986), 47–61.

[39] Gaver III, D. P., Jensen, O., and Halpern, D. Surfactant and airway liquid flows. *Lung Surfactant Function and Disorder (Lung Biology in Health and Disease) 201* (2005), 191–227.

[40] Gemci, T., Ponyavin, V., Chen, Y., Chen, H., and Collins, R. Computational model of airflow in upper 17 generations of human respiratory tract. *Journal of Biomechanics 41* (2008), 2047–2054.

[41] Goldberg, I., Zhang, Z., and Tran, M. Steady streaming of fluid in the entrance region of a tube during oscillatory flow. *Physics of Fluids 11*, 10 (1999), 2957–2962.

[42] Halpern, D., and Grotberg, J. Surfactant effects on fluid-elastic instabilities of liquid-lined flexible tubes: A model of airway closure. *Journal of Biomechanical Engineering 115*, 3 (1993), 271–277.

[43] Haselton, F., and Scherer, P. Flow visualization of steady streaming in oscillatory flow through a bifurcating tube. *Journal of Fluid Mechanics 123* (1982), 315–333.

[44] Henderson, D. M., and Miles, J. W. Single-mode faraday waves in small cylinders. *Journal of Fluid Mechanics 213* (1990), 95–109.

[45] Heraty, B., Laffey, J., and Quinlan, N. Fluid dynamics of gas exchange in high-frequency oscillatory ventilation: In vitro investigations in idealized and anatomically realistic airway bifurcation models. *Annals of Biomedical Engineering, 36 (11)* (2008), 1856–1869.

[46] Hickling, K. The pressure-volume curve is greatly modified by recruitment: A mathematical model of ards lungs. *American Journal of Respiratory and Critical Care Medicine 158*, 1 (1998), 194–202.

[47] Horsfield, K., and Cumming, G. Morphology of the bronchial tree in man. *Journal of applied physiology 24*, 3 (1968), 373–383.

[48] Horsfield, K., Dart, G., Olson, D., Filley, G., and Cumming, G. Models of the human bronchial tree. *Journal of applied physiology 31*, 2 (1971), 207–217.

[49] Hummler, H., Thome, U., and Schulze, A. Neue beatmungsstrategien in der neonatologie. *Monatsschr Kinderheilkd 150* (2002), 669–682.

[50] Ionel, I., Mochizuki, S., Comsa, O., and Lelea, D. Three-dimensional numerical simulation of the reciprocating flow in a branching tube network. *Heat Mass Transfer 46* (2010), 903–910.

[51] Ito, T., Tsuji, Y., and Kukita, Y. Interface waves excited by vertical vibration of stratified fluids in a circular cylinder. *Journal of Nuclear Science and Technology 36*, 6 (1999), 508–521.

[52] Johnson, A., Peacock, J., Greenough, A., Marlow, N., Limb, E., Marston, L., and Calvert, S. High-frequency oscillatory ventilation for the prevention of chronic lung disease of prematurity. *New England Journal of Medicine 347*, 9 (2002), 633–642.

[53] Jonson, B., and Svantesson, C. Elastic pressure-volume curves: What information do they convey? *Thorax 54*, 1 (1999), 82–87.

[54] Juckeland, G. http://tu-dresden.de/die_tu_dresden/zentrale_einrichtungen/zih /hpc /hochleistungsrechner/deimos, 16.08. 2010.

[55] Kaliner, M., Shelhamer, J., Borson, B., Nadel, J., Patow, C., and Marom, Z. Human respiratory mucus. *Am. Rev. Respir. Dis. 134* (1986), 612–621.

[56] Keane, R., and Adrian, R. Theory of cross-correlation analysis of piv images. *Applied Scientific Research 49* (1992), 191–215.

[57] Kitaoka, H., Takaki, R., and Suki, B. A three-dimensional model of the human airway tree. *Journal of Applied Physiology 87*, 6 (1999), 2207–2217.

[58] Kleinstreuer, C., Zhang, Z., and Donohue, J. Targeted drug-aerosol delivery in the human respiratory system. *Annual Review of Biomedical Engineering 10* (2008), 195–220.

[59] Kleinstreuer, C., Zhang, Z., and Li, Z. Modeling airflow and particle transport/deposition in pulmonary airways. *Respiratory Physiology and Neurobiology 163*, 1-3 (2008), 128–138.

[60] Krishnan, J., and Brower, R. High-frequency ventilation for acute lung injury and ards. *Chest 118*, 3 (2000), 795–807.

[61] Lachmann, B. Open up the lung and keep the lung open. *Intensive Care Medicine 18*, 6 (1992), 319–321.

[62] Lee, C., Anilkumar, A., and Wang, T. Streaming generated in a liquid bridge due to nonlinear oscillations driven by the vibration of an endwall. *Physics of Fluids 8*, 12 (1996), 3234–3246.

[63] Lee, W., Kawahashi, M., and Hirahara, H. Experimental analysis of air flows in bronchial airway models in the cases of natural breathing and hfov. *Journal of Fluid Science and Technology 1*, 2 (2006), 82–93.

[64] Lee, W., Kawahashi, M., and Hirahara, H. Experimental analysis of pendelluft flow generated by hfov in a human airway model. *Physiological Measurement 27*, 8 (2006), 661–674.

[65] Li. Z.and Kleinstreuer, C., and Zhanga, Z. Simulation of airflow fields and microparticle deposition in realistic human lung airway models. part i: Airflow patterns. *European Journal of Mechanics B/Fluids 26* (2007), 632–649.

[66] Lieber, B., and Zhao, Y. Oscillatory flow in a symmetric bifurcation airway model. *Annals of Biomedical Engineering 26*, 5 (1998), 821–830.

[67] Lighthill, S. Acoustic streaming. *Journal of Sound and Vibration 61*, 3 (1978), 391–418.

[68] Lin, C.-L., Tawhai, M., McLennan, G., and Hoffman, E. Characteristics of the turbulent laryngeal jet and its effect on airflow in the human intra-thoracic airways. *Respiratory Physiology and Neurobiology 157*, 2-3 (2007), 295–309.

[69] Liu, Y., So, R., and Zhang, C. Modeling the bifurcating flow in an asymmetric human lung airway. *Journal of Biomechanics 36* (2003), 951–959.

[70] Lomholt, N. Tracheal models which simulate the compliance of the adult male trachea. *British Journal of Anaesthesia 1992; 69: 98-100 69* (1992), 98–100.

[71] Luo, H., and Liu, Y. Modeling the bifurcating flow in a ct-scanned human lung airway. *Journal of Biomechanics 41*, 12 (2008), 2681–2688.

[72] Luo, X., Hinton, J., Liew, T., and Tan, K. Les modelling of flow in a simple airway model. *Medical Engineering & Physics 26* (2004), 403–413.

[73] Maunder, R., Shuman, W., and McHugh, J. Preservation of normal lung regions in the adult respiratory distress syndrome. analysis by computed tomography. *Journal of the American Medical Association 255*, 18 (1986), 2463–2465.

[74] Mauroy, B., and Bokov, P. The influence of variability on the optimal shape of an airway tree branching asymmetrically. *Physical Biology 7*, 1 (2010).

[75] Mauroy, B., Filoche, M., Weibel, E., and Sapoval, B. An optimal bronchial tree may be dangerous. *Nature 427*, 6975 (2004), 633–636.

[76] Melling, A. Tracer particles and seeding for particle image velocimetry. *Measurement Science and Technology 8*, 12 (1997), 1406–1416.

[77] Mochizuki, S., Togashi, Y., Murata, A., and Yang, W. Visualization experiment of mass transport in pulmonary ventilation inside bronchial tube model. *Journal of Mechanics in Medicine and Biology 2* (2001), 181–192.

[78] Mutch, W., Harms, S., Ruth Graham, M., Kowalski, S., Girling, L., and Lefevre, G. Biologically variable or naturally noisy mechanical ventilation recruits

atelectatic lung. *American Journal of Respiratory and Critical Care Medicine 162* (2000), 319–323.

[79] Müller, I. Inflating a rubber balloon. *Mathematics and Mechanics of Solids 7*, 5 (2002), 569–577.

[80] Nelson, T., West, B., and Goldberger, A. The fractal lung: Universal and species-related scaling patterns. *Experientia 46*, 3 (1990), 251–254.

[81] Nicolás, J., Rivas, D., and Vega, J. On the steady streaming flow due to high-frequency vibration in nearly in viscid liquid bridges. *Journal of Fluid Mechanics 354* (1998), 147–174.

[82] Nowak, N., Kakade, P., and Annapragada, A. Computational fluid dynamics simulation of airflow and aerosol deposition in human lungs. *Annals of Biomedical Engineering 31*, 4 (2003), 374–390.

[83] Pedley, T. pulmonary Fluid-dynamics. *Annual Review Of Fluid Mechanics 9* (1977), 229–274.

[84] Perchet, D., Fetita, C., Vial, L., Prêteux, F., Caillibotte, G., Sbîrlea-Apiou, and G., Thiriet, M. Virtual investigation of pulmonary airways in volumetric computed tomography. *Computer Animation and Virtual Worlds 15*, 3-4 (2004), 361–376.

[85] Phillips, C., and Kaye, S. On the asymmetry of bifurcations in the bronchial tree. *Respiration Physiology 107*, 1 (1997), 85–98.

[86] Porter, R.S.and Kaplan, J., Ed. *The Merck Manual of Diagnosis and Therapy - Eighteenth Edition*, 18th ed. Merck Sharp & Dohme Corp., New York., U.S.A., 2006.

[87] Putensen, C., Baum, M., and Hormann, C. Selecting ventilator settings according to variables derived from the quasi-static pressure/volume relationship in patients with acute lung injury. *Anesthesia and Analgesia 77*, 3 (1993), 436–447.

[88] Quintel, M., Meinhardt, J., and Waschke, K. Partielle flüssigkeitsventilation (partial liquid ventilation). *Anaesthesist 47* (1998), 479–489.

[89] Raffel, M., Willert, C., Wereley, S., and Kompenhans, J. *Particle Image Velocimetry - A Practical Guide*, 2nd edition ed. Springer-Verlag Berlin Heidelberg,

2007.

[90] Ramuzat, A., and Riethmuller, M. Piv investigations of oscillating flows within a 3d lung multiple bifurcation model. *11th Int. Symp. On Appl. of Laser Techniques to Fluid Flows, Lisbon, Portugal paper 19-1* (2002).

[91] Ritacca, F., and Stewart, T. Clinical review: High-frequency oscillatory ventilation in adults - a review of the literature and practical applicatons. *Critical Care 7*, 5 (2003), 385–390.

[92] Roberts, F. Respiratory physiology. *Update in Anaesthesia*, 12 (2000), 42–50.

[93] Royon-Lebeaud, A., Hopfinger, E., and Cartellier, A. Liquid sloshing and wave breaking in circular and square-base cylindrical containers. *Journal of Fluid Mechanics 577* (2007), 467–494.

[94] Schroter, R., and Sudlow, M. Flow patterns in models of the human bronchial airways. *Respiration Physiology 7*, 3 (1969), 341–355.

[95] Slutsky, A., and Hudson, L. Peep or no peep - lung recruitment may be the solution. *New England Journal of Medicine 354*, 17 (2006), 1839–1841.

[96] Snyder, B., Dantzker, D., and Jaeger, M. Flow partitioning in symmetric cascades of branches. *Journal of Applied Physiology Respiratory Environmental and Exercise Physiology 51*, 3 (1981), 598–606.

[97] Stark, A. High-frequency oscillatory ventilation to prevent bronchopulmonary dysplasia - are we there yet? *New England Journal of Medicine 347*, 9 (2002), 682–684.

[98] Suki, B., Alencar, A., Sujeer, M., Lutchen, K., Collins, J. J., Andrade, J., Ingenito, E., Zapperi, S., and Stanley, H. E. Lifesupport system benefits from noise. *Nature 393* (1998), 127–128.

[99] Suki, B., Arold, S., Alencar, A., Lutchen, K., and Ingenito, E. Noisy ventilation improves lung function. *AIP Conference Proceedings 665* (2003), 400–407.

[100] Suki, B., Barabási, A.-L., Hantos, Z., Peták, F., and Stanley, H. Avalanches and power-law behaviour in lung inflation. *Nature 368*, 6472 (1994), 615–618.

[101] Tarbell, J., Ultman, J., and Durlofsky, L. Oscillatory convective dispersion in a branching tube network. *Journal of Biomechanical Engineering 104*, 4 (1982), 338–342.

[102] Teng, Z., Ochoab, I., Li, Z., and Doblare, M. Study of tracheal collapsibility, compliance and stress by considering its asymmetric geometry. *Medical Engineering & Physics 31* (2009), 328–336.

[103] Theunissen, R., and Riethmuller, M. Particle image velocimetry in lung bifurcation models. *Topics Appl. Physics 112* (2008), 73–101.

[104] Tipton, C., and Mullin, T. An experimental study of faraday waves formed on the interface between two immiscible liquids. *Physics of Fluids 16*, 7 (2004), 2336–2341.

[105] Uchida, S. The pulsating viscous flow superposed on the steady laminar motion of incompressible fluid in a circular pipe. *ZAMP 7* (1956), 403–422.

[106] Ultman, J., Shaw, R., Fabiano, D., and Cooke, K. Pendelluft and mixing in a single bifurcation lung model during high-frequency oscillation. *Journal of Applied Physiology 65*, 1 (1988), 146–155.

[107] Van Ertbruggen, C., Hirsch, C., and Paiva, M. Anatomically based three-dimensional model of airways to simulate flow and particle transport using computational fluid dynamics. *Journal of Applied Physiology 98*, 3 (2005), 970–980.

[108] Van Reempts, P., Borstlap, C., Laroche, S., and Van der Auwera, J.-C. Early use of high frequency ventilation in the premature neonate. *European Journal of Pediatrics 162*, 4 (2003), 219–226.

[109] Vasquez, D., Singh, J., and Ferguson, N. Year in review 2006: Critical care - respirology. *Critical Care 11* (2007).

[110] Versteeg, H., and Malalaskera, W. *An Introduction to Computational Fluid Dynamics*, 2nd ed. Pearson Education Limited, 2007.

[111] Wackers, G. Modern anaesthesiological principles for bulbar polio: Manual ippr in the 1952 polio-epidemic in copenhagen. *Acta Anaesthesiologica Scandinavica 38*, 5 (1994), 420–431.

[112] Wall, W., L., W., Comerford, A., and Rausch, S. Towards a comprehensive

computational model for the respiratory system‡. *Int. J. Numer. Meth. Biomed. Engng. 26* (2010), 807–827.

[113] Wang, D., and Tarbell, J. Nonlinear-analysis Of Flow In An Elastic Tube (artery) - Steady Streaming Effects. *Journal Of Fluid Mechanics 239* (1992), 341–358.

[114] Wanner, A., Zarzecki, S., and Atkins, N. Relationship between frequency dependence of lung compliance and distribution of ventilation. *Journal of Clinical Investigation 54*, 5 (1974), 1200–1213.

[115] Wei, H.-H., Fujioka, H., Hirschl, R., and Grotberg, J. A model of flow and surfactant transport in an oscillatory alveolus partially filled with liquid. *Physics of Fluids 17*, 3 (2005), 031510–1–031510–16.

[116] Weibel, E. *Morphometry of the human lung.* Springer-Verlag, 1963.

[117] Wheeler, D. High frequency-oscillatory ventilation in adults. *Resp.Clin.* (2008), 18–20.

[118] Womersley, J. Method For The Calculation Of Velocity, Rate Of Flow And Viscous Drag In Arteries When The Pressure Gradient Is Known. *Journal Of Physiology-london 127*, 3 (1955), 553–563.

[119] Wyncoll, D., and Evans, T. Acute respiratory distress syndrome. *Lancet 354*, 9177 (1999), 497–501.

[120] Xi, J., P.W., L., and Martonen, T. Effects of the laryngeal jet on nano- and microparticle transport and deposition in an approximate model of the upper tracheobronchial airways. *Journal of Applied Physiology 104*, 6 (2008), 1761–1777.

[121] Yang, X., Liu, Y., and Luo, H. Respiratory flow in obstructed airways. *Journal of Biomechanics 39*, 15 (2006), 2743–2751.

[122] Zhang, Z., and Kleinstreuer, C. Transient airflow structures and particle transport in a sequentially branching lung airway model. *Physics of Fluids 14*, 2 (2002), 862–880.

[123] Zhang, Z., and Kleinstreuer, C. Airflow structures and nano-particle deposition in a human upper airway model. *Journal of Computational Physics 198* (2004), 178–210.